

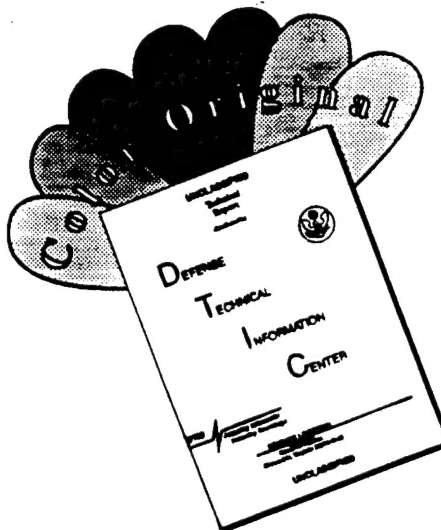
## REPORT DOCUMENTATION PAGE

Form Approved  
OMB No. 0704-0188

Public reporting burden for this collection of information is estimated to average 1 hour per response, including the time for reviewing instructions, searching existing data sources, gathering and maintaining the data needed, and completing and reviewing the collection of information. Send comments regarding this burden estimate or any other aspect of this collection of information, including suggestions for reducing this burden, to Washington Headquarters Services, Directorate for Information Operations and Reports, 1215 Jefferson Davis Highway, Suite 1204, Arlington, VA 22202-4302, and to the Office of Management and Budget, Paperwork Reduction Project (0704-0188), Washington, DC 20503.

1. AGENCY USE ONLY (Leave blank)	2. REPORT DATE	3. REPORT TYPE AND DATES COVERED	
	23 May 95	Final 2/1/92 - 12/31/94	
4. TITLE AND SUBTITLE <i>Quantitative Imaging of Time-Evolving Structure for Supersonic &amp; Hypersonic Flows</i>		5. FUNDING NUMBERS <i>F49620 92-J-0217</i>	
6. AUTHOR(S) Walt Lempert & Richard M. Iles		8. PERFORMING ORGANIZATION REPORT NUMBER	
7. PERFORMING ORGANIZATION NAME(S) AND ADDRESS(ES) Princeton University		10. SPONSORING / MONITORING AGENCY REPORT NUMBER <i>NA F49620 92-J-0217</i>	
9. SPONSORING / MONITORING AGENCY NAME(S) AND ADDRESS(ES) Air Force Office Of Scientific Research Aerospace & Materials Sciences Directorate 110 Duncan Avenue, Suite B-115 Bolling AFB DC 20332-0001			
11. SUPPLEMENTARY NOTES			
12a. DISTRIBUTION / AVAILABILITY STATEMENT APPROVED FOR PUBLIC RELEASE DISTRIBUTION IS UNLIMITED		12b. DISTRIBUTION CODE	
 13. ABSTRACT (Maximum 200 words)			
This final report documents activity for the period 2/1/92 to 12/31/94 on our AFOSR Contract #F49620-92-J-0217, entitled, "Quantitative Imaging of Time-Evolving Structure in Supersonic and Hypersonic Flows." This overall goals of this research were to develop new diagnostic tools capable of capturing unsteady and/or time-evolving, high-speed flow phenomena. The program centers around the development of Filtered Rayleigh Scattering (FRS) for velocity, temperature, and density measurement, and the construction of narrow linewidth laser sources which will be capable of producing an order MHz repetition rate "burst" of high power pulses.			15. NUMBER OF PAGES <i>94</i>
14. SUBJECT TERMS <i>Filtered Rayleigh Scattering</i>			16. PRICE/CODE <i>U</i>
17. SECURITY CLASSIFICATION OF REPORT <i>U</i>	18. SECURITY CLASSIFICATION OF THIS PAGE <i>U</i>	19. SECURITY CLASSIFICATION OF ABSTRACT <i>U</i>	20. LIMITATION OF ABSTRACT <i>U</i>

# DISCLAIMER NOTICE



THIS DOCUMENT IS BEST  
QUALITY AVAILABLE. THE COPY  
FURNISHED TO DTIC CONTAINED  
A SIGNIFICANT NUMBER OF  
COLOR PAGES WHICH DO NOT  
REPRODUCE LEGIBLY ON BLACK  
AND WHITE MICROFICHE.

**"QUANTITATIVE IMAGING OF TIME-EVOLVING STRUCTURE FOR  
SUPersonic AND HYPERSONIC FLOWS"**

**FINAL TECHNICAL REPORT**

**Contract #F49620-92-J-0217 P00004**

**TO:**

**AIR FORCE OFFICE OF SCIENTIFIC RESEARCH**

**AFOSR/PKA  
110 Duncan Ave., Suite B115  
Bolling Air Force Base, DC 20332-1001  
Attn: Carmen Calvert/PKA**

**Technical Monitor: Dr. Leonidas Sakell**

**Reporting Period: 2/1/92 to 12/31/94**

**Prepared by:**

**Dr. Walter R. Lempert  
Prof. Richard B. Miles**

**Department of Mechanical & Aerospace Engineering  
PRINCETON UNIVERSITY  
Princeton, NJ 08544**

<b>Accesion For</b>	
NTIS	CRA&I <input checked="" type="checkbox"/>
DTIC	TAB <input type="checkbox"/>
Unannounced <input type="checkbox"/>	
Justification _____	
<b>By _____</b>	
<b>Distribution / _____</b>	
<b>Availability Codes</b>	
<b>Dist</b>	<b>Avail and / or Special</b>
A-1	

**May 16, 1995**

(150-6635)

ed and is  
150-12

STINFO Program, University

19950821 044

## TABLE OF CONTENTS

	<u>Page #</u>
I. INTRODUCTION .....	3
II. SUMMARY OF RESULTS .....	4
A. I <sub>2</sub> FRS Development .....	4
i. Precision Laser Frequency Measurement .....	5
ii. Improvements of FRS Model and Fitting Routine .....	6
iii. Improvements of Iodine Absorption Model .....	7
B. Ultraviolet Filtered Rayleigh Scattering .....	7
i. Generation of High-Power, Single-Frequency, Automated Scanning at 761 nm .....	8
ii. Construction and Characterization of a Hg Filter at 0.2537 Microns .....	8
iii. Injection-Seeded, High Power UV Laser System .....	9
iv. Preliminary UV-FRS Images .....	9
C. Frequency Modulated-Filtered Rayleigh Scattering (FM-FRS) .....	10
i. Modulation Scheme .....	11
ii. Experimental Derivative Spectra .....	11
D. Pulse-Burst Laser Development .....	12
E. Flow Studies .....	13
i. Mach 3 Boundary Layer .....	14
ii. Mach 3 Inlet .....	14
iii. Mach 5 Free Jet .....	16
iv. Mach 2 Free Jet .....	17
F. Conclusions .....	19
REFERENCES .....	20
FIGURES .....	21
APPENDIX A: Performance Summary .....	45
Research Personnel .....	46
Associated Students .....	46
Collaborations .....	46
Individuals Who Have Requested Princeton Iodine Code .....	46
Presentation List .....	47
Publication List.....	48
APPENDIX B: Publication Reprints .....	49

## "QUANTITATIVE IMAGING OF TIME-EVOLVING STRUCTURE FOR SUPersonic AND HYPERSONIC FLOWS"

### I. INTRODUCTION

This final report documents activity for the period 2/1/92 to 12/31/94 on our AFOSR Contract #F49620-92-J-0217, entitled, "Quantitative Imaging of Time-Evolving Structure in Supersonic and Hypersonic Flows." This overall goals of this research were to develop new diagnostic tools capable of capturing unsteady and/or time-evolving, high-speed flow phenomena. The program centers around the development of Filtered Rayleigh Scattering (FRS) for velocity, temperature, and density measurement, and the construction of narrow linewidth laser sources which will be capable of producing an order MHz repetition rate "burst" of high power pulses.

The basic FRS principle (1), which utilizes a sharp cut-off atomic or molecular vapor filter to recover flow field scalar and vector data, is illustrated in Fig. 1. When narrow bandwidth laser radiation is incident upon a flow field, elastically scattered light from stray surfaces is superimposed upon the Doppler-shifted Rayleigh scattered light. If the laser frequency is tuned to coincide with the absorption band of an optically thick atomic or molecular vapor, and if a cell filled with the vapor is placed in front of a detector, then the elastically scattered light will be absorbed. By properly choosing the laser frequency relative to the edge of the vapor filter cut-off, the Doppler-shifted scattering will be, at least partially, transmitted. Since Rayleigh scattering is relatively intense, the laser light can be spread into a sheet, and single-pulse planar imaging approaches can be used to obtain instantaneous cross-sectional data. In general, the transmission is a function of both static temperature and velocity. By simultaneously performing two linearly independent transmission measurements (for example, by use of two filters with different passbands), instantaneous cross-sectional images of flow velocity and temperature can be obtained. If calibration of the absolute intensity of the scattering is also performed, instantaneous cross-sectional images of density, temperature, and velocity can, in principle, be obtained.

While the basic FRS principle is relatively straightforward, there are a number of technical challenges which need to be addressed in order to fulfill the potential of the method. In particular, extraction of quantitative flow parameters from the image data necessitates an accurate knowledge of both physical phenomena, such as molecular scattering and absorption, and instrumental phenomena, such as the stability of the spectral and spatial output of the laser system and the linearity and dynamic range of the microchannel plate intensified videocamera

system. Additionally, enhancements, such as extension into the ultraviolet, and modifications such as operation in a Frequency Modulated (FM) mode, serve to extend the range of applicability and to increase the accuracy of the technique.

Since the capabilities of virtually any diagnostic method are, ultimately, limited by the constraints imposed by available optical sources, a major goal of this program is to develop new laser sources. While these sources will be of particular utility to Filtered Rayleigh Scattering measurements, they will also be of general interest to the diagnostic and laser community. To this end, we have worked with Schwartz Electro-Optics, Concord, Massachusetts, to develop precise frequency control in both continuous wave and high power, pulsed, Titanium:Sapphire lasers; and with Medox, Inc., Ann Arbor, Michigan, to develop MHz rate, pulse "burst" technology.

Finally, we have endeavored at each step along the way to perform measurements in suitable flow environments in order to ascertain the true utility of the FRS method, and to couple the diagnostic with other experimental high-speed fluids research programs within the department.

With these overall goals in mind, the specific work performed under this contract can be broken down into the following five areas:

- i. Continued Development of the Iodine-Based FRS Technique.
- ii. Development of the Ultra-Violet FRS Technique.
- iii. Development of the Frequency-Modulated FRS Technique.
- iv. Development of a Pulse-Burst Laser Source.
- v. Experimental Tests.
  - a. Mach 3 High Reynold's Number Facility.
  - b. Mach 3 Inlet Model.
  - c. Mach 5 Free Jet.
  - d. Mach 2 Free Jet.

## **II. SUMMARY OF RESULTS**

### **A. I<sub>2</sub>FRS Development**

The ability to obtain quantitative flow data is predicated upon having developed an accurate model of both the spectroscopy of iodine and the details of the experimental procedure. To this

end, work has progressed on  $I_2$  code development, precise frequency measurement, and characterization of laser and camera performance. The results, which we shall summarize here, have been fully documented in a recent paper presented at the 33rd AIAA Aerospace Sciences Meeting (2) (copy attached).

### i. Precision Laser Frequency Measurement

The accuracy with which the laser frequency can be determined significantly affects the accuracy of the FRS method. We have addressed this issue by the development of a system, illustrated in Fig. 2, which is capable of continuously measuring laser frequency with high accuracy. This has been accomplished, as shown on the left side of Fig. 2, by first generating a well defined reference frequency. In order to do this, the infrared output of a Lightwave Model 124 cw Nd:YAG laser is passed through a frequency-doubling KTP crystal. The small amount of frequency-doubled light is then passed through a well stabilized iodine cell, and is used to "lock" the laser frequency to the frequency of a particular iodine absorption line. The frequency of the residual infrared laser light from this laser then becomes the reference to which all other measurements are compared.

To accurately characterize the absorption profile of our iodine filter, a second tunable cw Nd:YAG laser is used as shown on the right side of Fig. 2. The infrared output from this laser is also passed through a KTP crystal to generate a small amount of green, frequency-doubled light. This green beam is split into two legs. One of these is passed through the iodine cell to measure transmission as a function of frequency, while the other is monitored to account for fluctuations in laser intensity which occur when the frequency of the laser is tuned. The residual infrared beam is combined with the infrared beam from the reference laser and carried through a fiber optic to a high-speed photodiode. This heterodyning technique results in an amplitude modulation of the total intensity incident on the photodiode, the frequency of which is precisely the difference in frequency between the reference beam and the beam being used to characterize the cell. This beat frequency is measured by the high-speed counter and sent to the computer along with the transmission value through the iodine cell. This system was then used to accurately characterize the absorption profile of our iodine cell.

In order to obtain data in a high-speed flow facility, a high-power, pulsed interrogation laser, with precisely controlled frequency is required. The technique for achieving this is known as injection-seeding. In essence, a low power, cw, "seed" laser is used to control the spectral output of the high-power laser. By measuring the frequency of the seed beam, we can determine the

frequency of the high-power laser. The frequency of the seed beam is measured by splitting off a small piece of the beam and combining it with the reference laser beam on a high-speed photodetector (see Fig. 3). The beat frequency between the two beams is again measured with a high-speed counter.

The frequency measurement schemes described above have been tested and have resulted in measurements of frequency, relative to the reference, with an accuracy on the order of 1 MHz. For a typical experiment, a 1 MHz uncertainty in frequency corresponds to less than 1 m/s uncertainty in velocity.

## ii. Improvements of FRS Model and Fitting Routine

In order to obtain quantitative flow parameters, scattering data as a function of frequency is fit to theoretical predictions with velocity, temperature, and density taken as fitting parameters. Because the accuracy of the fitted values depends crucially on the accuracy of the fitting model, we have focused considerable efforts on improving the model to which data is fit. The main additions to the model consist of incorporating Brillouin scattering in the lineshape model, and including the effects of light collection over a non-infinitesimal solid angle.

The most accurate lineshape profile, which includes both Rayleigh and Brillouin scattering, was developed by G. Tenti in the 1970's (3,4). While this model describes the scattering lineshape more accurately than the simple Gaussian model which we used for our earlier experiments, it is also considerably more complex. We have obtained permission from Professor Tenti to incorporate his computer subroutines to our existing computer modeling and fitting codes.

We have also modified our modeling and fitting codes to include the effect of non-infinitesimal solid collection angle. The first approximation, which was used previously by us, and which is currently used by most other investigators, assumes that all of the light collected by the imaging lens experiences the same Doppler shift. However, this is not strictly correct. Because different portions of the imaging lens collect light which is scattered at different angles, and because the Doppler shift depends on scattering angle, the imaging lens actually collects light with a range of Doppler shifts. In order to take the variation in scattering angle across the lens into account, we have modified our computer routines to partition the lens into subunits, each small enough so that the variation in Doppler shift across each is small. The light collected by each of these subunits is then summed to yield the total amount of light collected. The fitting routine using

this new model will take into account the variation in scattering angle across the imaging lens, and, therefore, this will no longer be a source of uncertainty.

### **iii. Improvements of Iodine Absorption Model**

In order to accurately predict the iodine filter absorption characteristics, we have been developing a computer-based model which is capable of predicting the absorption profile of an arbitrary cell of any given temperature, pressure, and length. Prediction of filter absorption curves is important because it allows for the design of cells without requiring extensive laboratory work. During the past year, we have updated our model using the latest spectroscopic constants determined by P. Luc and S. Gerstenkorn (5), and hyperfine structure constants collected by M. Glaser (6). This model now include all of the lines experimentally observed in the tuning range of the frequency-doubled Nd:YAG, and the predicted lineshapes now match those measured experimentally quite well (see Figs 4 and 5).

This model is currently being used by a number of researchers in the United States and abroad to design iodine filter cells for particular experiments (see Appendix A). Some researchers are also using this model in lieu of performing experimental characterizations of their cells to analyze wind tunnel data obtained with FRS and related techniques.

### **B. Ultraviolet Filtered Rayleigh Scattering**

There are a number of distinct advantages resulting from shifting the FRS measurement into the ultraviolet (UV) region of the spectrum. First, UV sources take advantage of the scaling of the Rayleigh Scattering cross section with the fourth power of the frequency; second, the decreased reflectivity of metals in the UV reduces interference from stray "flare" scattering (7). These two features combine to produce greatly increased inherent contrast in images obtained from typical flow facilities. Finally, atomic mercury vapor filters exhibit nearly ideal characteristics.

In order to take advantage of this potential, we began a program in UV-FRS based on combination of an atomic mercury vapor filter and the third harmonic of a pulsed Ti:Sapphire laser source. This work was carried out in close collaboration with Schwartz Electro-Optics, Inc., Concord, Massachusetts, the manufacturer of the laser system. Together we received a Phase II Small business Innovative Research (SBIR) grant from NASA (Ames Research Center) to develop the high power and frequency control necessary for the FRS measurement. The

significant leveraging of the Phase I SBIR, provided by the current AFOSR grant, contributed significantly to our success and ultimate Phase II award.

The UV-FRS development effort is documented in detail in a presentation at the 32nd Aerospace Sciences Meeting in Reno, Nevada (8) (reprint attached). The work consisted of development of continuous, single frequency tuning in a commercial continuous wave (cw) Ti:Sapphire laser; construction and characterization of an atomic mercury vapor filter at 0.2537 microns; assembly of a high power injection-seeded laser system; and capture of preliminary UV-FRS images in a supersonic shear layer. We shall describe each of these briefly.

**i. Generation of High-Power, Single-Frequency, Automated Scanning at 761 nm**

Continuous single-frequency tuning was obtained by modifying a commercially available Schwartz Electro-Optics, Inc., Titan-cw laser system in the following manner (refer to Fig. 6): A piezo-electrically tunable etalon and a galvo-driven dual-tilt plate assembly were added to the ring cavity. The etalon had a free spectral range of approximately 75 GHz, a finesse of approximately two (mirror reflectivity of 20%), and was coated for operation between 700 and 900 nm. The purpose of the etalon is to select the single highest gain, longitudinal mode of the cavity by suppressing all others to below threshold for lasing. The tilt-plate assembly changes the effective cavity length and provides the continuous tuning capability. The etalon is modulated at 2 KHz, producing an amplitude modulation that is detected with a lock-in amplifier. A feedback signal is generated using the standard approach of first derivative nulling. This feedback provides a dc-bias voltage to the etalon, which stabilizes the cavity by insuring that the center of the etalon passband overlaps the peak of the cavity mode. The cavity is then continuously tuned with the tilt-plate assembly.

The above described approach was found to reliably tune over a frequency range in excess of 15 GHz, which exceeded the requirements for UV-FRS measurements.

**ii. Construction and Characterization of a Hg Filter at 0.2537 Microns**

A mercury vapor filter was constructed as illustrated in Fig. 7. The cell is 5 cm in diameter by 5 cm long, and the optical thickness is controlled by maintaining constant temperature on a side-arm "cold tip." The cold tip, which is 18 cm in length, is inserted into 0.5 liter water bath, whose temperature is regulated (to approximately  $\pm 0.25$  C) with a commercial temperature-controlled

closed loop recirculating system. The side-arm temperature determines the vapor pressure of mercury, and, therefore, the absorption. The cell was constructed from all quartz and was pumped-out prior to sealing, in order to avoid pressure broadening from air. The partial pressure of mercury, therefore, equals the cell total pressure. The body of the cell is wrapped with ordinary laboratory heating tape in order to maintain a temperature higher than that of the cold tip. Using this cell and the third harmonic light generated from the cw laser using a pair of BBO crystals, experimental transmission spectra were obtained at a variety of conditions. Figure 8 shows an experimental spectrum obtained with a cold-tip temperature of 23 C, and a body temperature of 48 C, along with modeling predictions. The mercury absorption cell is observed to have the nearly ideal characteristics of high line center extinction ( $\sim 10^{-30}$ ), and very sharp absorption edge (10-90% in 0.55 GHz).

### **iii. Injection-Seeded, High Power UV Laser System**

As discussed previously, the FRS measurement requires a high power, narrow bandwidth laser system in order to simultaneously spectrally resolve the molecular Doppler shift, and temporally freeze the flow structure. A block diagram of the system is shown in Fig. 9. An argon-ion laser is used to pump the cw Ti:Sapphire ring laser described previously. This acts as a seed source for a pulsed oscillator pumped by the second harmonic of a Q-switched Nd:YAG laser at 0.532 microns. Using 280 mJ of 0.532 pump power, we have obtained 80 mJ of injection-seeded fundamental at 0.761 microns (three times the wavelength of the mercury absorption filter). Using type I second harmonic, plus type II third harmonic generation, we have produced 10-12 mJ/pulse at 0.2537 microns.

### **iv. Preliminary UV-FRS Images**

Preliminary application of the UV laser source to image the flow from a nitrogen free jet demonstrates the utility of this system for UV-FRS. Figures 10a, 10b, and 10c show image scattering from the shear layer of a nitrogen free jet exiting an 1/8" nozzle (flow is from bottom to top). The laser is propagating from top right to bottom left. The mercury vapor filter is that described by Fig. 7. With the laser appropriately tuned outside the absorption band of the narrow band absorption filter, scattered light from the flow, ambient air, and nozzle flare are all apparent (Fig. 10a). In Fig. 10b, tuning the laser just into the absorption band of the mercury filter significantly suppresses the elastically scattered (and non-Doppler shifted) light. The moving shear layer remains Doppler-shifted outside the absorption band of the Hg filter. The high centerline absorption of the mercury filter allows for the discrimination of flow very near model

surfaces. The 1/8" nozzle is imaged because of ambient 532 nm light (from the Nd:YAG pump), and, possibly due to the UV source directly hitting the nozzle. Figure 10c demonstrates the ability to simultaneously suppress the flow and elastic scattering. Both the nonmoving and moving scattering sources are suppressed because the frequency of each scatterer lies within the absorption region of the mercury filter. This data, as well as additional work performed after the termination of this contract, have been submitted for presentation at the 34th AIAA Aerospace Sciences Meeting.

### C. Frequency Modulated-Filtered Rayleigh Scattering (FM-FRS)

In collaboration with M.L. Energia, Inc., Princeton, New Jersey, we have begun an effort to assess the capability of a potential velocity sensor, based on the combination of Frequency Modulation (FM) spectroscopy and FRS. Frequency Modulation is a well known approach for detecting small fractional changes in a signal. The basic FM approach is performed by applying a rapid (order of KHz) "dither" to the frequency of the excitation laser. As illustrated in Fig. 11, the effect of this dither is to superimpose what are termed frequency "side-bands" around the central "carrier" frequency of the laser. In essence, the laser output now consists of three distinct frequencies. The amplitude of the side-bands is determined by the magnitude of the dither, whereas the spectral separation is determined by the frequency of the dither (termed  $\Omega$ , the modulation frequency).

The key concept, common to any FM approach, is that differential attenuation of the side-bands will give rise to a signal at the modulation frequency, which can be detected with a lock-in amplifier. Since the dc offset has been removed, small fractional changes (as low as  $10^{-7}$ ) can be detected. The magnitude of the signal at the modulation frequency,  $\omega$ , is given as follows:

$$I_\omega = I_c I_\omega - I_c I_{-\omega} = I_c (I_\omega - I_{-\omega}) \quad (1)$$

where  $I_c$  is the detected intensity of the carrier, and  $I_\omega / I_{-\omega}$  are the detected intensities of the positive/negative side-bands, respectively. In a standard FM absorption experiment, the laser beam passes through an absorbing medium, most often a cell filled with a gas. If one tunes the carrier frequency through a symmetric absorption feature, the detected signal at the modulation frequency exhibits 1st derivative shape. Alternatively, the frequency of the laser can be stabilized to the center of the absorption profile by using the magnitude and sign of the derivative signal as feedback. This is termed "1st derivative locking" of a laser to an absorption profile.

The FM-FRS diagnostic (see Fig. 12) is based on "locking" the laser to the flow. We proposed to accomplish this by differential absorption of the Rayleigh scattering from the side-bands, using a potassium vapor cell and the cw Ti:Sapphire system described in Section B. The frequency of excitation of the laser will, in turn, be heterodyned against a low power reference laser which is locked directly to a cell. The difference in frequency is a measure of the Doppler shift produced by the flow field, and is, therefore, a measure of velocity. The significance of this research is that, given the exceedingly rapid progress in high power, compact, cw solid-state laser technology, a velocity sensor based on the FM-FRS diagnostic is a credible expectation in the near future.

The work performed to-date has been quite preliminary, and has focused on the design and implementation of a suitable FM modulation scheme, and the acquisition of experimental proof-of-concept "1st derivative" scattering spectra.

### i. Modulation Scheme

As a general rule, the larger the modulation frequency (and, hence, the maximum frequency excursion), the larger the FM signal. In practice, however, we were constrained by budget considerations. After significant survey of commercially available components, we decided on a modulation frequency of 100 MHz, and a heterodyned detection scheme, which would enable us to use a 100 KHz lock-in amplifier, already in-place in the laboratory. The design is shown schematically in Fig. 13. A 10 MHz reference oscillator is attenuated and split into two equal outputs which drive a pair of custom, phase-locked oscillators at 100 MHz and 99.9 MHz, respectively. The 100 MHz output is further split into two legs, one of which, after amplification, drives an electro-optic phase modulator, and the other of which goes to mixer 1. The 99.9 MHz signal is also split into two legs. One of these goes to mixer 1, the output of which provides the 0.10 MHz reference signal for the lock-in, and the other of these goes to mixer 2. Mixer 2 is used to heterodyne ("beat") the 100 MHz FM signal down to 0.10 MHz, which is then detected with the lock-in.

### ii. Experimental Derivative Spectra

To establish the feasibility of FM-FRS, a number of experiments were performed using the apparatus shown on the right side of Fig. 12. Absorption measurements of the potassium vapor filter from air and particle scattering were made to characterize the filter spectroscopy, signal-to-noise ratios, and the expected velocity measurement sensitivity. Shown in Fig. 14 are direct FRS

(filled circles) and FM-FRS (open circles) spectra obtained using an optically-thin potassium filter and approximately 100 mW from the Ti:Sapphire laser. Light scattered from a point along the beam by room air at 1 atm and 300 K was imaged at 45° through the filter and onto a photomultiplier tube. For the FM spectrum, the photocurrent was detected at the modulation frequency (100 MHz). Because the width of the potassium transition (~900 MHz) is much larger than the modulation frequency, the FM spectrum approximates the first derivative of the absorption lineshape. This represents the first, to our knowledge, FM spectrum obtained with light scattered from air as the source. Preliminary least-squares fits to the experimental FM spectrum have established a statistical uncertainty of approximately 2 MHz (2  $\sigma$ ) in measuring the line center frequency, which, for this geometry, propagates to a velocity uncertainty of approximately 2 m/s.

The preliminary results described above have been accepted for presentation as a post-deadline paper at the 1995 Conference on Lasers and Electro-Optics. Further results have been submitted for presentation to the 34th AIAA Aerospace Sciences Meeting.

#### **D. Pulse-Burst Laser Development**

While there has been enormous progress in recent years in the development and application of a variety of diagnostic imaging techniques, the ability to capture time-evolving or volumetric information is severely constrained by limitations of available laser technology. As a general rule, in the gas phase, signal levels for demonstrated imaging diagnostic techniques are sufficiently small that the measurements require high-power, nanosecond duration pulsed sources, such as Q-switched solid-state (principally Nd:YAG) or excimer lasers. The pulse repetition rate of these devices is limited to the range 10-30 pulses/second for solid-state lasers, and 10-300 pulses/second for excimer lasers. The current state-of-the-art is represented by double-pulsed Nd:YAG lasers, which may be used to produce a pair of excitation sheets, separated in time between 1-80 microseconds, to capture two sequential images. With this in mind, we have begun the assembly of a high-power, Nd:YAG-based, "pulse burst" laser system. The system is capable of creating a "train" of on the order of 30-40 high power pulses, at a burst frequency of up to 1 MHz. The number and interpulse spacing of the individual pulse is flexible, and individual pulse energies on the order of 10's to 100's of mJ's are, ultimately, anticipated. It should be pointed out that the laser system complements, particularly well, a novel, MHz rate CCD framing camera, currently being developed by Princeton Scientific Instruments, Inc., Monmouth Junction, New Jersey, under a Phase II SBIR grant from the Wright Patterson Air Force Base.

The pulse burst laser system illustrated in Fig. 15 consists of the following four elements:

1. Monolithic, single-frequency, diode-pumped, cw Nd:YAG laser.
2. Pulse slicer.
3. Two-stage, multi-pass preamplifier.
4. Two-stage power amplifier.

The single-frequency Nd:YAG laser is a Lightwave Electronics model 120-03, with cw power of approximately 20 mWatts. The output of this laser is polarization-coupled into preamplifier #1, which is a four-pass, 10 Hz repetition rate, flashlamp-pumped, 7 mm diameter by 110 mm long Nd:YAG rod. The small signal, single pass gain has been measured to be approximately 10x, so that the output of preamplifier #1 is a single, approximately 100 microsecond duration, 200 Watt peak power pulse, repeated at a repetition rate of 10 Hz. This 100 microsecond pulse is formed into a "train" using a pulse slicer, custom built by Medox, Inc., Ann Arbor, Michigan. The pulse slicer consists of a pair of fast electro-optic Pockel cells, and is capable of creating an arbitrary number of pulses, with minimum individual pulse duration of 10 nsec, and minimum inter-pulse period of 1 microsecond. The output of the pulse slicer is spatially filtered and double-passed through preamplifier #2. To date, we have obtained  $10^6$  net power gain out of this system, with pulse trains consisting of 10-20 pulses, and individual pulse durations between 10-20 nsec. This corresponds to individual pulse energies between 200-400 microjoules.

The above described system has existed in our laboratory for approximately nine months, and its operation is relatively straight-forward. The number, spacing, and duration of the pulses within the train can be continuously varied by flipping a few thumbwheel switches on the slicer timing electronics. A two-stage power amplifier has recently become available in our laboratory, and we plan to add it to our system this summer. Individual pulse energies of the order of mJ's are anticipated.

The ultimate pulse energy achievable should be limited only by the availability of additional amplifiers. While individual pulse energies of the order of 100's of mJ's are considered quite realistic, there is at the current time no funding in place for their purchase.

#### **E. Flow Studies**

Over the course of the contract period, FRS has been demonstrated in a variety of supersonic flow environments including a Mach 3 boundary layer, a Mach 3 inlet model, and Mach 2 and 5

free jets. These experiments are described in more detail in References 2, 9, 10, and 11 (copies attached). All of the measurements were performed using a molecular iodine vapor filter.

### i. Mach 3 Boundary Layer

Experimental tests were conducted in the 8" x 8" high Reynold's number facility at the Gas Dynamics Laboratory which is located at Princeton's James Forrestal Campus. The tests were done using a high power, injection-locked Nd:YAG laser which had been previously installed in that laboratory with support from AFOSR (Contract #AFOSR-90-0420 F). The laser was expanded into a sheet which passed at an angle through the flow field so that a significant Doppler shift was generated in the scattered light. Initially (Fig. 16a), the laser is tuned away from the molecular filter absorption line so that both scattering from the flow and scattering from the windows and walls is captured in the camera image. As the laser is tuned, first scattering from the windows and walls is suppressed by the filter (Fig. 16b), and finally, scattering from the flow is suppressed (Fig. 16c). It should be noted here that, in this particular facility, strong scattering from the flow field is observed due to the condensation of residual water vapor which forms a low density ice "fog" in the low temperature portions of the flow field. Since the ice crystals are large compared to the size of molecules, the random motion is small, so the cut-off rate associated with the scattering from the flow is similar to that associated from scattering from the walls and windows, and represents the combination of the laser linewidth and the filter edge profile. By digitizing the image sequence as the laser is tuned and comparing the laser frequency at which the windows and walls are cut-off with the laser frequency at which the flow field is cut-off, one can determine the flow velocity. Figure 17 shows the results of such a procedure using image data similar to that of Fig. 16. In this case, a velocity of  $524 \pm 36$  m/sec was measured.

### ii. Mach 3 Inlet

A series of FRS imaging experiments were performed in the 8" x 8" wind tunnel using a supersonic inlet model. The tunnel was run with a stagnation temperature of 260 K, stagnation pressure of 100 psi, and with a free stream Mach number of 3. A schematic of the inlet model and imaging optics is shown in Fig. 18. The model consisted of two 24-inch long flat plates, each mounted parallel to the wind tunnel floor and ceiling. The bottom plate was mounted 2 inches from the floor of the wind tunnel, while the top plate was mounted 2 inches from the ceiling of the wind tunnel (4 inches from the bottom plate). The boundary layer on the wind tunnel walls was approximately 1 inch thick at the leading edge of the flat plates, so the flow

entering the model was free of any initial boundary layer. Between these two flat plates were two variable angle vertical fins. The leading edges of the fins were separated by approximately 6 inches, and were 7.6 inches downstream of the leading edges of the flat plates. Although each fin angle could be varied independently from 5 degrees to 11 degrees with respect to the wind tunnel free stream flow direction, all of the data obtained were taken with both fins set at 11 degrees. Optical access to the inlet model was provided by BK7 and quartz windows mounted in the floor and ceiling of the wind tunnel, and in the two flat plates in the model.

To obtain the images, laser light was focused into a sheet 0.8 mm thick and 7 cm wide, and passed through the model oriented perpendicular to the flat plates, and spanwise with respect to the incident free stream flow. Light from the laser sheet was scattered by an ice vapor fog which is formed in the cold regions of the flow from a few parts per million residual water vapor in the compressed air supply. The light scattered from the flow in the downstream direction was turned by a 3-1/8 inch by 1-5/8 inch, front surface aluminum mirror which was placed roughly 27 inches downstream of the leading edges of the flat plates. This mirror was mounted at an angle of 45 degrees to the tunnel walls on the end of a sting arm. Light reflected from this mirror passed through a quartz window mounted in the side of the tunnel and was imaged by a Vivitar zoom lens onto a double-intensified CID camera. The camera output was stored on videotape for subsequent analysis.

Images were taken at 26 different downstream locations inside of the model, with the farthest upstream location 12.3 inches downstream of the leading edges of the flat plates. Subsequent locations were separated from each other by 0.1 inches. Each image captured a slice of the flow roughly 3 inches high and 3 inches wide. In order to preserve the camera magnification as the laser sheet was translated, the camera assembly was also translated in 0.1 inch increments.

A set of two-dimensional images are shown in Fig. 19. In the first 11 images, the edge of the turbulent boundary layer on the bottom flat plate is clearly visible. Outside of the boundary layer, where the static temperature is cold, the ice vapor fog is present, and much light is scattered. Within the boundary layer, however, the static temperature is much higher, so the ice vapor fog disappears, and very little light is scattered. The interface between the dark and light regions, therefore, indicates the location of the gradient in static temperature at the edge of the boundary layer. The effect on the boundary layer of the strong pressure gradients generated across the vertical shocks is clearly seen in these images. Boundary layer fluid is forced to the centerline of the model using a "bulging" of the boundary layer as the flow moves downstream.

Shock locations in these images are also clearly visible. In the first 7 images taken at locations ahead of the shock crossing point, the shocks are observed as curved lines of slightly increased intensity extending from the top of the field-of-view to the bottom boundary layer. In the images taken farther downstream, beyond the shock crossing point, the static temperature after the shocks is high enough that the ice vapor fog disappears completely, and so, shocks are observed here as sharp discontinuities between bright and dark regions of the images. The two crossing shocks observed in these images exhibit a continuous curvature from the bottom boundary layer to the top of the field-of-view.

The images of Fig. 19 were reconstructed using a three-dimensional projection algorithm developed previously in this laboratory (11, 12). Figures 20a and 20b show example images generated for an observer looking downstream/upstream, respectively, from the crossing shock using the two-dimensional images from Fig. 19.

### iii. Mach 5 Free Jet

In collaboration with M.L. Energia, Princeton, NJ, a Mach 5 overexpanded free jet was set-up as shown in Fig. 21. Once again, the laser was focused to a sheet and passed at an angle through the flow field so that a significant Doppler shift occurred. The experiment was conducted in a manner similar to that done in the Mach 3 facility, but, in this case, scattering was from air molecules rather than a condensate fog. As the laser was tuned, the background scattering from windows and walls was eliminated in much the same manner as seen in the Mach 3 facility. The scattering from the flow, on the other hand, turned off slowly due to the thermal motion of the molecules. An example of the digitized data is shown in Fig. 22, together with a least-squares fit. This resulted in mean values of velocity equal to  $649 \text{ m/sec} \pm 11 \text{ m/sec}$ , and temperature equal to  $60 \text{ K} \pm 9 \text{ K}$ . It should be noted that most of the scatter seen in this data is due to fluctuations in the free jet itself.

Measurements were also made at very low pressure in this free jet facility to determine pressure limitations associated with the Filtered Rayleigh Scattering approach. Line images were taken at pressures down to 5 torr, suggesting that this approach will be viable in existing hypersonic facilities.

#### iv. Mach 2 Free Jet

As a final example, a very careful set of time-mean data is being obtained in both ambient air and in a near pressure-matched Mach 2 laboratory free jet. The purpose of these measurements is to ascertain the absolute accuracy of planar FRS measurements of velocity, temperature, and velocity obtained under well defined and characterized conditions. The particular emphasis is to elucidate any systematic errors associated with inaccuracies in either the iodine FRS model, or the experimental procedure.

The configuration for these experiments is as follows: The laser beam was focused into a sheet and passed through the 6" x 6" vertical test section of a laboratory-scale wind tunnel, at an angle of roughly 50 degrees to the vertical. The scattering was captured orthogonal to the laser sheet and an absorption cell containing molecular iodine was placed in front of the camera lens. The ambient room air test condition was achieved by temporarily removing the windows on the test section before the experiment was performed. The Mach 2 test utilized a stagnation pressure of 100 psig, and a stagnation temperature of 258 K. Isentropic calculations predict that the free stream velocity, static temperature, and static pressure at the exit of this jet should be 480 m/s, 143 K, and 753 torr, respectively. In order to achieve a significant Doppler shift, the Nd:YAG beam crossed the flow at an angle of 50 degrees. This necessitated that the measurement region in the flow be located between 12 mm and 22 mm (2 to 4 nozzle diameters) downstream of the nozzle exit in order to keep the laser beam from hitting the nozzle.

A data run consisted of obtaining 50 camera frame averages at each of 110 different laser frequencies. The image data was binned into 10 by 10 superpixels corresponding to approximately 300 micron by 300 micron spatial resolution in the object plane (i.e., the flow). At each resolution element, the fitting procedure described above was performed. Figure 23 shows the experimental data (dots) and the best least squares fit (solid) for a single, representative resolution element for the ambient air case. Similar fits, one at each resolution element, yielded values for  $v$ ,  $T$ , and  $P$  at each point in the flow.

The measured planar velocity profile from test case one, which has a uniform velocity of 0 m/s, is shown in Fig. C.1. The laser sheet extends from the top right of the plot to the bottom left. Measured velocity values within the sheet range from -12 m/s to 31 m/s. A comparison of Fig. C.1 with Fig. C.2, which shows the laser sheet intensity, indicates that the variations in measured velocity are correlated with the spatial profile of the laser intensity. We postulate, therefore, that the velocity errors are due to a non-linearity of the detection system. In particular, the region at

the top of the laser sheet, with low laser energy (less than 75% of the peak), exhibits the largest discrepancy in the measured velocity. Neglecting this small portion of the laser sheet yields a measured velocity range between -12 m/s and 10 m/s. Current work is centered on quantifying the camera non-linearity. Results from a detailed error analysis which includes all other sources of systematic uncertainty, predict that resolution of the non-linearity issue will reduce the velocity uncertainty for these conditions to approximately 4 m/s.

Velocity values obtained from the Mach 2 free jet are shown in Figs. C.3 and C.4. The core of the jet exhibits velocities between 192 m/s and 221 m/s, while the shear layers, apparent on either side of the core, exhibit velocities between 200 m/s and 0 m/s. The isentropic value is calculated to be 220 m/s. Points outside of the flow, but still within the laser sheet, exhibit velocities of approximately 0 m/s. It should be emphasized that the measured velocity is the velocity component along the direction of FRS sensitivity, which is determined by the laser propagation direction, and the camera observation direction. When comparing the measured core velocities to the isentropic value, these angles were measured relative to the exit surface of the nozzle and the jet was assumed to issue perpendicular to this surface. If the direction of the jet differs from the perpendicular by one degree, the isentropic value changes by 8 m/s. As in the case of ambient air, a significant discrepancy is observed across the laser sheet, particularly in the low energy region. However, RELIEF measurements have exhibited velocity variations of  $\pm 4$  m/s in this region of the flow.

Although the temperature and pressure data obtained from the Filtered Rayleigh Scattering experiments has not yet been fully analyzed, Figs. C.5 and C.6 show preliminary plots of this data for the Mach 2 condition. Both show general behavior of the parameters as expected. The pressure of the free jet appears to be the same as that of the ambient surroundings, as expected from a pressure matched nozzle, although the pressure values vary significantly across the entire region of interest. These variations are believed to be due, in part, to variations in the jet, and in part to the non-linearities discussed above. The temperature of the free jet is seen in Fig. C.6 to be significantly lower than that of the ambient surroundings, as expected. Although the variation of measured temperature across the jet is  $\pm 17$  K, the average value of 142 K agrees with the isentropically calculated value of 143 K.

## **F. Conclusions**

We have conducted a multi-prong research program consisting of diagnostic development, the generation of new laser sources, and a series of experimental tests in a variety of flow environments. Two new diagnostics, Ultra-Violet (UV) and Frequency Modulated (FM) Filtered Rayleigh Scattering techniques, have been demonstrated. Significant progress toward a high power, MHz rate pulse "burst" Nd:YAG system has been achieved. FRS imaging experiments have been performed in a Mach 3, high Reynold's number boundary layer, a Mach 3 inlet, and Mach 2 and Mach 5 free jets.

## REFERENCES

1. R.B. Miles and W.R. Lempert, "Two-Dimensional Measurement of Density, Velocity, and Temperature, in Turbulent High-Speed Air Flows by UV Rayleigh Scattering," *Applied Physics B*, Vol. 51, pg. 1, 1990.
2. J.N. Forkey, N.D. Finkelstein, W.R. Lempert, and R.B. Miles, "Control of Experimental Uncertainties in Filtered Rayleigh Scattering Measurements," Paper #AIAA-95-0298, AIAA 33rd Aerospace Sciences Meeting and Exhibit, Reno, NV, January 9-12, 1995.
3. C.D. Boley, Rashmi C. Desai, and G. Tenti, *Canadian Journal of Physics* 50, p. 2158, (1972).
4. G. Tenti, C.D. Boley, and Rashmi C. Desai, *Canadian Journal of Physics* 52, p. 285, (1974).
5. S. Gerstenkorn and P. Luc, "Atlas du Spectre d'Absorption de la Molecule d'Iode," (Editions du CNRS).
6. M. Glaser, *Optics Communications* 54, p. 335, (1985).
7. D.E. Gray, *American Institute of Physics Handbook*, 2nd Ed., p. 6-119 (1963).
8. N. Finkelstein, J. Gambogi, W.R. Lempert, R.B. Miles, G.A. Rines, A. Finch, and R.A. Schwarz, "The Development of a Tunable, Single-Frequency Ultraviolet Laser Source for UV Filtered Rayleigh Scattering, Paper #AIAA-94-0492, AIAA 32nd Aerospace Sciences Meeting and Exhibit, January 10-13, 1994, Reno, Nevada.
9. R.B. Miles, J.N. Forkey, and W.R. Lempert, "Filtered Rayleigh Scattering Measurements in Supersonic/Hypersonic Facilities," Paper #AIAA092-3894, AIAA 7th Aerospace Ground Testing Conference, Nashville, TN, July 1992.
10. J.N. Forkey, W.R. Lempert, S.M. Bogdonoff, R.B. Miles, and G. Russell, "Volumetric Imaging of Supersonic Boundary Layers Using Filtered Rayleigh Scattering Background Suppression," Paper #AIAA-94-0491, AIAA 32nd Aerospace Sciences Meeting and Exhibit, January 10-113, 1994, Reno, Nevada.
11. J. Forkey, S. Cogne, A. Smits, S. Bogdonoff, W.R. Lempert, and R.B. Miles, "Time-Sequenced and Spectrally Filtered Rayleigh Imaging of Shock Wave and Boundary Layer Structure for Inlet Characterization," Paper AIAA-93-2300, AIAA/SAE/ASME/ASEE 29th Joint Propulsion Conference and Exhibit, Monterey, CA, June 28-30, 1993.

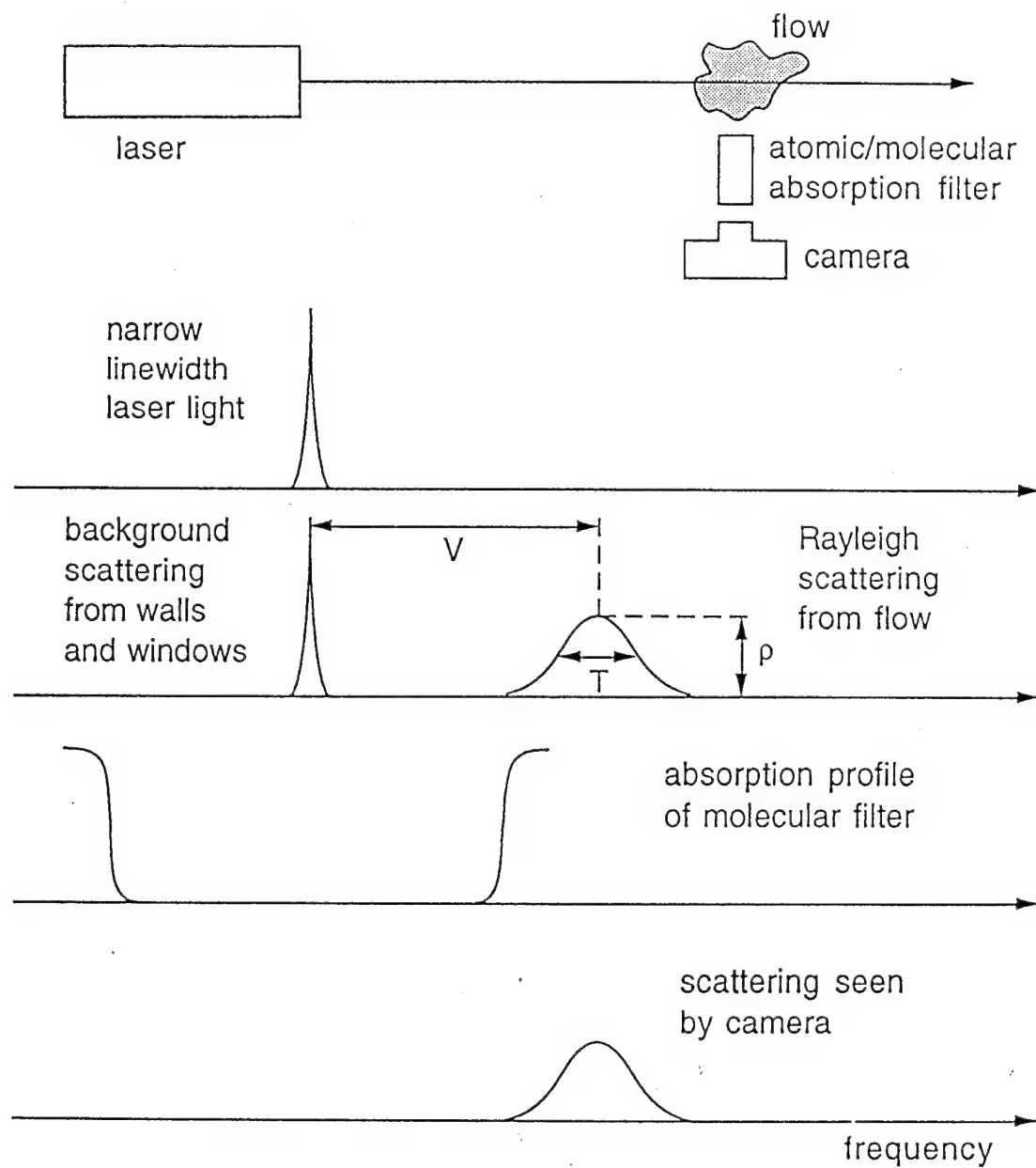


Figure 1. Basic Filtered Rayleigh Scattering process.

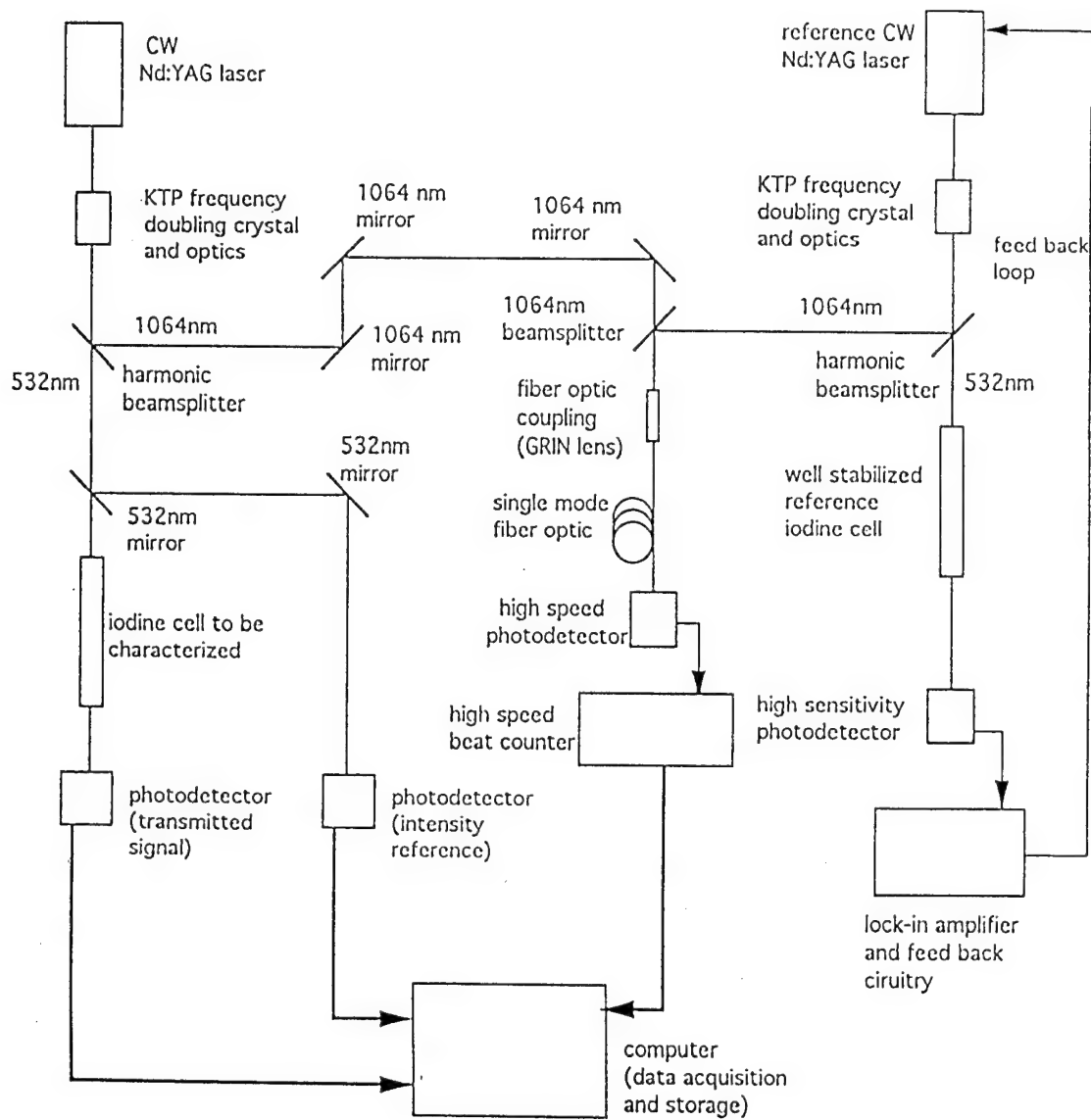


Figure 2. Schematic of apparatus for accurate measurement of filter profile and laser wavelength.

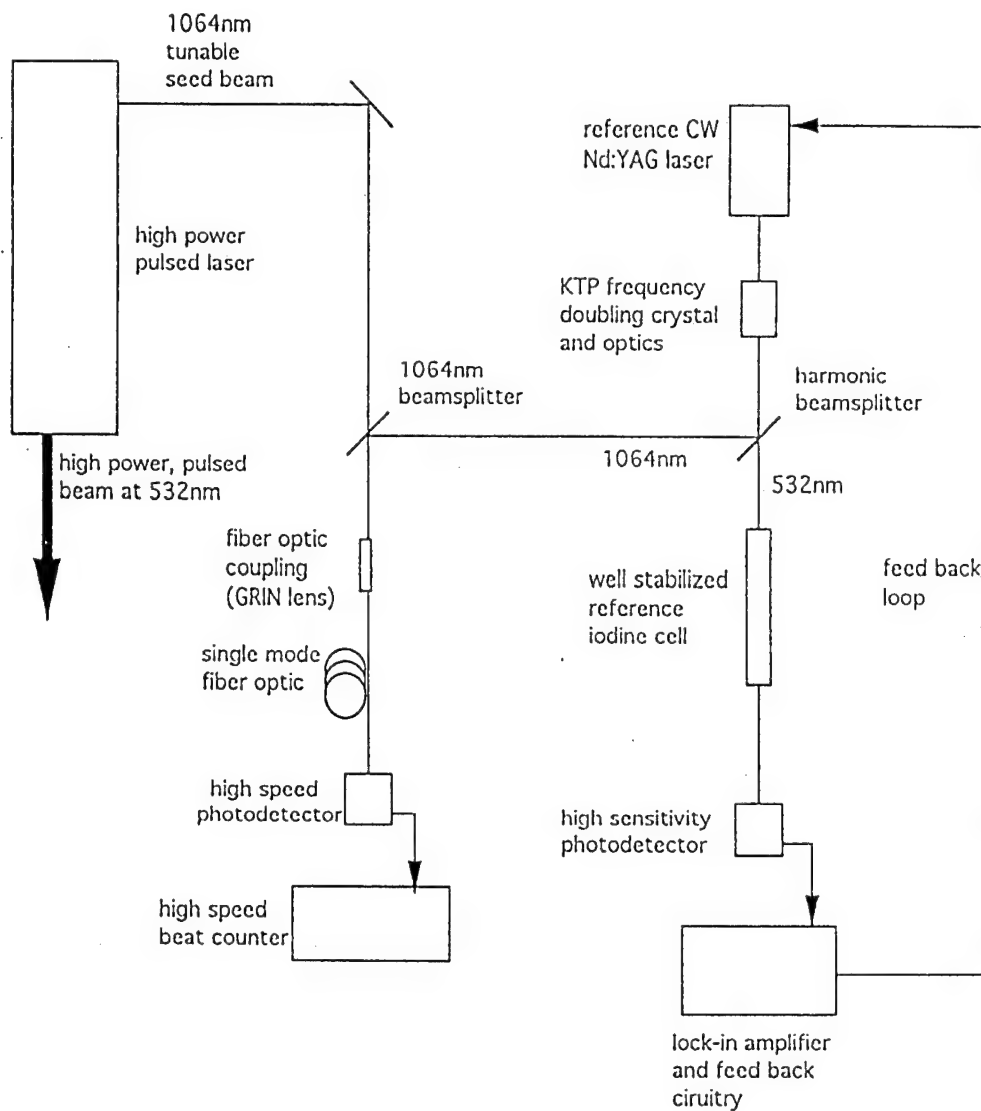


Figure 3. Schematic of apparatus for accurate determination of excitation laser frequency.

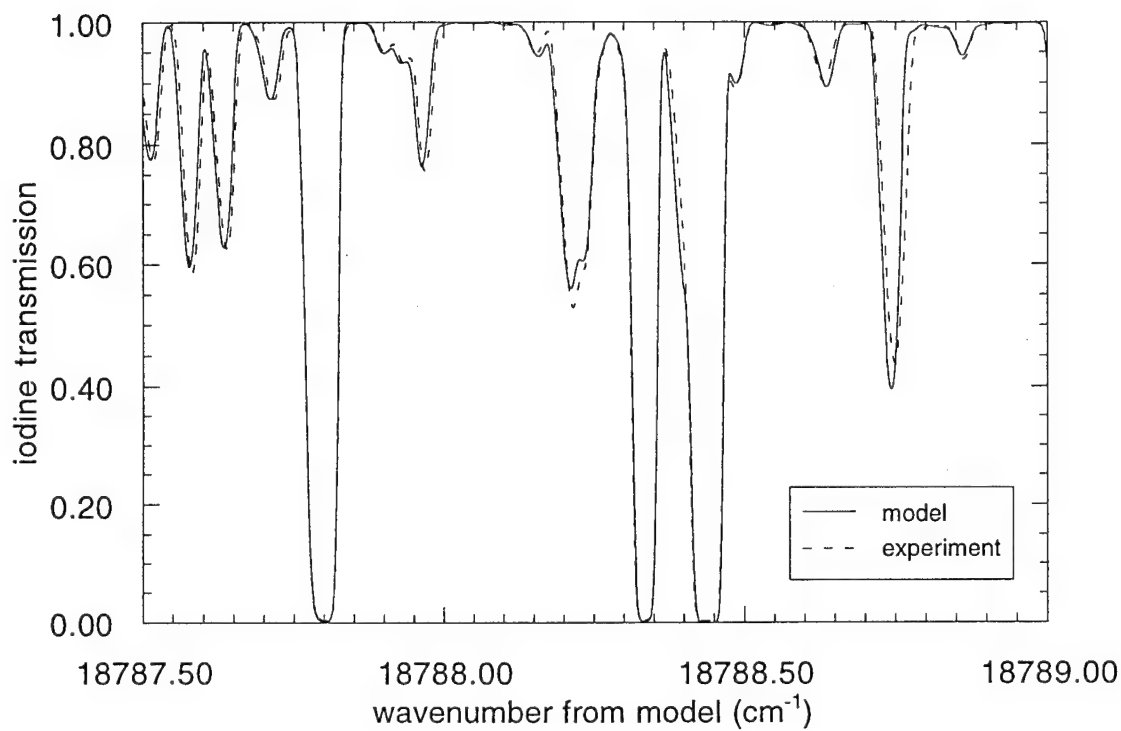


Figure 4. Experimental and modeled iodine absorption features over full tuning range of Nd:YAG laser.

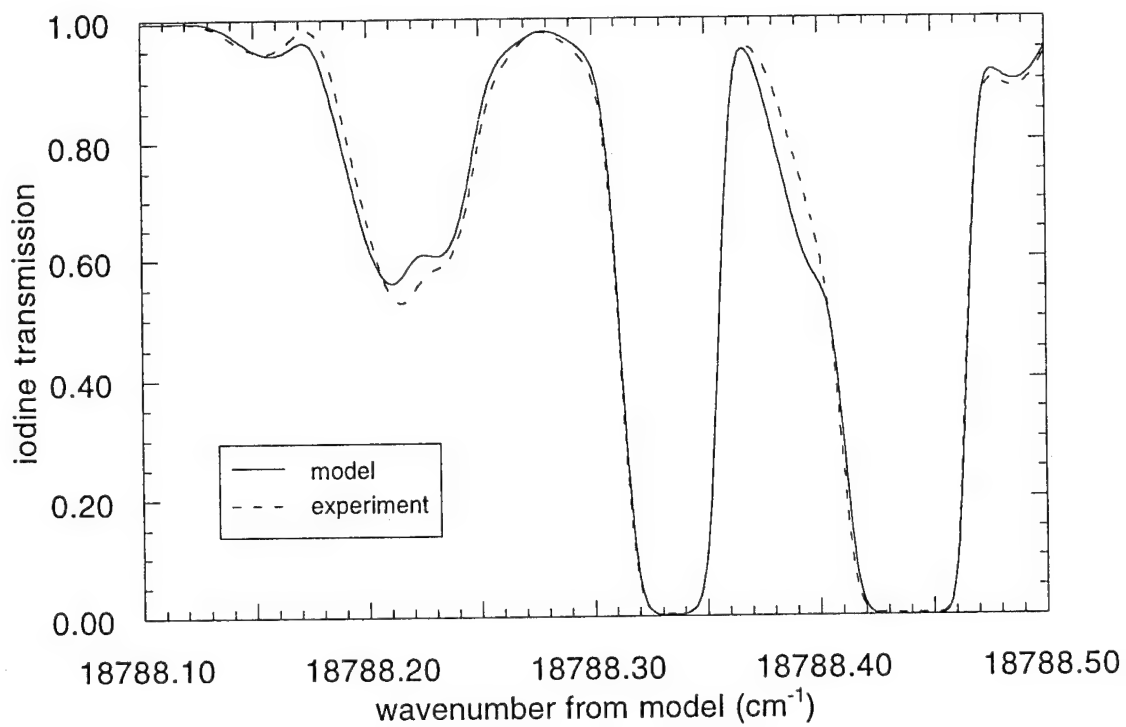


Figure 5. Experimental and modeled iodine-absorption features used for FRS measurement.

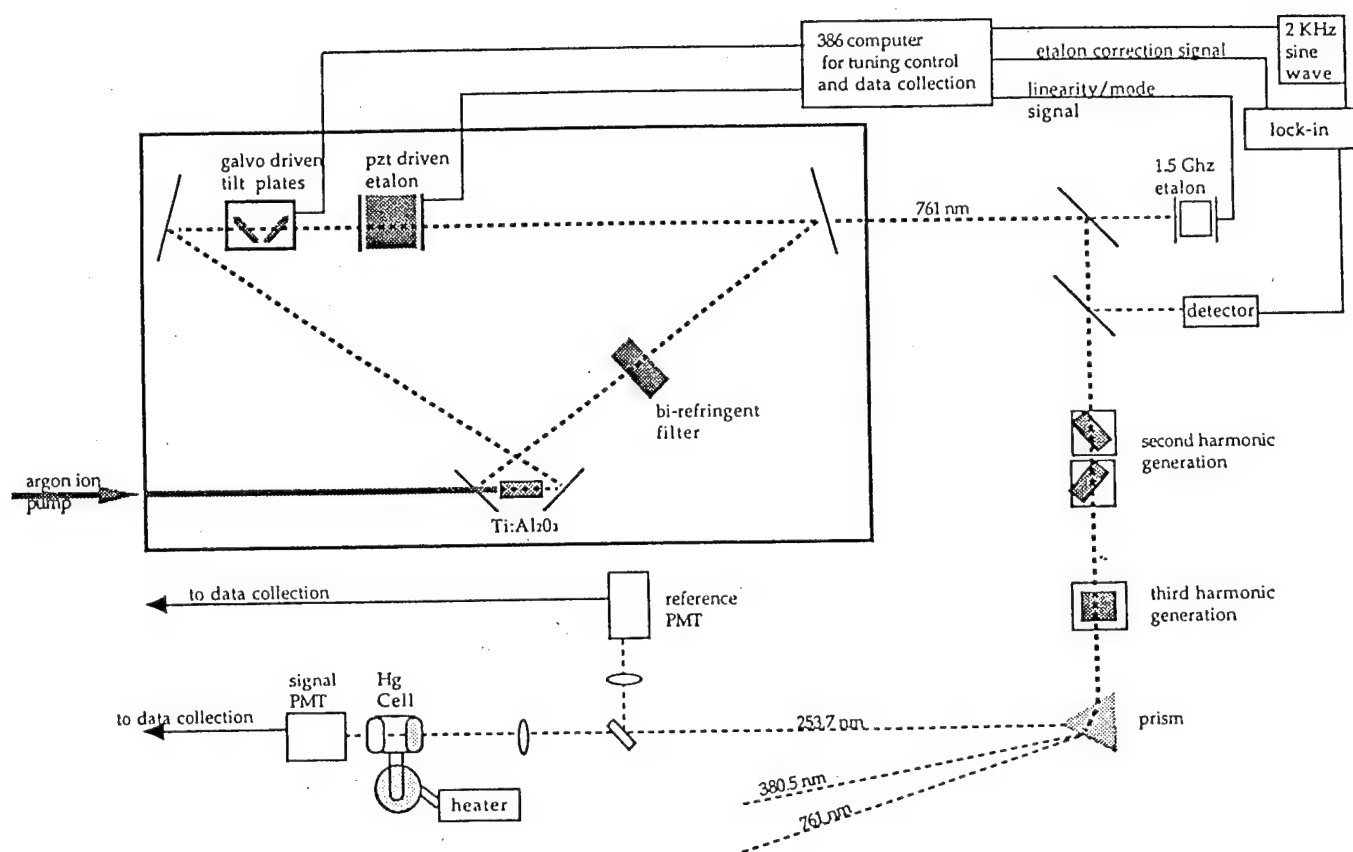
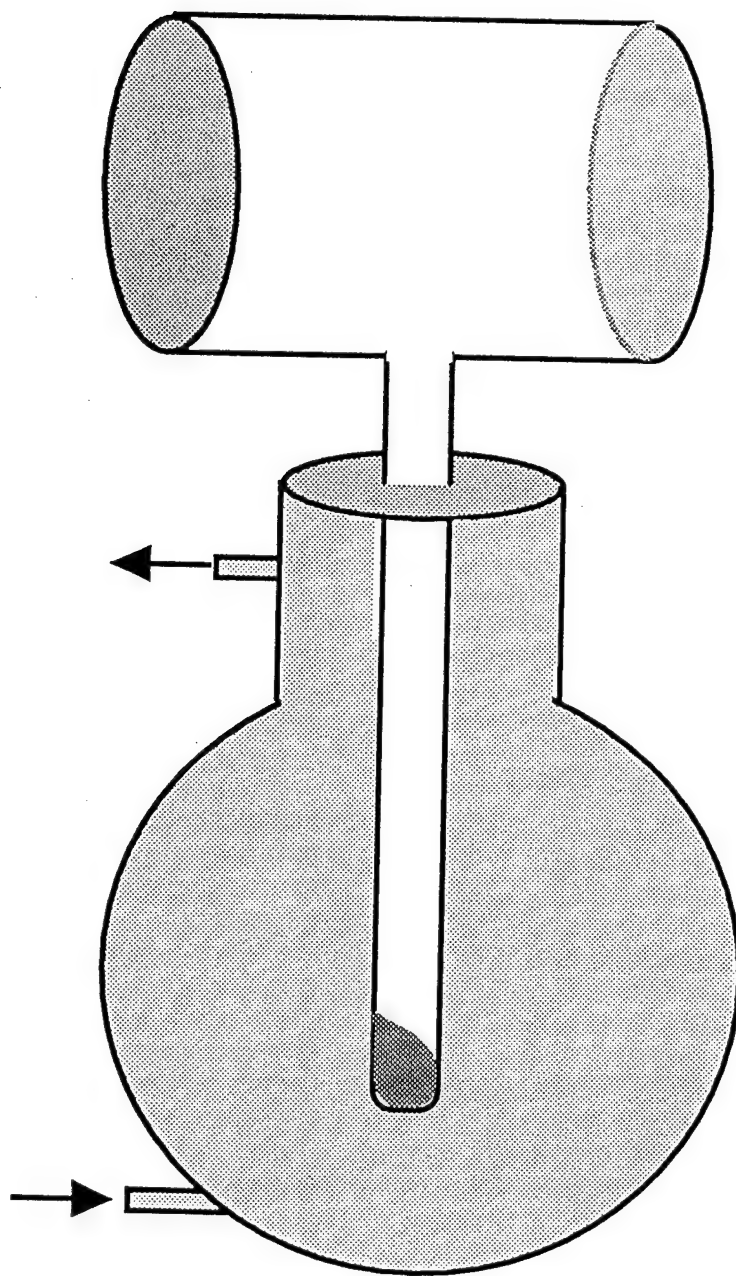


Figure 6. Schematic diagram of cw Ti:Sapphire system.



cell length: 5 cm.  
window diameter: 5 cm.  
side arm length: 18 cm.  
bath volume: 0.5 litre  
mercury content: 5 grams  
vacuum: 0.05 torr

Figure 7. Mercury vapor filter.

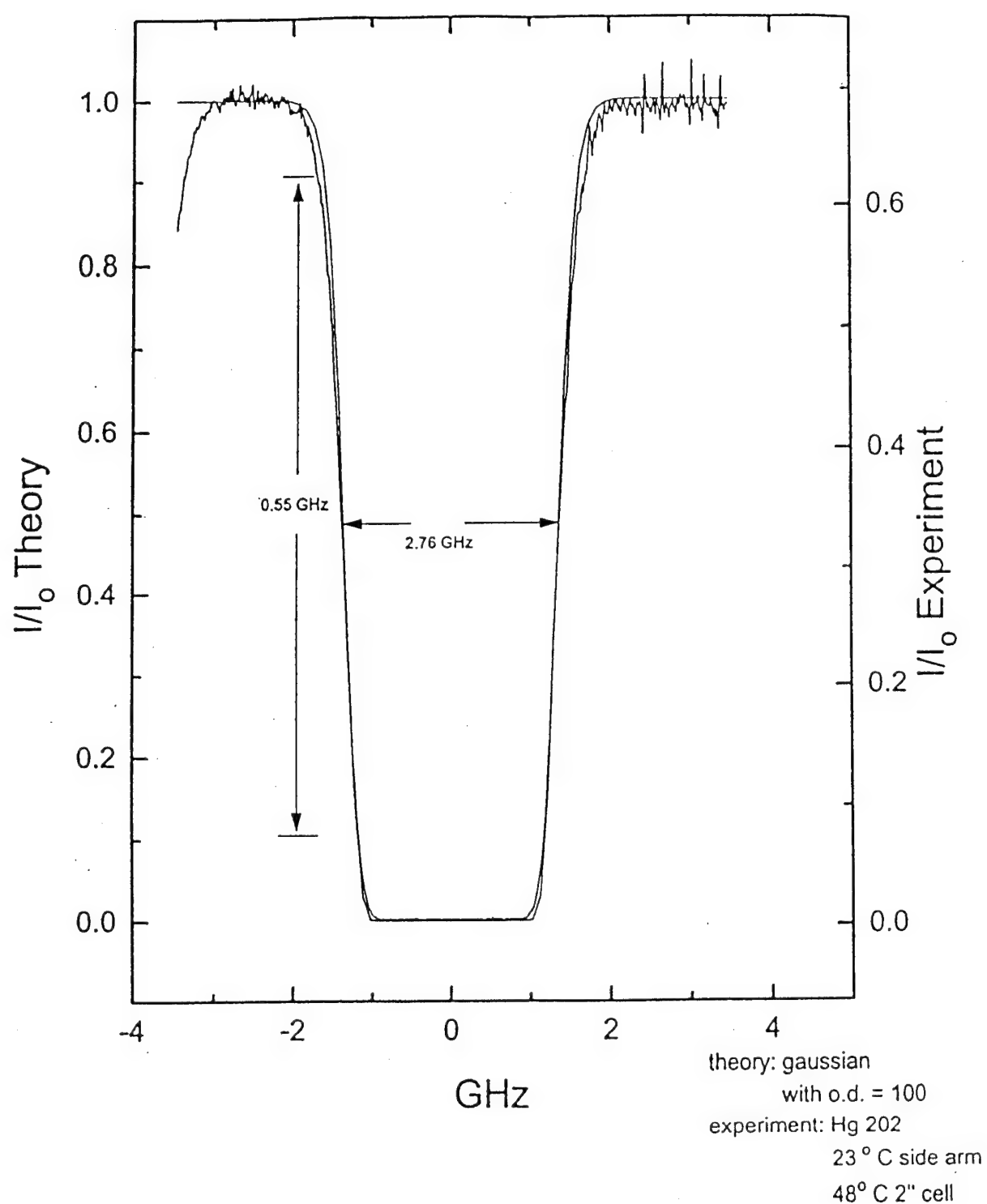


Figure 8. Experimental and modeled mercury absorption filter.

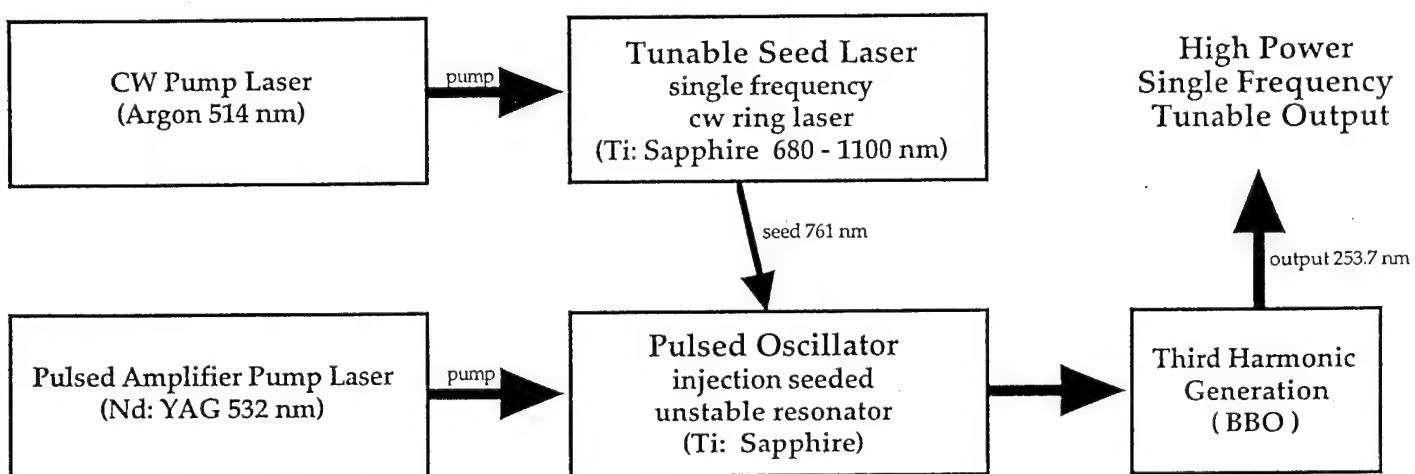


Figure 9. Major elements of tunable, high power Ti:Sapphire laser system.

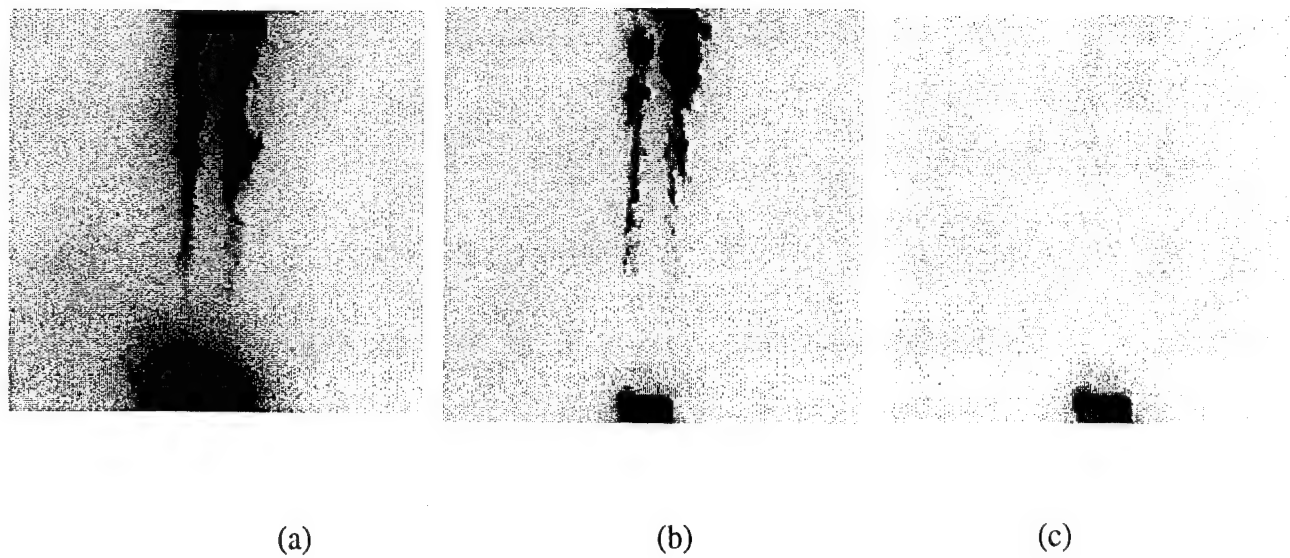


Figure 10. UV-FRS images off supersonic air jet.  
(a) Off resonance.  
(b) Background suppressed.  
(c) Background and flow suppressed.

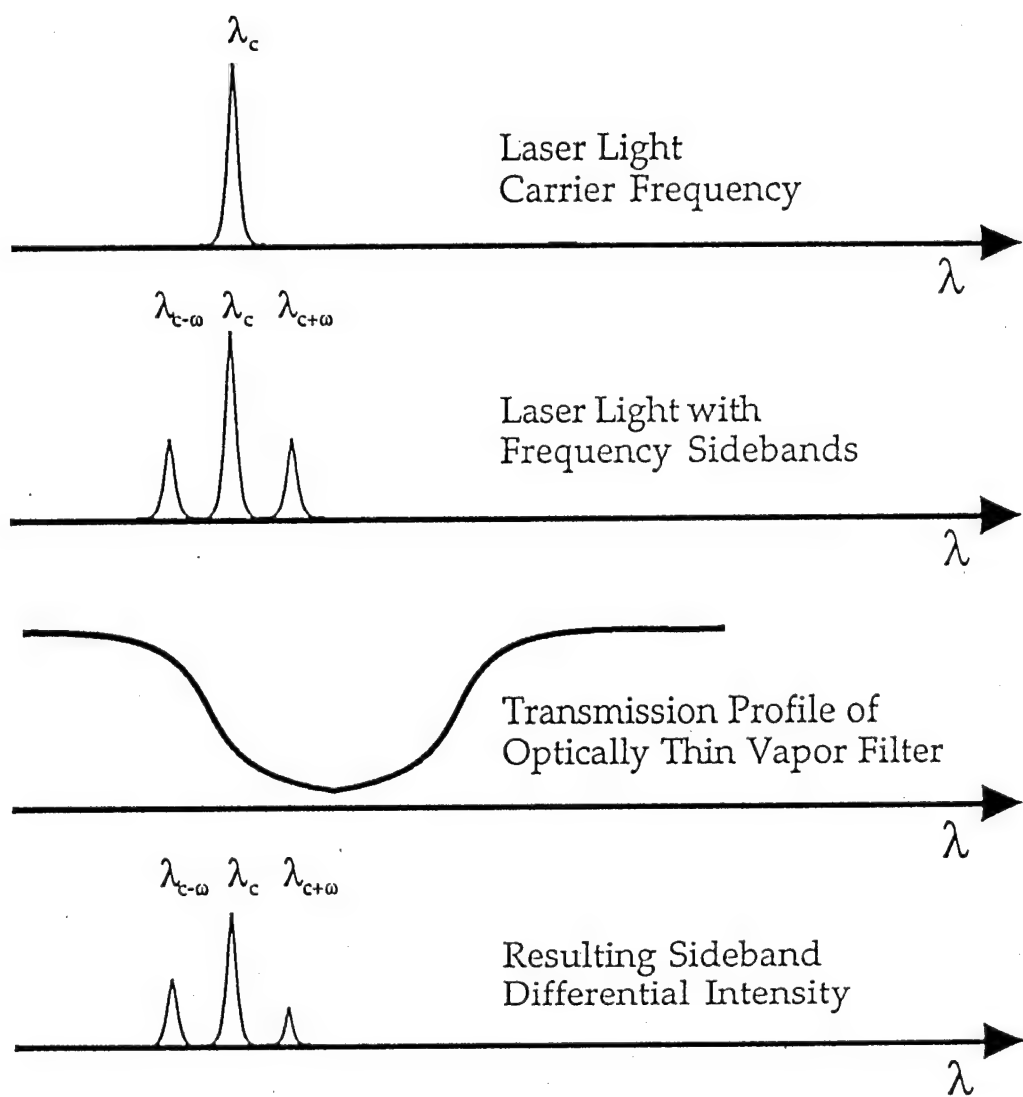


Figure 11. Illustration of basic FM-FRS concept.

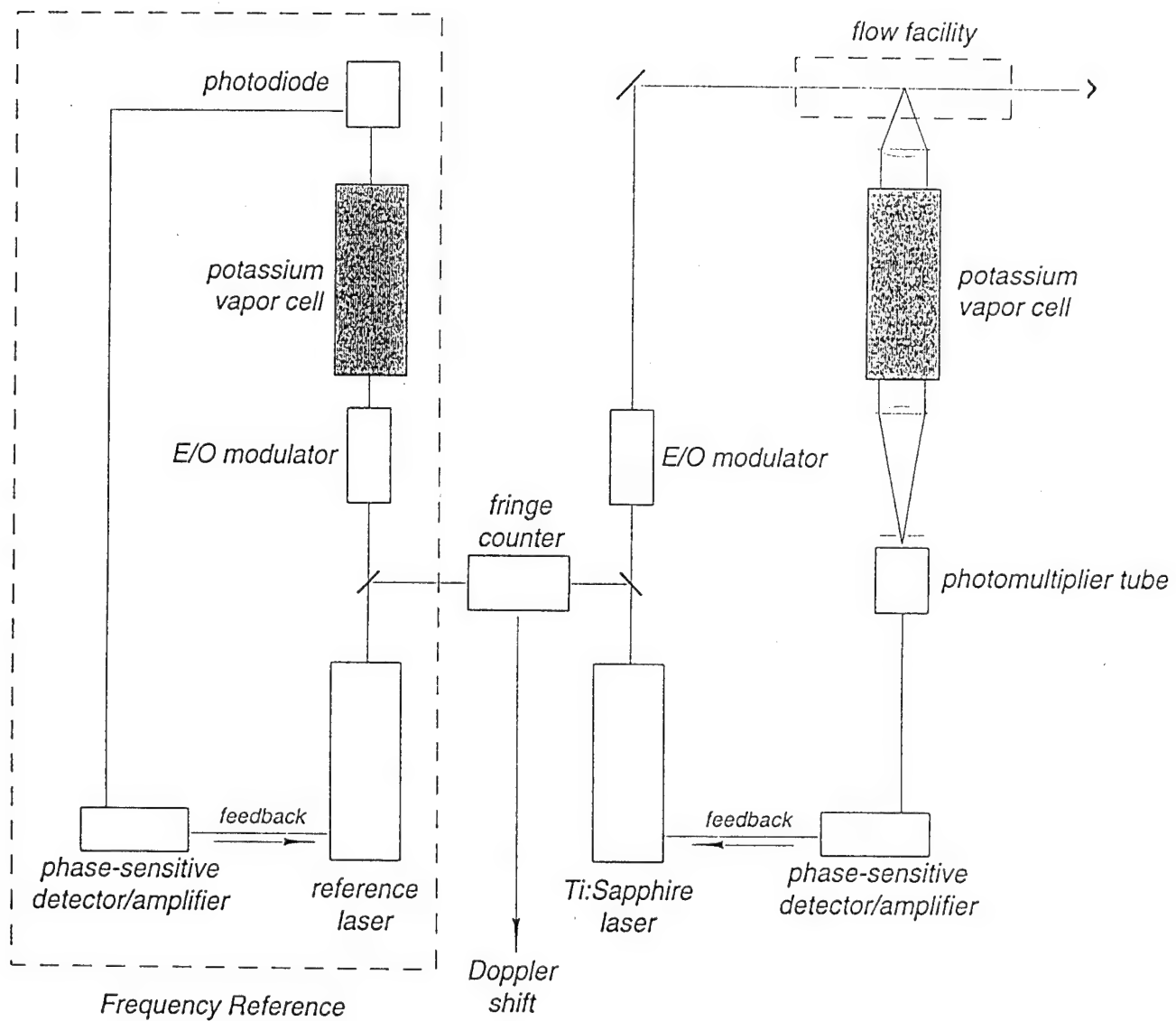


Figure 12. FM-FRS measurement schematic.

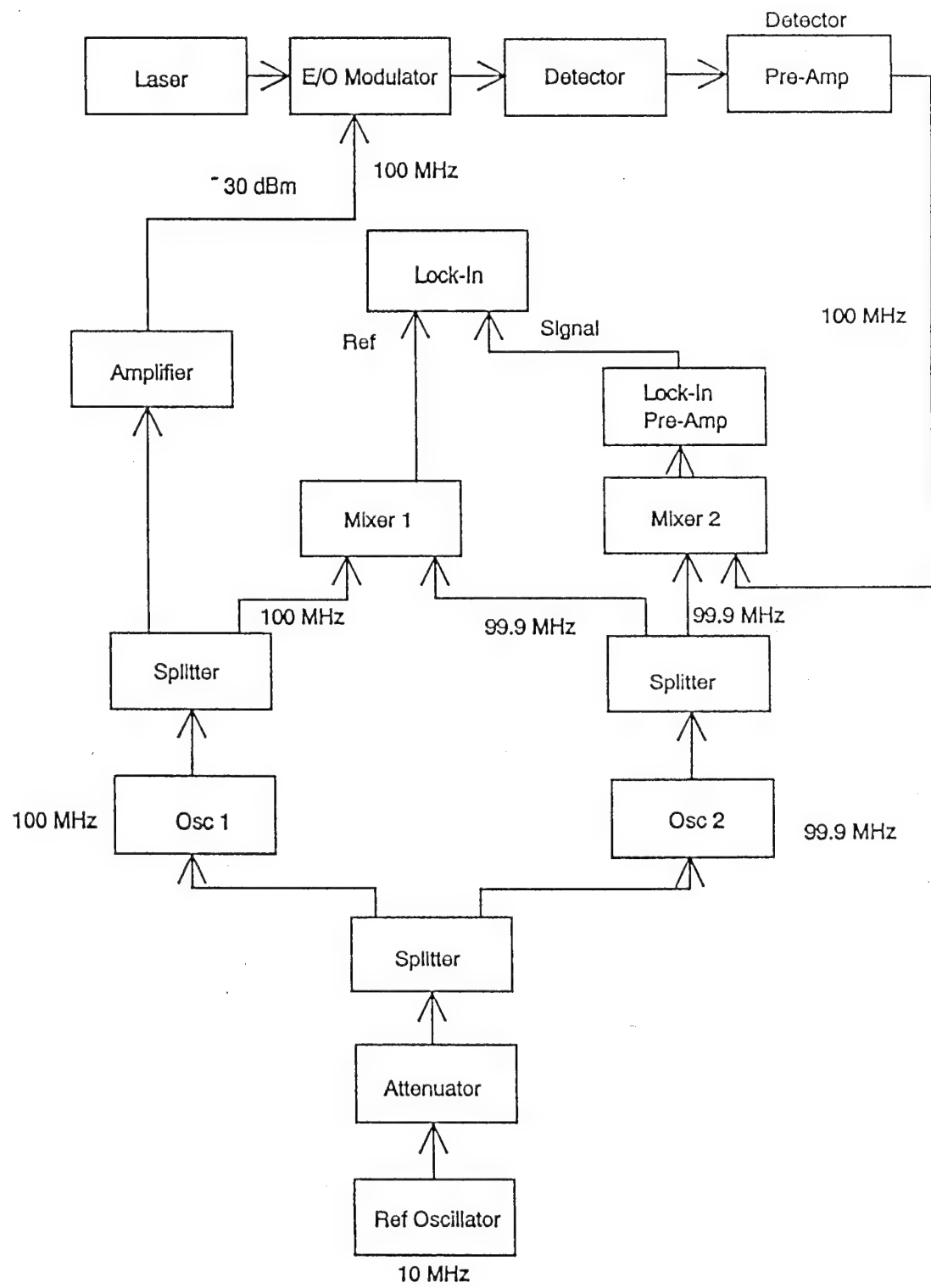


Figure 13. FM-FRS modulation scheme.

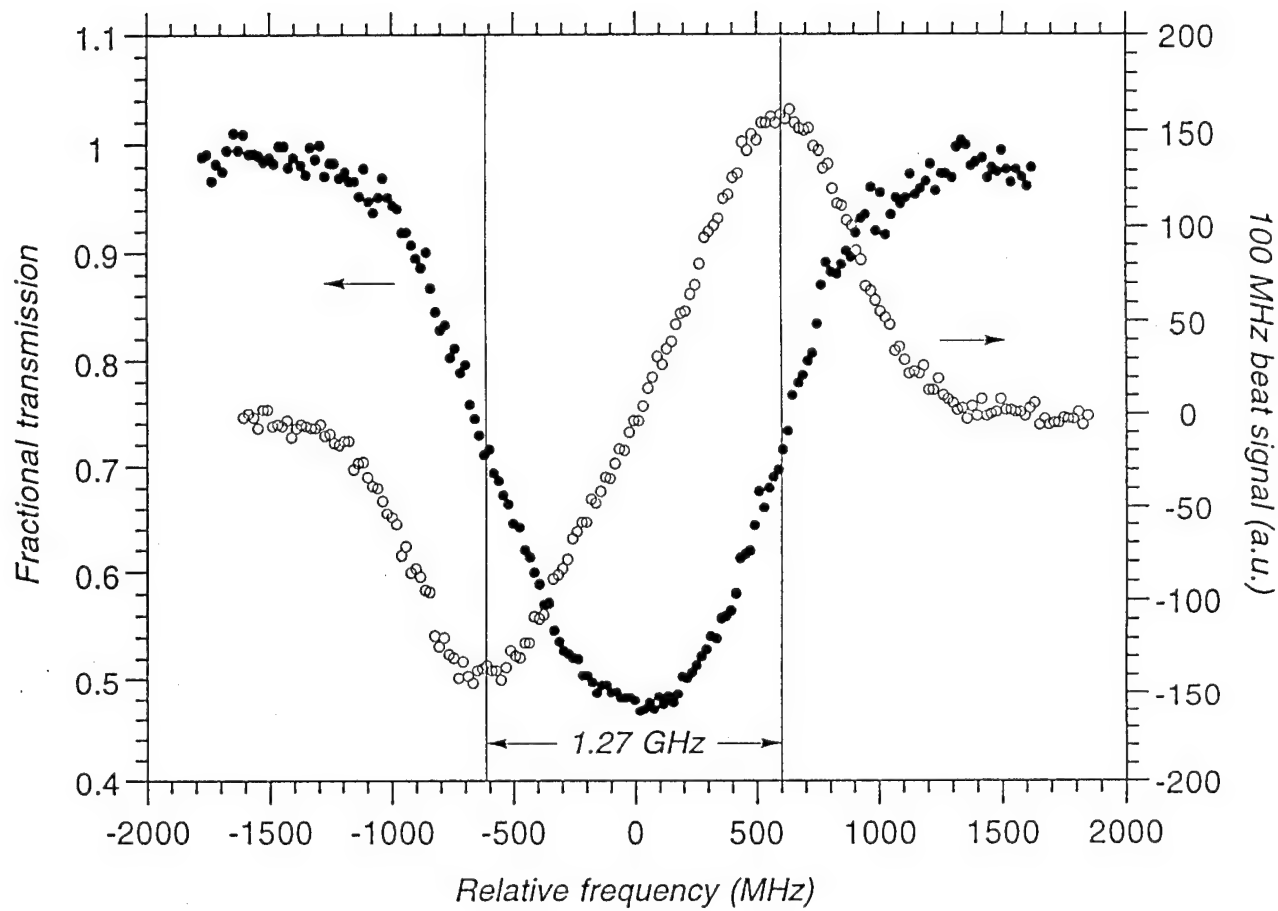


Figure 14. Experimental FRS (●) and FM-FRS (○)scattering spectra.

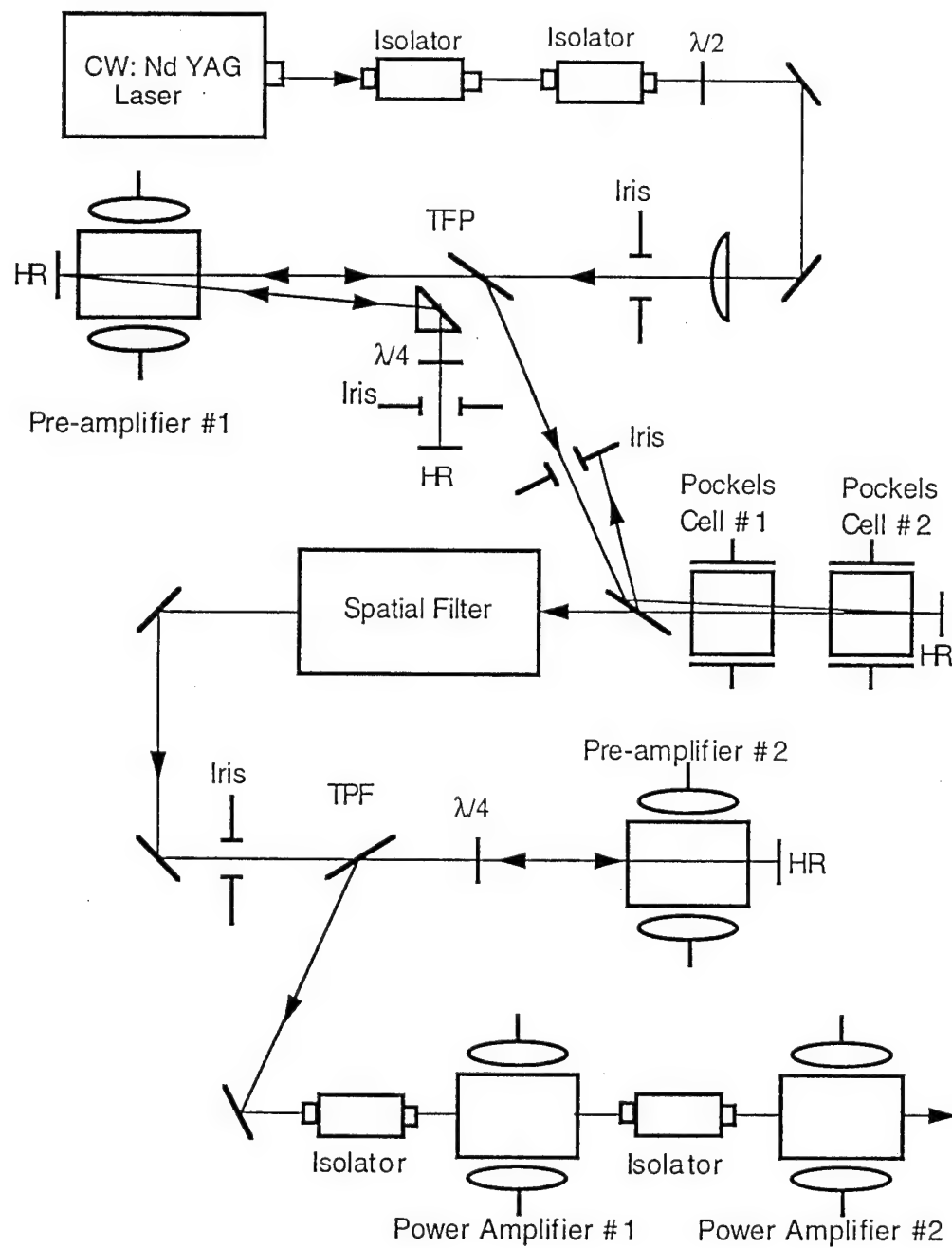
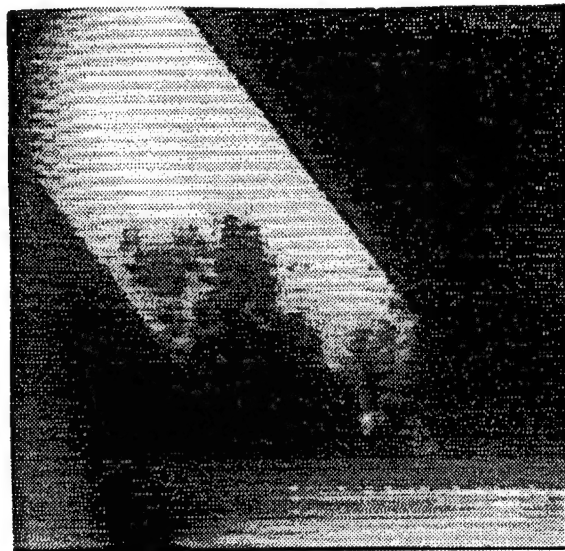


Figure 15. Schematic diagram of Nd:YAG pulse burst laser system.



(a)



(b)



(c)

Figure 16. Filtered Rayleigh images of a Mach 3 high Reynolds number boundary layer at different instances during the laser frequency scan.  
(a) Outside of resonance.  
(b) Background suppressed.  
(c) Near the cut-off point for the flow field.

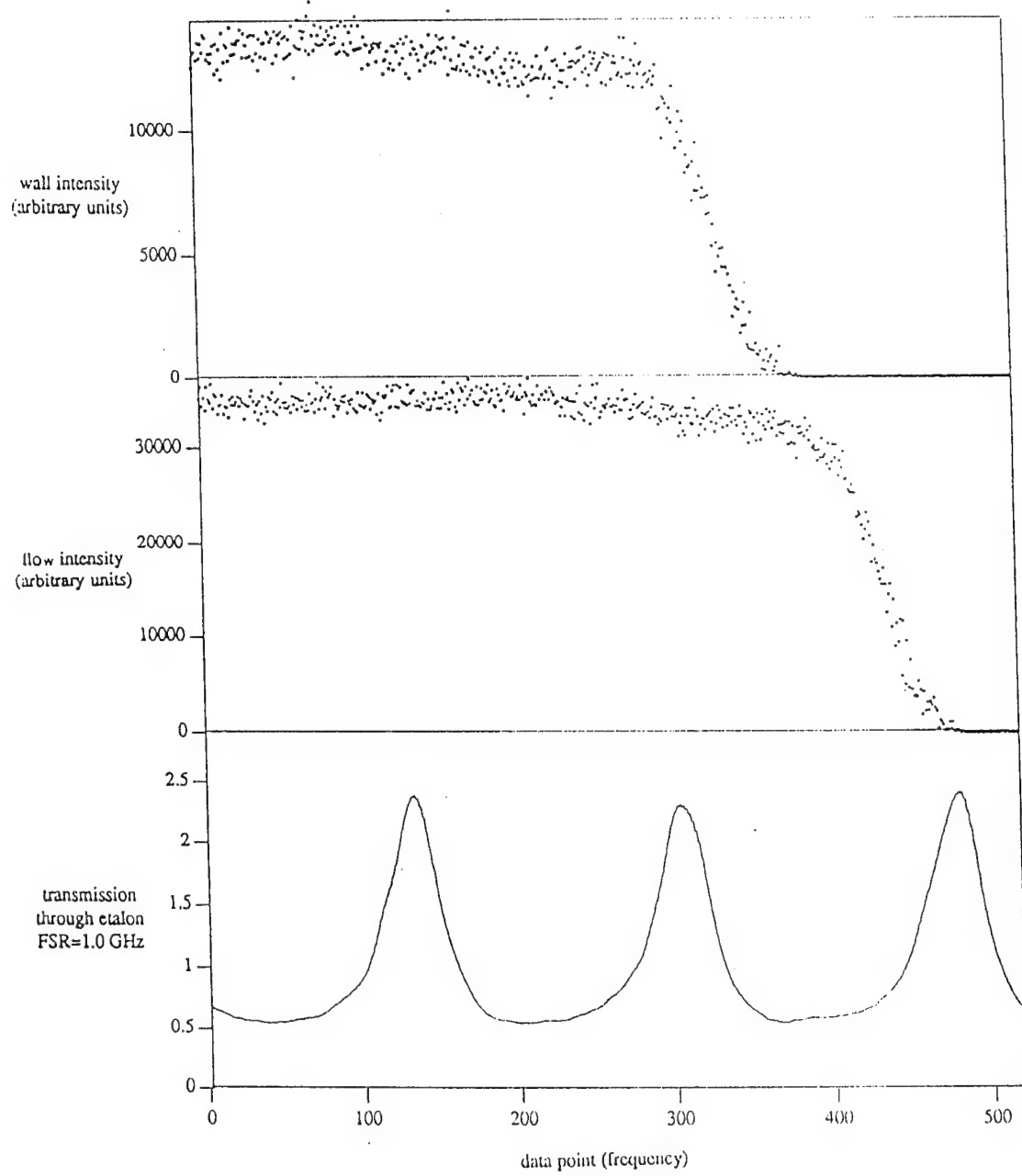


Figure 17. Experimental FRS velocity data from Mach 3, 8" x 8" wind tunnel. Top trace is scattering from walls. Middle trace is scattering from flow. Lower trace is etalon scan of relative laser frequency.

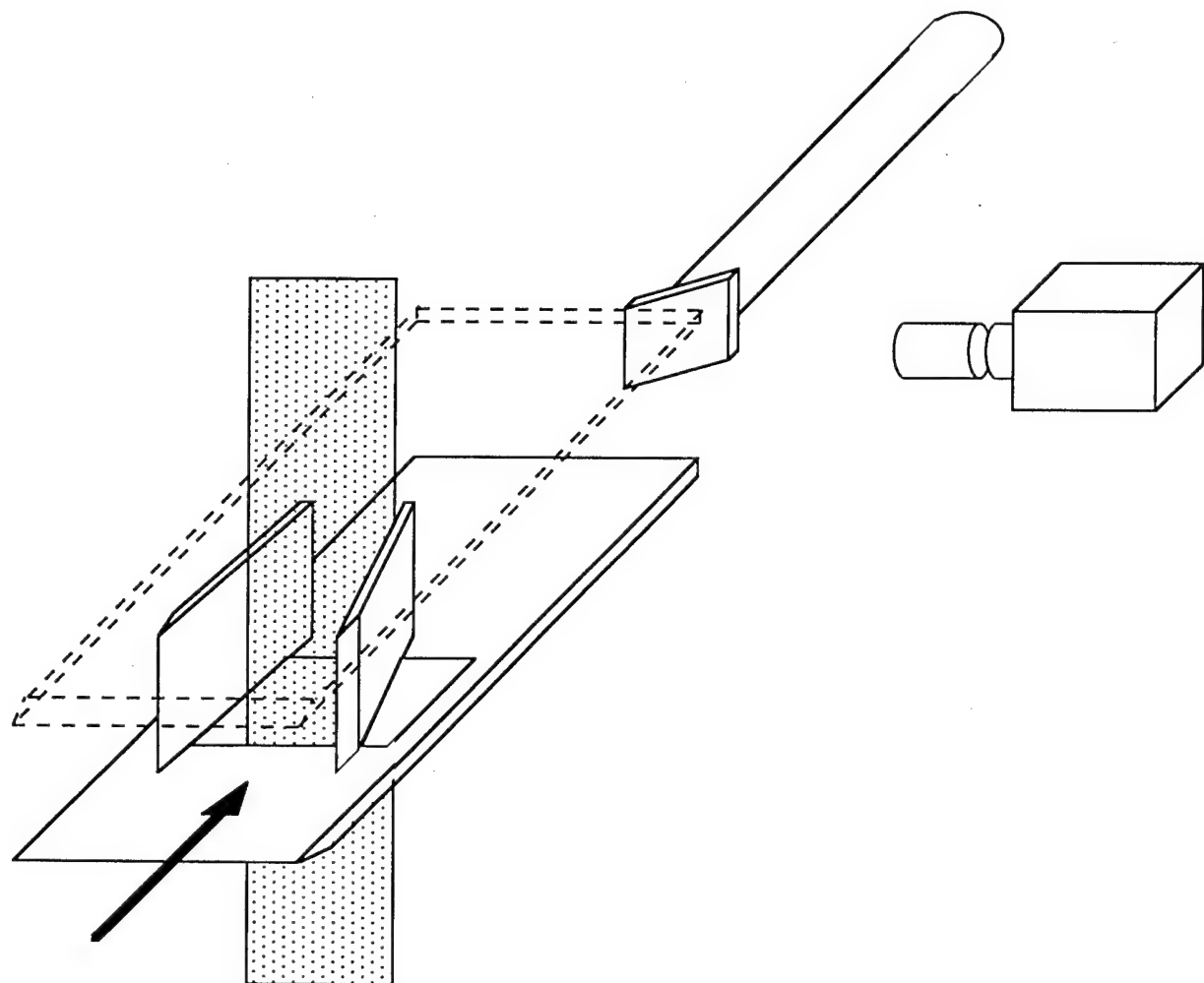


Figure 18. Experimental schematic of FRS measurement in Mach 3 inlet model.

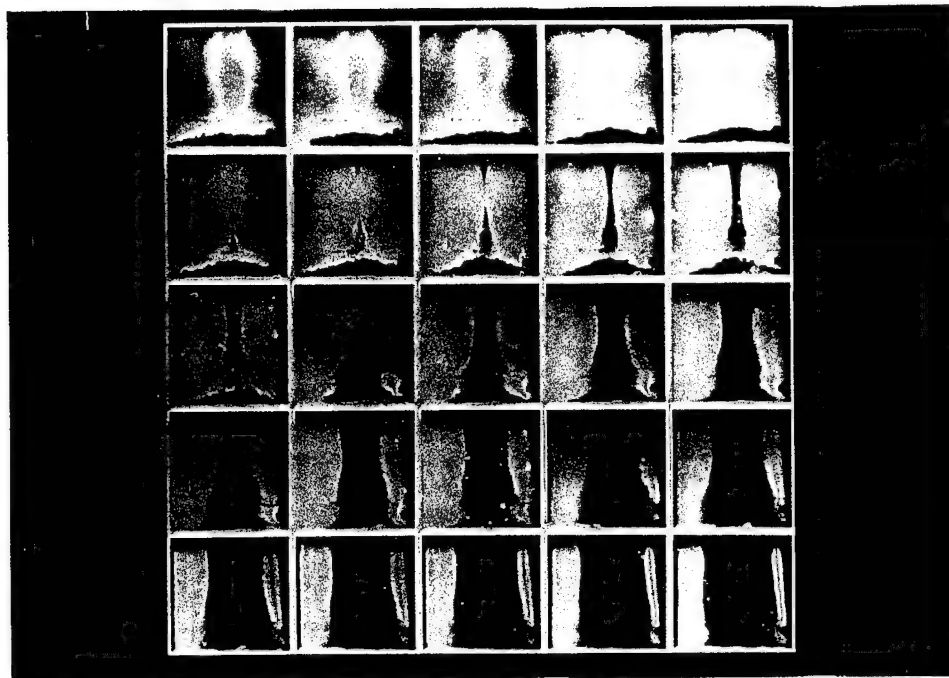
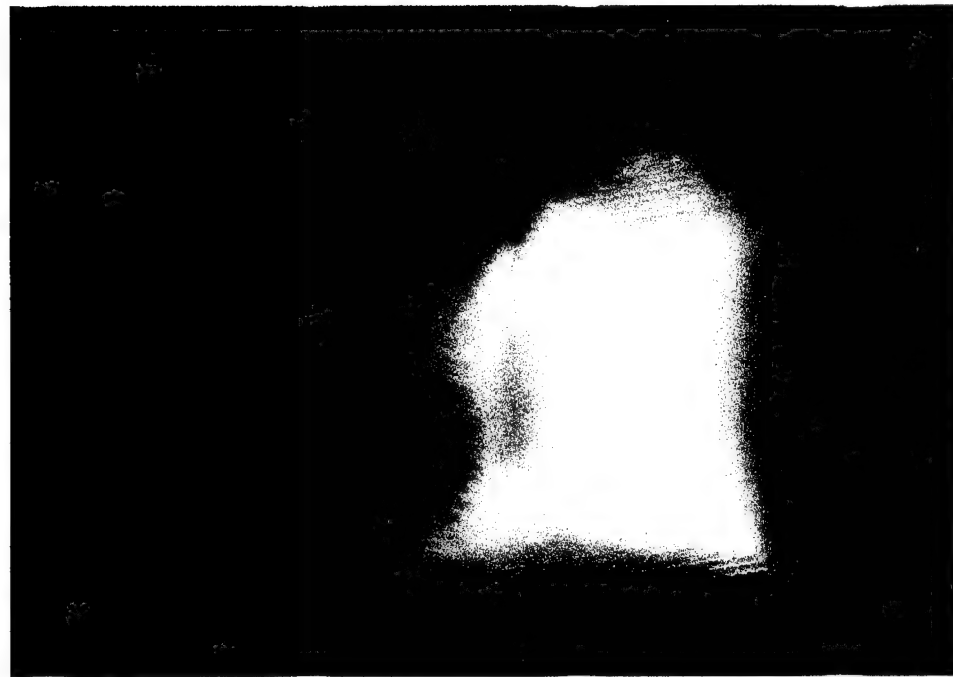
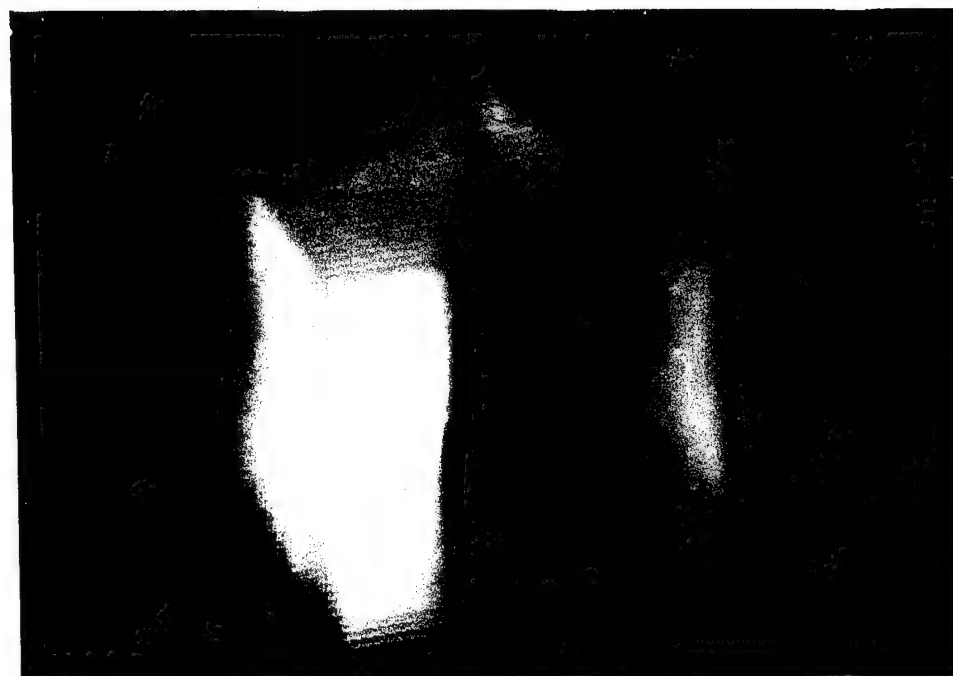


Figure 19. 3 inch by 3 inch slices of data showing shock structure and bottom plate boundary layer. The image on the top left was taken 12.4 inches downstream of the leading edge of the flat plate. Subsequent images were separated from each other by 0.1 inches.



(a)



(b)

Figure 20. Three-dimensional reconstruction of data from Fig. 19.

- (a) Observer looking downstream from before crossing shock.
- (b) Observer looking upstream from behind crossing shock.

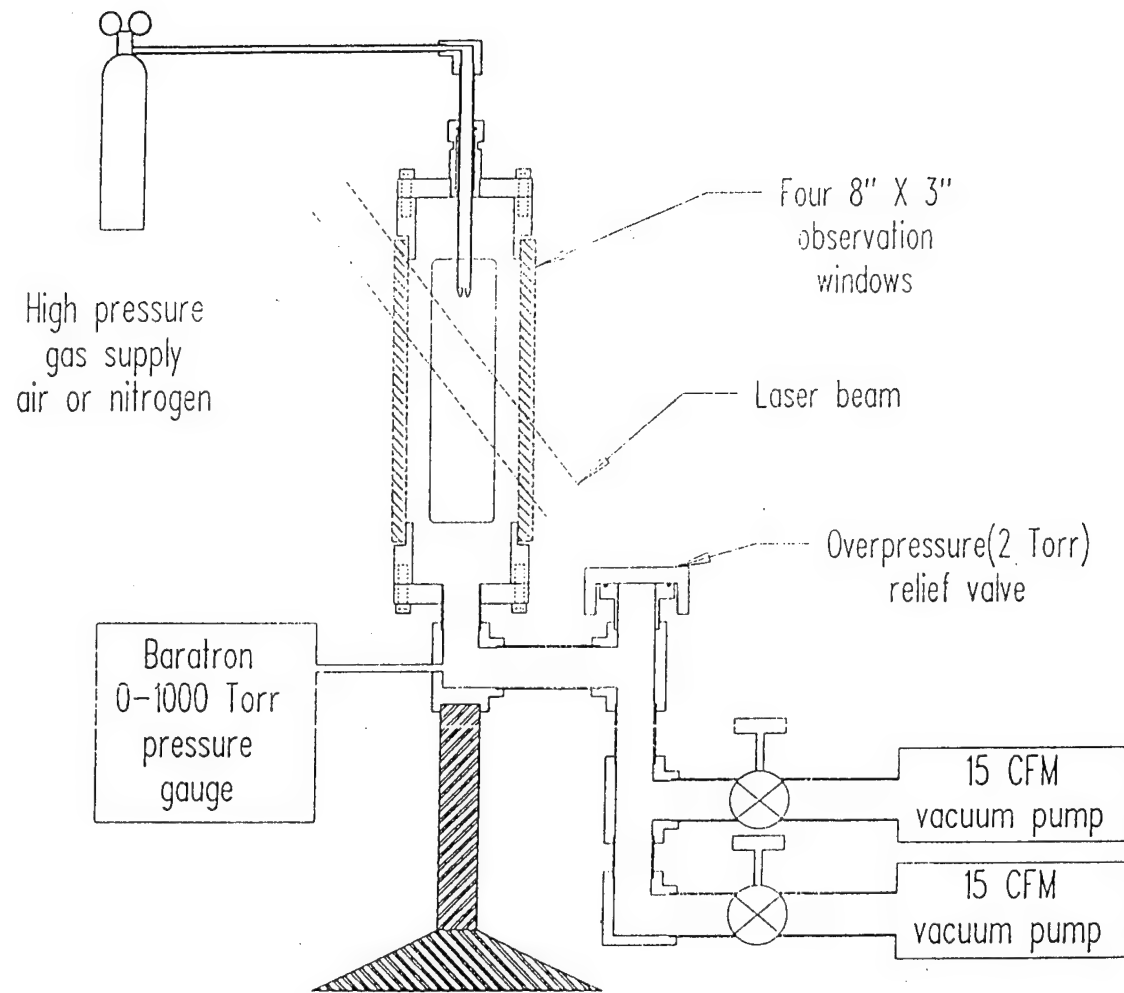


Figure 21. Schematic diagram of Mach 5  $\text{N}_2$  free jet facility.

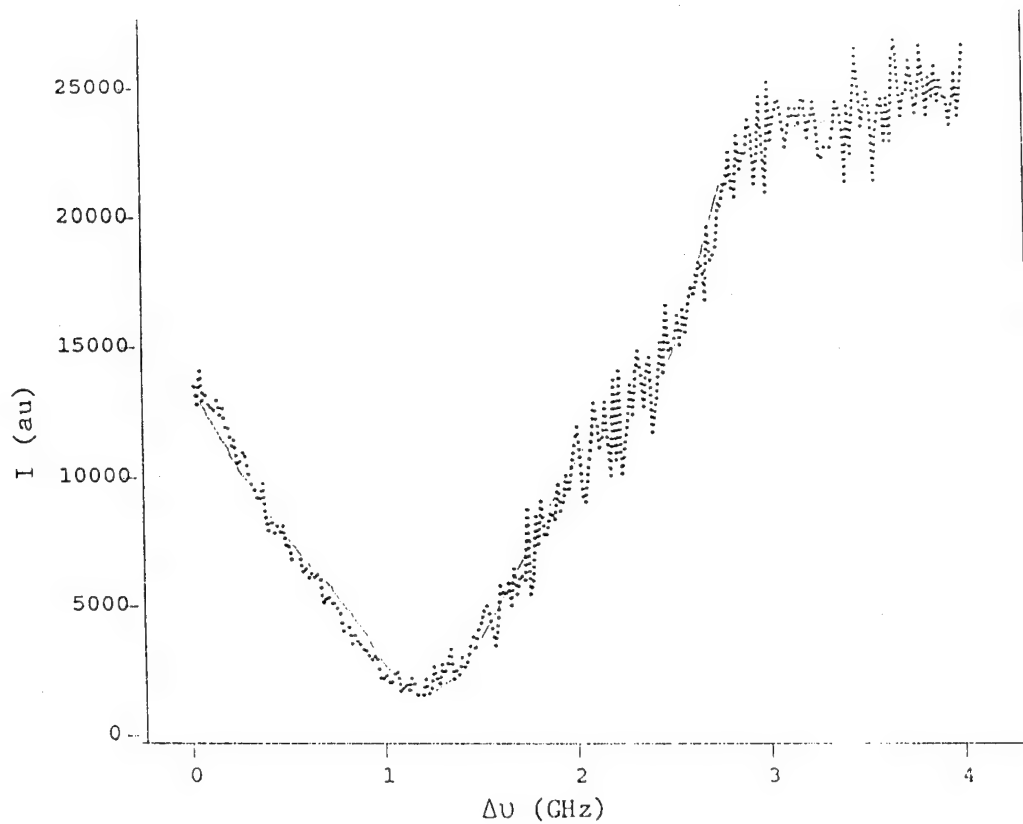


Figure 22. Experimental data (pts) and least-squares fit (solid curve) for time-mean velocity, temperature, and density measurement in Mach 5 flow.

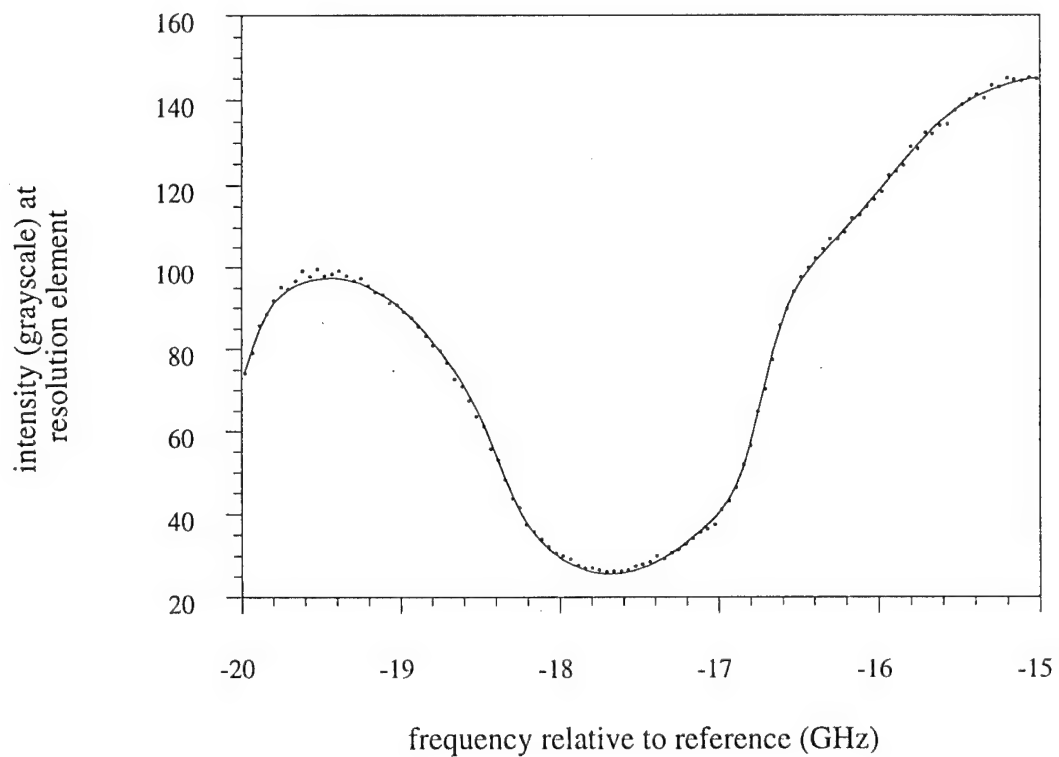
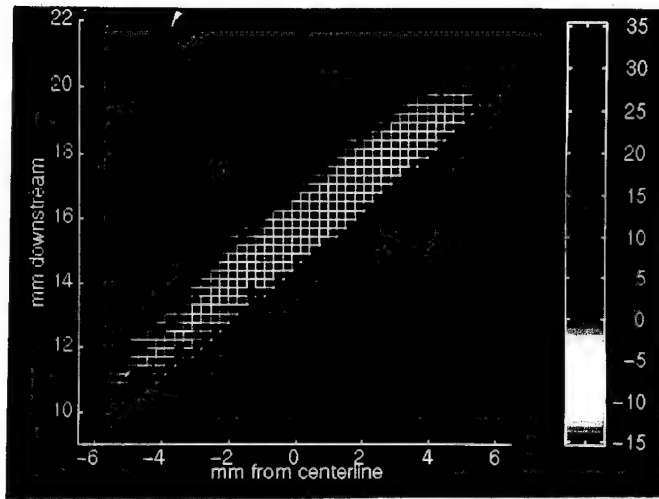
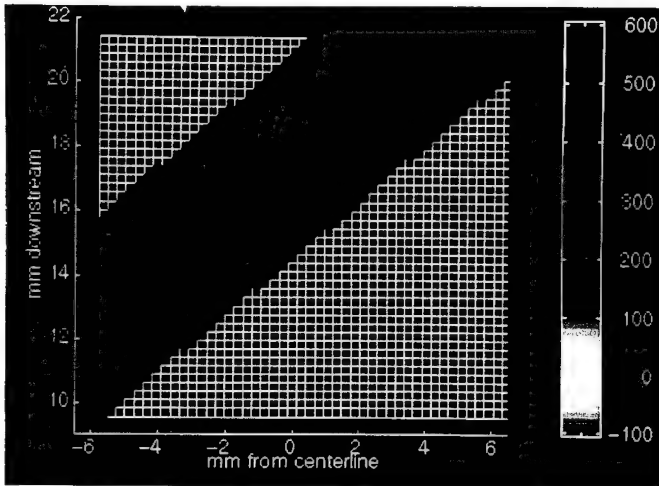


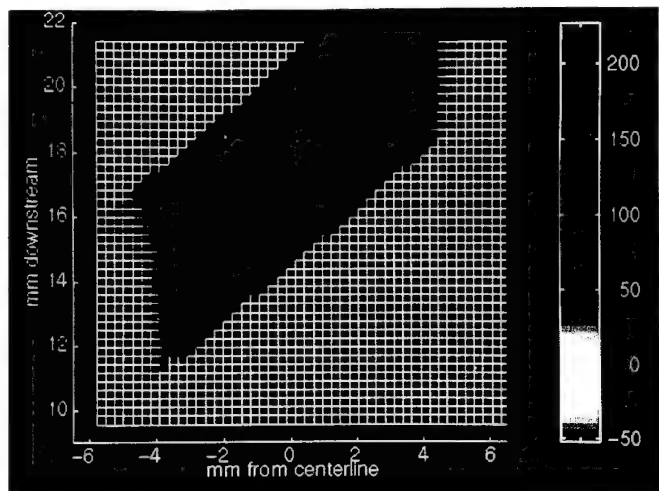
Figure 23. Experimental FRS spectrum (dotted) and least-squares fit (solid) for ambient air measurement.



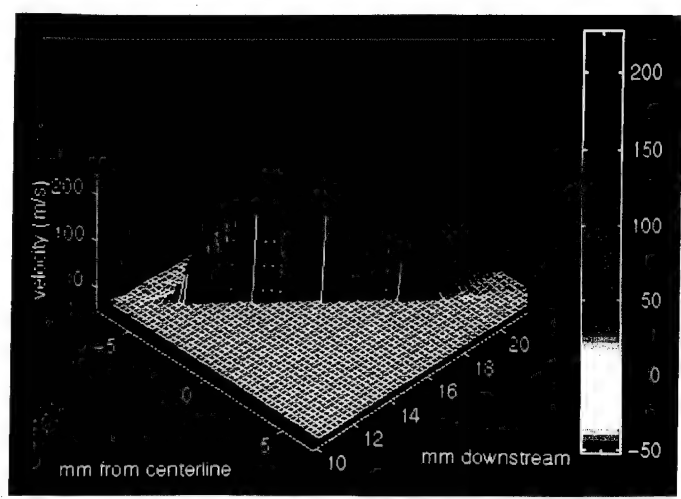
C. Fig. 1: Measured velocity in the direction of FRS sensitivity, of ambient air. Large values at the top of the laser sheet are due to low laser energy.



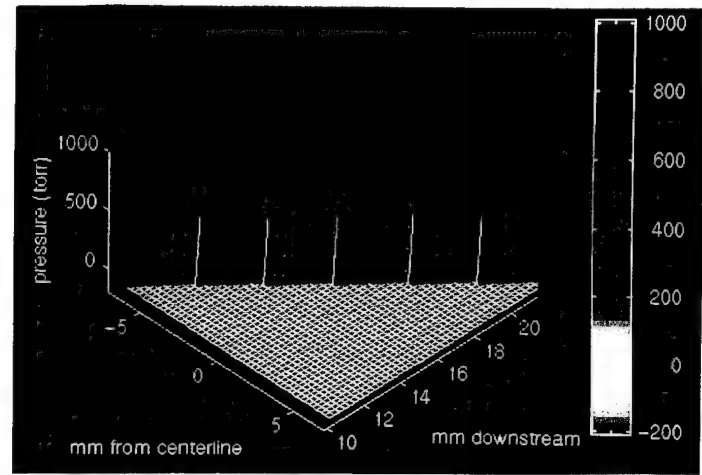
C. Fig. 2: Calibration of R for ambient air. Variation of R across laser sheet is an indication of the variation in laser intensity.



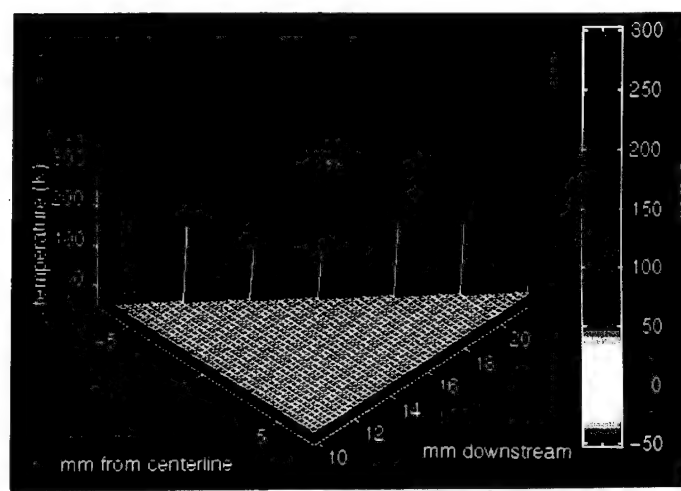
C. Fig. 3: Measured velocity in direction of FRS sensitivity, of Mach 2 free jet.



C. Fig. 4: 3-D plot of velocity in direction of FRS sensitivity, of Mach 2 free jet



C. Fig. 5: Measured static pressure of Mach 2 free jet.



C. Fig. 6: Measured static temperature of Mach 2 free jet.

## **APPENDIX A: PERFORMANCE SUMMARY**

### **Research Personnel**

### **Associated Students**

### **Collaborations**

### **List of Researchers Using Princeton Iodine Model**

### **Presentation List**

### **Publication List**

## RESEARCH PERSONNEL

1. Richard B. Miles, Professor, Principal Investigator
2. Walter R. Lempert, Research Scientist, Co-Principal Investigator
3. Philip Howard, Technical Staff

## ASSOCIATED STUDENTS

1. Joseph Forkey (supported by NASA/Lewis)
2. George Williams (supported by AASERT)
3. Noah Finkelstein
4. Ping-Fang Wu

## COLLABORATIONS

### 1. Princeton Faculty

Seymour M. Bogdonoff -- 3D Inlet Flow.  
Alexander Smits -- High Reynold's Number Boundary Layer Imaging  
Giancinto Scoles (Chemistry) -- Ti:Sapphire Laser Development  
Kevin Lehmann (Chemistry) -- Ti:Sapphire Laser Development

### 2. Industry

Schwartz Electro-Optics (Concord, MA): NASA Ames Phase I and Phase II SBIR's:  
A Study of Laser-Based Instrumentation for Nonintrusive Diagnostics of  
Hypersonic Reactive Flows.  
M.L. Energia (Princeton, NJ): Army Phase I SBIR: Fluctuating Flow Measurements  
Over a Wide Mach Number Range.  
M.L. Energia (Princeton, NJ): U.S. Air Force--Arnold Engineering Development Center  
Phase I SBIR: Fluctuating Flow Field Velocity Measurements Using Frequency  
Modulated-Filtered Rayleigh Scattering.  
Princeton Scientific Instruments, Inc. (Monmouth Junction, NJ): Phase I and Phase II  
SBIR's--Wright Patterson Air Force Base: A Novel High-Speed CCD Framing  
Camera.

## INDIVIDUALS WHO HAVE REQUESTED PRINCETON IODINE CODE

Dr. Richard Seasholtz, NASA Lewis Research Center  
Dr. Bob McKenzie, NASA Ames Research Center  
Prof. Joe She, Colorado State University, Physics Dept.  
Dr. Karl Hoppel, Naval Research Laboratory  
Dr. Mike Smith, NASA Langley Research Center  
Prof. Ed Eloranta, University of Wisconsin, Madison  
Dr. R. Schodell, Institute for Propulsion Technology, DLR, Germany  
Prof. M. Otugen, Polytechnic University, Brooklyn

## PRESENTATION LIST

### **A. Scheduled for 1995:**

May 21-26, 1995 "Frequency Modulated-Filtered Rayleigh Scattering (FM-FRS): A New Velocimetry Technique," CLEO/QELS '95, Baltimore, MD (W.R. Lempert, J. Grinstead, N. Finkelstein, and R.B. Miles).

May 21-26, 1995 "Mercury Vapor Filter and UV Laser System for Rayleigh LIDAR," CLEO/QELS '95, Baltimore, MD (N. Finkelstein, W.R. Lempert, and R.B. Miles)

### **B. Presented 1992-94**

Sept. 28, 1992 "Optical Air Data System," presentation to Wright Aeronautics Labs Representatives, Princeton University.

Oct. 28-29, 1992 "Molecular Methods for Diagnostics," presented to NASA Workshop on Enhanced Turbulent Mixing for HSCT Take-Off Noise Reduction, Williamsburg, Virginia (R. Miles). (Invited)

Jan. 18-21, 1993 "Optically-Based Air Data Using Doppler-Shifted, High Spectral Resolution LIDAR," OSA High Resolution Spectroscopy First Topical Meeting, Salt Lake City, Utah (W.R. Lempert, J. Forkey, N. Finkelstein, and R. Miles).

Feb. 25, 1993 "Imaging of Fluid Flows by Precision Spectroscopy and Nonlinear Optics," Vanderbilt University (R. Miles). (Invited)

Apr. 13, 1993 "PHANTOMM, RELIEF, and Filtered Rayleigh Scattering: A Renaissance in Flow Diagnostics," ONERA, Chatillon, France (R. Miles).

Aug. 30-31, 1993 "Imaging the Turbulent Density Field Near a Window by Filtered Rayleigh Scattering," AFOSR Workshop on Image Reconstruction and Aero-Optic Metrology in Turbulence, Albuquerque, NM (R. Miles).

Sept. 28, 1993 "Tracking Molecular Motion and Imaging Temperature, Velocity, and Density in Unseeded Air," Euromech 309 Colloquium, Gottingen, Germany (R. Miles).

Nov. 17, 1993 "Making Light of Turbulence," Princeton Plasma Physics Laboratory Colloquium, Princeton, New Jersey (R. Miles).

Nov. 22, 1993 "Shedding Light on Turbulence," American Physical Society Division of Fluid Dynamics Annual Meeting, Albuquerque, NM (R. Miles).

Jul. 11-14, 1994 "Precision Whole Field Velocity Measurements with Frequency Scanned Filtered Rayleigh Scattering," 7th International Symposium on Applications of Laser Techniques to Fluid Mechanics, Lisbon, Portugal (R. Miles).

## PUBLICATION LIST

### **A. Submitted for 1996:**

W.R. Lempert, P-F Wu, and R.B. Miles, "Pulse Burst Laser System for High-Speed Flow Diagnostics," (Abstract submitted to the AIAA 34th Aerospace Sciences Meeting, Reno, Nevada, January 15-18, 1996).

J.H. Grinstead, W.R. Lempert, N.D. Finkelstein, and R.B. Miles, "Frequency Modulated-Filtered Rayleigh Scattering (FM-FRS): A New Technique for Real-Time Velocimetry," (Abstract submitted to the AIAA 34th Aerospace Sciences Meeting, Reno, Nevada, January 15-18, 1996).

N.D. Finkelstein, W.R. Lempert, and R.B. Miles, "Application of Narrow Bandwidth Ti:Sapphire Laser to UV Scattering Diagnostics," (Abstract submitted to the AIAA 34th Aerospace Sciences Meeting, Reno, Nevada, January 15-18, 1996).

### **B. Published 1992-95**

R.B. Miles, J.N. Forkey, and W.R. Lempert, "Filtered Rayleigh Scattering Measurements in Supersonic/Hypersonic Facilities," Paper #AIAA-92-3894, AIAA 17th Aerospace Ground Testing Conference, Nashville, TN, July 6-8, 1992.

R. Miles, W. Lempert, and J. Forkey, "Filtered Rayleigh Imaging of Velocity, Temperature, and Density in Hypersonic Flows for the Study of Boundary Layers, Shock Structure, Mixing Phenomena, and the Acquisition of In-Flight Air Data," New Trends in Instrumentation for Hypersonic Research, ONERA, France, April 27-May 1, 1992. Proceedings published in NATO ASI SERIES E: Applied Sciences, Vol. 224, "New Trends in Instrumentation for Hypersonic Research," (Kluwer Academic Publishers, The Netherlands), p. 391, Ed. A. Boutier, 1993.

J. Forkey, S. Cogne, A. Smits, S. Bogdonoff, W.R. Lempert, and R.B. Miles, "Time-Sequenced and Spectrally Filtered Rayleigh Imaging of Shock Wave and Boundary Layer Structure for Inlet Characterization," Paper #AIAA-93-2300, AIAA/SAE/ASME/ASEE 29th Joint Propulsion Conference and Exhibit, June 28-30, 1993, Monterey, CA.

N. Finkelstein, J. Gambogi, W.R. Lempert, R.B. Miles, G.A. Rines, A. Finch, and R.A. Schwarz, "The Development of a Tunable, Single-frequency Ultraviolet Laser Source for UV Filtered Rayleigh Scattering, Paper #AIAA-94-0492, AIAA 32nd Aerospace Sciences Meeting & Exhibit, January 10-13, 1994, Reno, Nevada.

J.N. Forkey, W.R. Lempert, S.M. Bogdonoff, R.B. Miles, and G. Russell, "Volumetric Imaging of Supersonic Boundary Layers Using Filtered Rayleigh Scattering Background Suppression," Paper #AIAA-94-0491, AIAA 32nd Aerospace Sciences Meeting & Exhibit, January 10-13, 1994, Reno, Nevada.

R. Miles, W. Lempert, J. Forkey, N. Finkelstein, and P. Erbland, "Quantifying High Speed Flows by Light Scattering from Air Molecules," Paper #AIAA-94-2230, 25th AIAA Fluid Dynamics Conference, June 20-23, 1994, Colorado Springs, CO.

J. N. Forkey, N.D. Finkelstein, W.R. Lempert, and R.B. Miles, "Control of Experimental Uncertainties in Filtered Rayleigh Scattering Measurements," Paper #AIAA-95-0298, 33rd AIAA Aerospace Sciences Meeting and Exhibit, January 9012, 1995, Reno, Nevada. (Also submitted to the AIAA Journal).

**APPENDIX B**

**Publication Reprints**



**AIAA-93-2300**

**TIME-SEQUENCED AND SPECTRALLY FILTERED RAYLEIGH  
IMAGING OF SHOCK WAVE AND BOUNDARY LAYER  
STRUCTURE FOR INLET CHARACTERIZATION**

**J. Forkey, S. Cogne, A. Smits, S. Bogdonoff,  
W.R. Lempert, and R.B. Miles  
PRINCETON UNIVERSITY  
Department of Mechanical & Aerospace Engineering  
Princeton, New Jersey 08544**

**AIAA/SAE/ASME/ASEE  
29th Joint Propulsion  
Conference and Exhibit**

**June 28-30, 1993 / Monterey, CA**

# TIME-SEQUENCED AND SPECTRALLY FILTERED RAYLEIGH IMAGING OF SHOCK WAVE AND BOUNDARY LAYER STRUCTURE FOR INLET CHARACTERIZATION

Joseph Forkey, Sandrine Cogne,<sup>‡</sup> Alexander Smits,<sup>\*</sup> Seymour Bogdonoff,<sup>\*\*</sup>  
Walter R. Lempert,<sup>†</sup> and Richard B. Miles<sup>††</sup>

Department of Mechanical & Aerospace Engineering  
PRINCETON UNIVERSITY  
Princeton, New Jersey 08544 U.S.A.  
609/258-5131

## ABSTRACT

The accurate characterization of inlet performance is critical for the optimum design of engines for high-speed flight. The three-dimensional nature of the inlet flow leads to complex shock structures, vorticity, and shock wave/boundary layer interactions. New Rayleigh imaging techniques show great promise of achieving this goal by providing instantaneous images of shock wave and boundary layer structures. Rayleigh scattering is also capable of producing rapidly time-sequenced images of boundary layer evolution and capturing details of shock wave/boundary layer interactions.

In previous work we have demonstrated the utility of ultraviolet Rayleigh imaging for the observation of supersonic flow structure and the potential of spectrally filtered Rayleigh imaging for the suppression of background scattering from windows and walls and the measurement of flow field velocity.<sup>1,2</sup> In this paper we present time-sequenced Rayleigh images taken with a visible, double-pulsed laser system which show the evolution of boundary layer structure and shock wave/boundary layer interactions. In addition, we present filtered Rayleigh images which map out the full three-dimensional shock wave and boundary layer structure of the internal flow in a generic cross-shock inlet. The intent of the work presented here is to examine the utility

of multiple pulsed Rayleigh imaging and Filtered Rayleigh Scattering for imaging complex flows in research-scale, high Reynolds number supersonic flow facilities.

## DOUBLE-PULSED IMAGES

The double-pulsed Rayleigh images are taken with a Continuum double Q-switched Nd:YAG laser whose pulses can be separated in time from as little as 15  $\mu$ secs to as much as 200  $\mu$ secs. The laser output beam is frequency-doubled to the green (0.532 microns) and expanded into a thin sheet which is passed through the flow to generate a stream-wise cross-sectional image. The pulses are approximately 10 nsec in duration, so even the high frequency fluctuations are time-frozen in the images.

Two sets of experiments were run. The first was performed using two separate cameras observing the same flow regime from opposite sides of the tunnel, while the second made use of a single high-speed framing camera to capture two time-sequenced images from the same observation point. The two cameras are double-intensified CID devices which are downloaded onto videotape for analysis. The framing camera is a Hadland Imacon 792 which generates a normal film image. Figures 1 and 2 show image pairs of the time-evolving boundary layer structure taken 20  $\mu$ secs apart (Fig. 1) and 60  $\mu$ secs apart (Fig. 2) using the two-camera geometry. In each case, one of the camera images was reversed to yield image pairs with the flow moving from right-to-left. The resolutions and gains of the two cameras were not precisely matched, so some care must be taken when comparing image pairs. The figures indicate, however, that small scale structure can grow rapidly over relatively short distances. An example of that growth can be seen particularly well along the upstream edge of the large scale structure in Fig. 2. The orientation and size of the structures are also of importance for the understanding of boundary layer physics. The displacement of the observed structures versus distance from the wall gives a quantitative

<sup>‡</sup> Present Address: E.S.E.M., 45067 Orleans, Cedex 02  
FRANCE

<sup>\*</sup> Professor, Mechanical & Aerospace Engineering,  
Member AIAA

<sup>\*\*</sup> Professor, Mechanical & Aerospace Engineering,  
Fellow, AIAA

<sup>†</sup> Research Scientist, Mechanical & Aerospace  
Engineering, Member AIAA

<sup>††</sup> Professor, Mechanical & Aerospace Engineering,  
Senior Member AIAA

measure of the convection velocity versus position. Fig. 3 shows a distribution plot of velocities of these structures normalized to the free stream velocity as a function of position normalized to the boundary layer thickness. The figure also shows average velocities measured by RELIEF flow tagging and by pitot surveys.<sup>3</sup> Note that the velocities measured from the displacement of the structures are generally lower than those measured by pitot tube and RELIEF measurements at the same location in the boundary layer. This suggests that either the structures move slower than the average flow, or the measurement techniques may be biased. Further discussion of the boundary layer physics that can be extracted from this data is given in Ref. 4.

The number of Rayleigh sample points near the wall is limited since samples can only be taken at the interface between the hot wall fluid and the cold core flow. This is the so because the predominant scatterer in the flow field is a residual ice crystal fog which occurs even though the air is carefully dried with silica gel at high pressure before passing into the wind tunnel facility. In the absence of this fog, the camera gain can be turned up and scattering from the molecules in the flow field itself can be recorded. If the fog is present, however, images record the thermal sublimation contour where the ice crystal fog vaporizes. This fog is observed in virtually all high pressure air-supplied blowdown facilities.<sup>5</sup> In some cases, the fog is augmented by bypassing the silica gel dryers in order to provide higher signal levels for flow field visualization.<sup>6</sup>

Figure 4 shows a pair of images of a shock wave/boundary layer interaction taken over a 16° angle wedge in the 8" x 8" high Reynolds number Mach 3 facility. Once again, these images were taken using two cameras observing from opposite sides, and the bottom image was taken 40  $\mu$ secs after the top. It is interesting to observe how the boundary layer structure is modified as it passes through the shock generated by the wedge. For example, in the top picture at the center, one can see a well defined flow feature moving towards the shock. In the lower image, this feature has passed through the shock and has been compressed in the direction perpendicular to the shock, but still maintains a recognizable structure. Similar image pairs taken from the same data set show that the boundary layer structure drives the shock motion and causes significant distortion of the shock front in the boundary layer regime.

The images shown in Figs. 5a and 5b were taken using the high-speed framing camera. Since these images were both taken with the same camera from the same perspective, they can be directly compared for a more quantitative evaluation of flow evolution. Images are again shown with the flow moving from right-to-left. The first image is on the right, and the second, taken 40  $\mu$ secs later, is on the left. Here, again, individual flow structures can be observed passing through the shock wave.

## FILTERED RAYLEIGH SCATTERING IN AN INLET

The double-pulsed images were taken using straightforward Rayleigh imaging together with careful masking and a high sensitivity camera. While the boundary layer and shock features can be observed in the outer portion of the boundary layer and in the core region of the flow, strong background scattering obscures many of those features near the wall. In addition, background scattering from windows and walls degrades the image quality, particularly in complex geometries, and where a lower signal level, due to scattering from the air itself rather than the ice vapor fog is observed. In order to suppress this background scattering, a narrow linewidth, injection-locked Nd:YAG laser is used, and the frequency-doubled output is tuned to precisely overlap a strong spectral absorption line in iodine vapor. By placing an iodine vapor cell in front of the camera, scattering from windows and walls is absorbed. The scattering from the flow field, however, is Doppler-shifted, due to the motion of the air molecules and ice crystals, and, therefore, passes through the filter and is seen by the camera. This approach is called Filtered Rayleigh Scattering and is used to significantly enhance the quality of the Rayleigh images.<sup>2</sup>

To demonstrate the utility of this background suppression feature, Filtered Rayleigh Scattering has been used to capture shock wave and boundary layer structure in a simple, generic cross-shock inlet model placed in our Mach 3 high Reynolds number facility. A sketch of the experimental geometry is shown in Fig. 6. The inlet has an opening of approximately 4" in height by 6" in width. It is bounded by two parallel plates on the upper and lower surfaces, and variable angle fins on the sides. The fins are set back 7.6" behind the leading edges of the top and bottom plates and are each 9" long. They end 5" before the end of the plates. These fins generate a pair of shocks which cross downstream in the inlet and lead to complex three-dimensional flow structures. Of particular interest in this study is the shock curvature and the impact that the crossing shocks have on the upper and lower boundary layers.

In order to examine this flow, the injection-locked, frequency-doubled Nd:YAG laser was expanded to a sheet which passed through windows in the upper and lower walls in the wind tunnel facility and in the upper and lower plates of the inlet model. The sheet was oriented so that it was normal to the incoming flow direction. Thus, an instantaneous cross-sectional image of the flow could be captured with each laser pulse. A 45° mirror was placed in the flow downstream of the inlet model so these transverse images could be recorded with a camera located outside of the flow. This geometry is particularly attractive for Filtered Rayleigh Scattering since the collected light is scattered with large Doppler-shifted frequency (~1 GHz). A 3.25 inch long iodine vapor filter was placed in front of the camera. As

can be seen in Fig. 7, the absorption bandwidth of this filter is approximately 2 GHz, so if the laser is tuned close to the center of the filter (maximum extinction of background scattering), the light scattered from the flow itself is shifted sufficiently to pass through the filter with little attenuation. Once again, the primary scatterer in the flow field is the ice vapor fog caused by residual water vapor. This geometry is similar to that used for measurements made by Settles and co-workers, however, their model had no top plate.<sup>6,7</sup> They used a copper-vapor laser to illuminate a similar flow that had been "seeded" by by-passing the silica gel dryer.

A series of cross-sectional images taken at Mach 3 with the inlet fins set at an 11° angle relative to the flow axis are shown in Figs. 8a-t. These images were taken in sequential 0.1" steps, in the streamwise direction, passing through the point at which the shock crossing occurs. Each of these images represents an instantaneous cross-sectional image of the flow field. The camera position was moved in synchronization with the laser sheet displacement in order to maintain image focus and magnification. Note that downstream of the crossing point the temperature has increased enough in the flow field to cause the ice crystals to evaporate. The bright scattering from particle "snow" which is seen in some of the images occurs near the end of the wind tunnel run, and its origin is uncertain. The boundary layer throughout the entire scan is warm enough so there are no ice crystals, and it appears black in these images. These images appear similar to those presented by Garrison and Settles for a Mach 3.8 flow with a 15° fin angle.<sup>7</sup> Due to the much lower density of water vapor in these images, the "shadowgraph" effect seen by Garrison and Settles does not occur, and since a high-power pulsed laser is used, the images are captured instantaneously. Much greater shock curvature is seen in the images presented here, perhaps due to the lower Mach number, weaker shocks, or to the presence of a top plate on the inlet. Note that, in addition to the shock curvature, the induced vorticity at the corners sweeps the boundary layer up in the middle of the inlet. This is particularly evident downstream of the shock crossing point.

Since the shocks heat the flow, the ice vapor fog vanishes behind the shock crossing point. At some distance downstream the ice vapor fog is no longer seen in the image plane. At this point the camera gain can be increased so scattering directly from the molecular field can be observed. Figure 9 shows a time-averaged image of molecular scattering taken approximately three inches downstream of the crossing point. It is apparent in this image that the boundary layer has left a residual semi-circular feature in the flow whose character has yet to be fully determined. These images suggest, however, that the density is significantly lower than the free stream flow, and, therefore, this feature represents warm wall fluid that has been swept towards the core of the flow by the induced separation vortices.

## SUMMARY

Multiple pulsed Rayleigh scattering and Filtered Rayleigh Scattering have been used to generate images of complex boundary layer structure, shock wave/boundary layer interactions, and crossing shock waves. These images give instantaneous realizations of the flow field and, in the case of multiple-pulsed lasers, can be used to capture flow field evolution. The images taken in the inlet give insight into the three-dimensional effects caused by the inlet geometry and may provide guidance for modeling of these complex flows.

## ACKNOWLEDGMENTS

This work was supported by the AFOSR under L. Sakell, NASA/Lewis under R. Seasholtz, and NASA/Langley under R. Antcliff. Technical support from W. Stokes, P. Howard, and D. Zhou is gratefully acknowledged.

## REFERENCES

1. M. Smith, A. Smits, and R. Miles, "Compressible Boundary Layer Density Cross Sections by UV Rayleigh Scattering," *Optics Letters* **14**, 1989.
2. R.B. Miles, J.N. Forkey, and W.R. Lempert, "Filtered Rayleigh Scattering Measurements in Supersonic/Hypersonic Facilities," *AIAA-92-3894*, 7th Aerospace Ground Testing Conf., Nashville, TN, July 6-8, 1992.
3. R. Miles, W.R. Lempert, B. Zhang, and I. Glesk, "Rayleigh Imaging and Flow Tagging in Ground Test Facilities," International Congress on Instrumentation in Aerospace Simulation Facilities (ICIASF '91), IEEE Publication # 91CH3028-8, 1991, pp. 255 - 261.
4. S. Cogne, J. Forkey, W. Lempert, R.B. Miles, and A.J. Smits, "The Evolution of Large-Scale Structures in a Supersonic Turbulent Boundary Layer," *ASME Fluids Engineering Conf.*, Washington D.C., June 20-24, 1993.
5. B. Shirinzadeh, M. Hillard, A. Blair, and R. Exton, "Study of Cluster Formation and Its Effects on Rayleigh and Raman Scattering Measurements in a Mach 6 Wind Tunnel," *AIAA-91-1496*, Presented at the AIAA 22nd Fluid Dynamics, Plasma Physics, and Lasers Conference, June 24-27, Honolulu, Hawaii.
6. F.S. Alvi and G.S. Settles, "Physical Model of the Swept Shock Wave/Boundary-Layer Interaction Flowfield," *AIAA Journal* **30**, Sept. 1992, p. 2252.
7. T.J. Garrison and G.S. Settles, "Flowfield Visualization of Crossing Shock-Wave/Boundary-Layer Interactions," *AIAA-92-0750*, 30th Aerospace Sciences Meeting, Reno, Nevada, January 6-9, 1992.

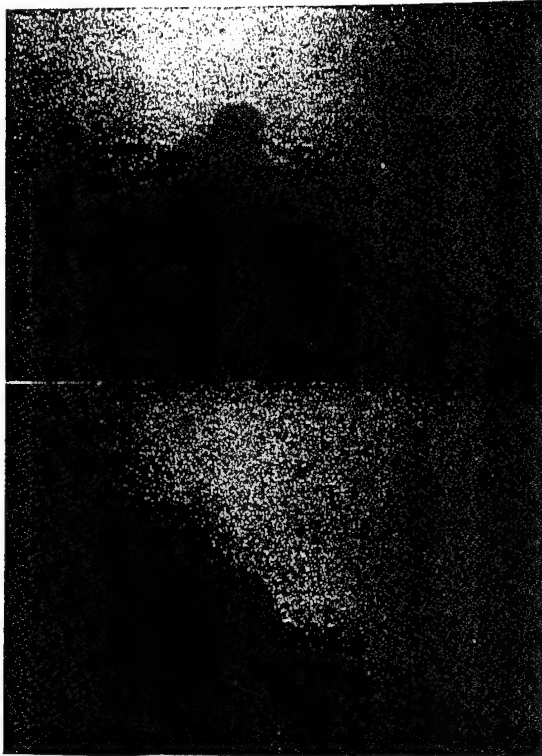


Fig. 1. Double pulsed Rayleigh image pair of a Mach 3 high Reynolds number boundary layer. The lower image was taken 20 $\mu$ s after the upper image and flow is from right to left. The images were taken with two separate cameras.

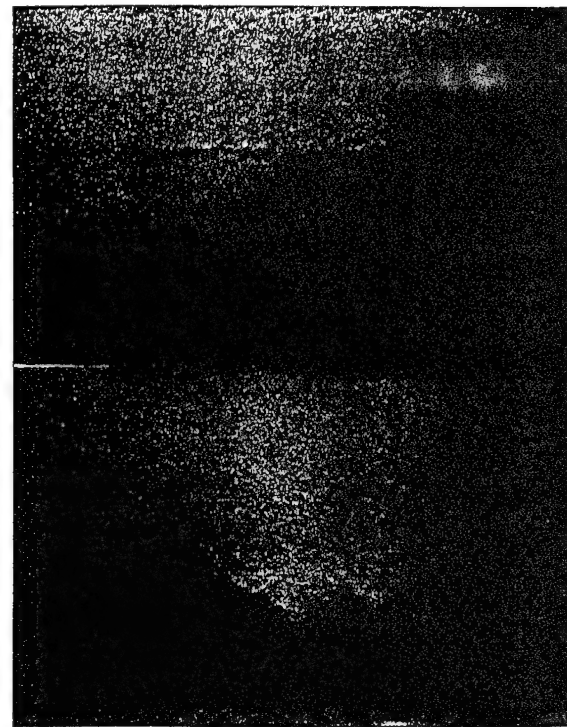


Fig. 2. Double pulsed Rayleigh image pair of a Mach 3 high Reynolds number boundary layer. The lower image was taken 60 $\mu$ s after the upper image and flow is from right to left. The images were taken with two separate cameras.

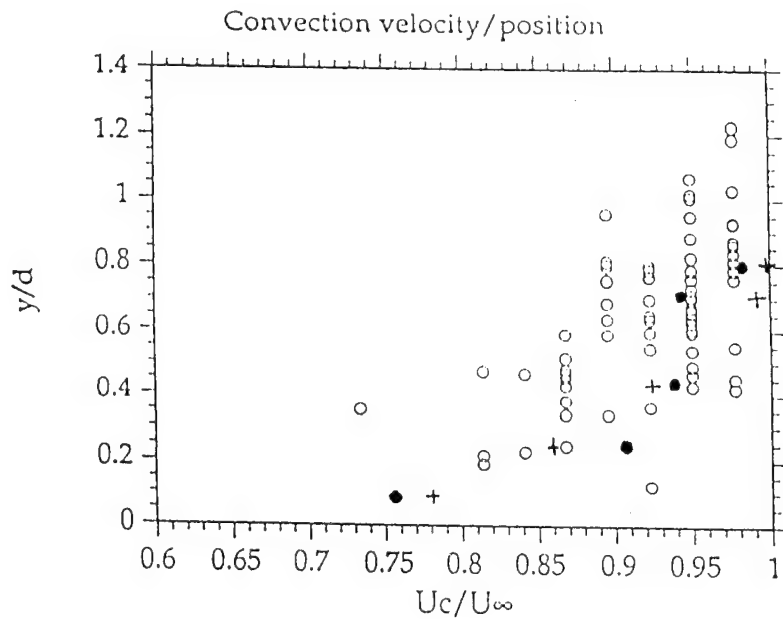


Fig. 3. Normalized convection velocities across the boundary layer determined by double pulsed Rayleigh imaging (open circles),<sup>4</sup> RELIEF flow tagging (solid circles) and pitot survey (crosses).<sup>3</sup>

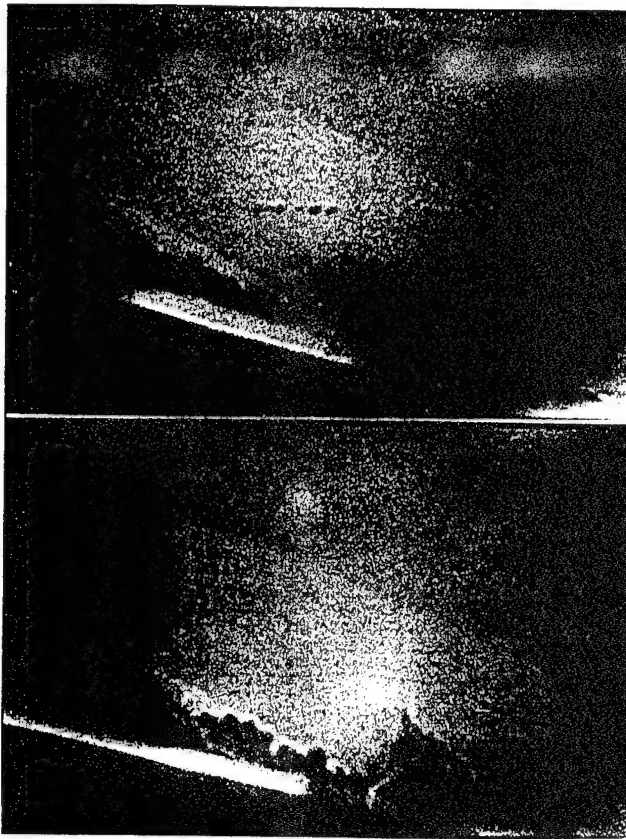


Fig. 4. Double pulsed Rayleigh image pair showing a shock wave / boundary layer interaction at a 16 degree wedge in a Mach 3, high Reynolds number flow. The lower image was taken 40 $\mu$ s after the upper image and the flow is from right to left. The images were taken with two separate cameras.

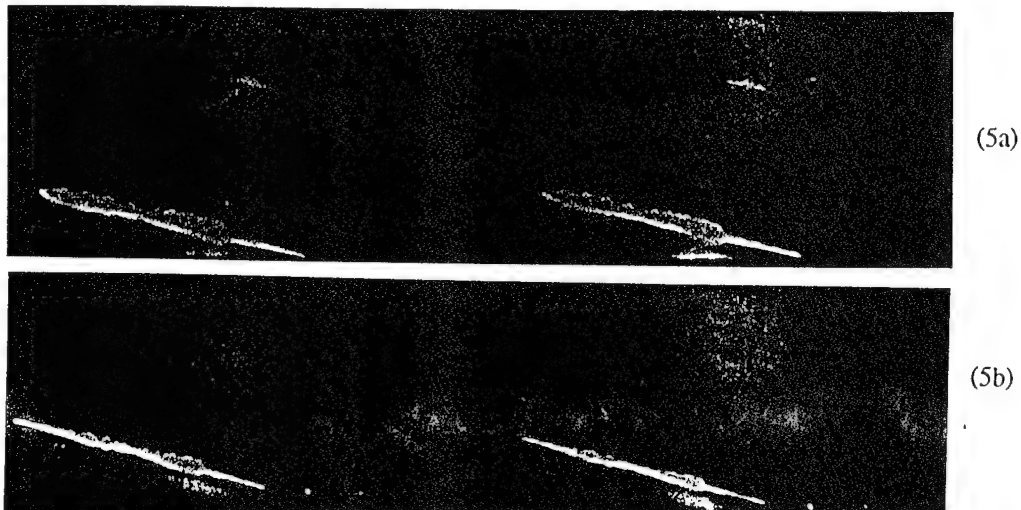


Fig. 5a,b. Double-pulsed Rayleigh image pairs of a shock wave/boundary layer interaction at a 16 degree wedge in a Mach 3, high Reynolds number flow. The left image of each pair is taken 40 $\mu$ s after the right image and flow is from right to left. The images were both taken with a single high-speed framing camera.

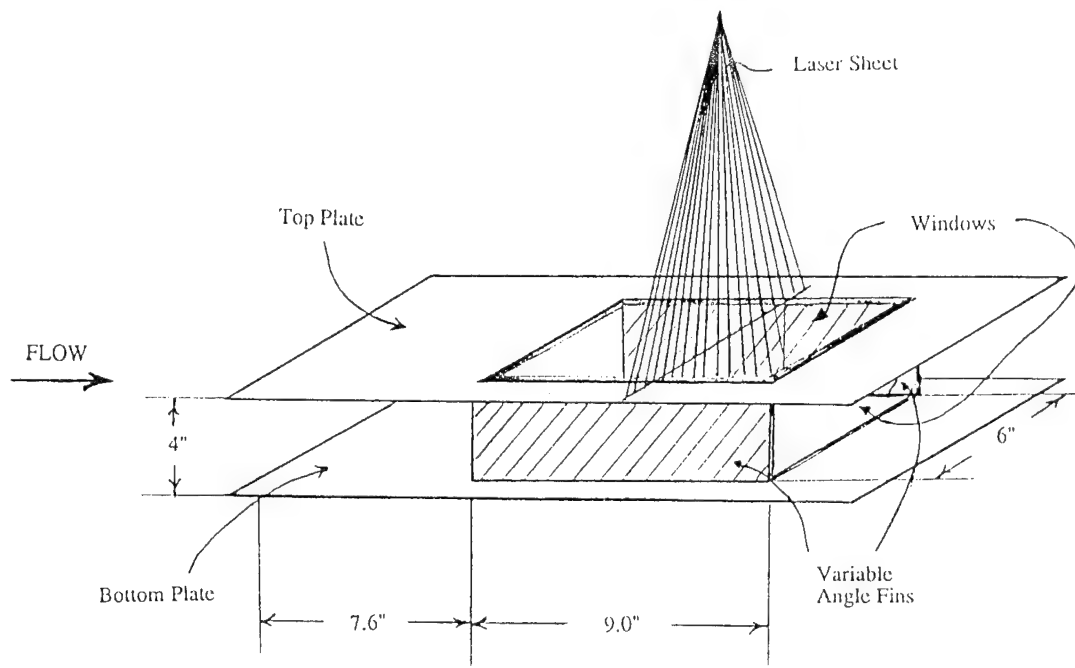


Fig. 6. Experimental geometry for Filtered Rayleigh imaging of the flow field inside of a supersonic inlet model.

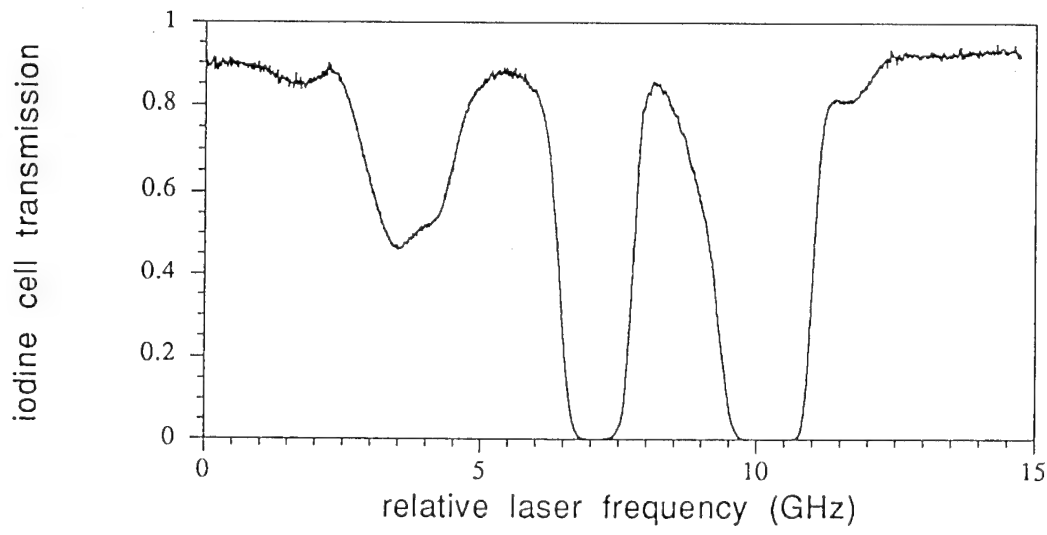


Fig. 7. Transmission spectrum of iodine vapor cell. The strong absorption line shown here near 10 GHz was used as the filter for the Filtered Rayleigh imaging experiments.

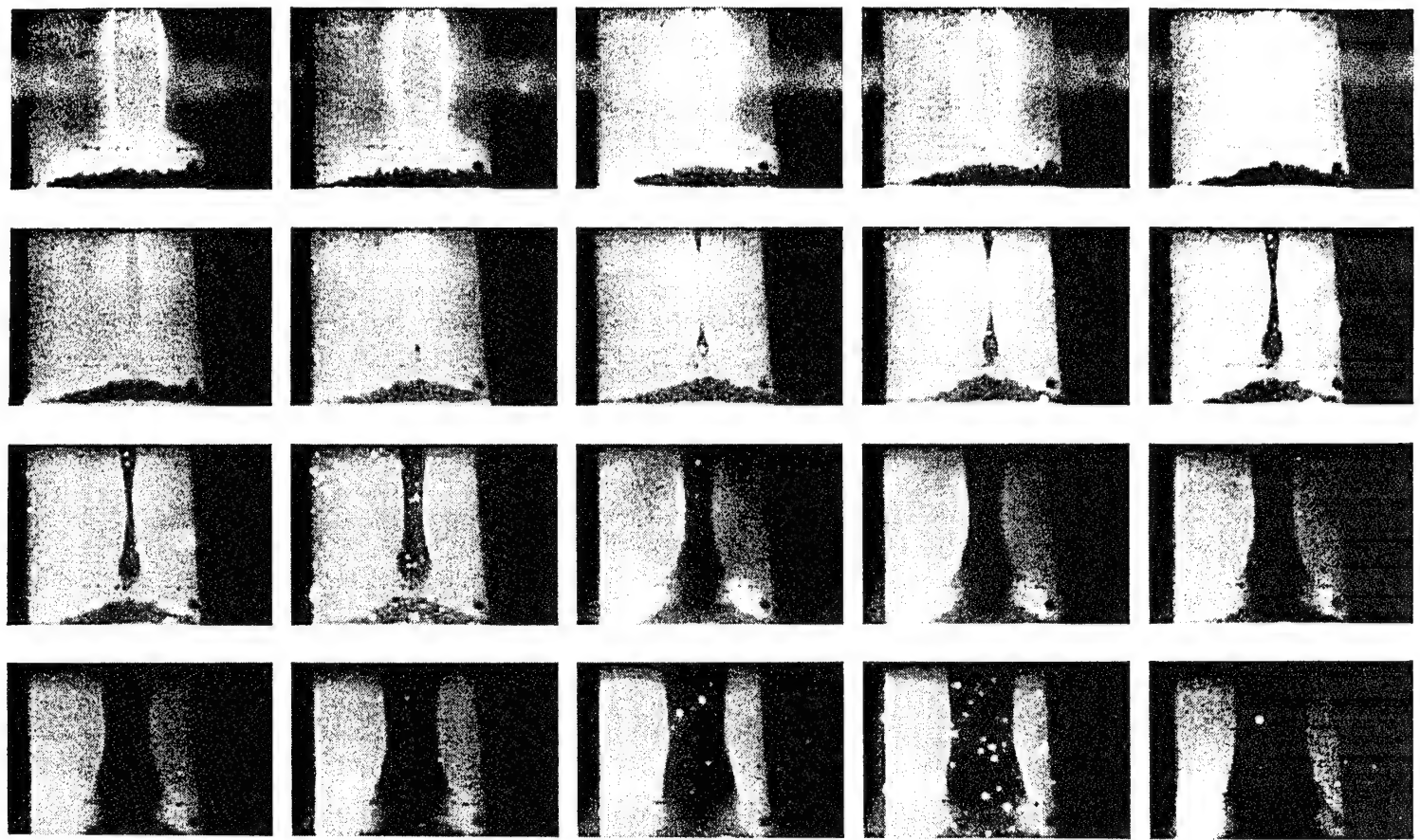


Fig. 8a-t. Cross sectional Filtered Rayleigh images taken at sequential 0.1 inch intervals moving downstream through the shock crossing region in the inlet model.

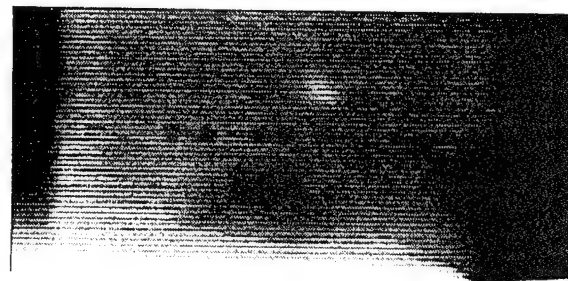


Fig. 9. Filtered Rayleigh image of molecular scattering taken approximately 3 inches downstream of the shock crossing point. The image shows the bottom 1.5 inches of the central portion of the flow.



AIAA-92-3894

**FILTERED RAYLEIGH SCATTERING MEASUREMENTS  
IN SUPERSONIC/HYPersonic FACILITIES**

RICHARD B. MILES, JOSEPH N. FORKEY, AND  
WALTER R. LEMPERT,

PRINCETON UNIVERSITY  
DEPARTMENT OF MECHANICAL & AEROSPACE ENGINEERING  
PRINCETON, NEW JERSEY 08544

**AIAA 17th  
Aerospace Ground Testing Conference  
July 6-8, 1992 / Nashville, TN**

FILTERED RAYLEIGH SCATTERING MEASUREMENTS  
IN SUPersonic/HYPersonic FACILITIES

Richard B. Miles\*, Joseph N. Forkey, and Walter R. Lempert\*\*

Princeton University  
Department of Mechanical & Aerospace Engineering  
Princeton, New Jersey 08544

ABSTRACT

We present preliminary measurements of flow field properties in Mach 3 and Mach 5 flows using Filtered Rayleigh Scattering. Filter properties have been characterized by high resolution spectroscopy in order to optimize the selection of laser frequency and filter operating conditions, as well as for the development of an accurate filter modeling program. With an optimized filter we have used the background suppression feature of this technique to image the boundary layer structure in a Mach 3 high Reynolds number facility and the shock structure in a Mach 5 overexpanded jet. This has been achieved using a visible laser source. By frequency scanning the laser, we have also made time-averaged velocity measurements in the Mach 3 and Mach 5 flows. Data acquisition at 10 torr and below indicates that this approach can be extrapolated for use in hypersonic flow facilities and is applicable as an in-flight optical air data device for hypersonic vehicles.

1. INTRODUCTION

Filtered Rayleigh Scattering (FRS) is a new, nonintrusive diagnostic technique which is capable of generating both qualitative and quantitative images of high-speed, unseeded flow fields.<sup>1,2</sup> This approach is particularly attractive since it can be done in the visible portion of the spectrum, as compared to previous Rayleigh imaging which has used ultraviolet sources.<sup>3</sup> Furthermore, with a well controlled laser, the density, velocity, and temperature at any point in the image can be measured. In this paper we explore applications of Filtered Rayleigh Scattering to measurements in the supersonic and hypersonic regimes. Data is presented showing boundary layer structure and flow velocity in a Mach 3, 8" x 8", high Reynolds number air facility, and the shock structure and flow velocity in an overexpanded Mach 5 free jet. Line images have been acquired at pressures below 10 torr, indicating that this approach is well suited to hypersonic facilities which typically operate at low static pressures.

While the specific details of an FRS experiment vary depending upon the particular application (i.e., background suppression, velocity measurement, temperature measurement), the basic concept is the same in all cases. When narrow linewidth laser light is directed into a wind tunnel, some of the light is scattered from the windows and walls of the tunnel, and some of the light is Rayleigh scattered from the molecules in the flow (or from particles in the flow, should any be present). When the scattered light is imaged on

a camera, that portion originating from the windows and walls often obscures the portion originating from the flow. This is particularly true in low density flows where the Rayleigh scattered component is exceptionally weak. It is, of course, the Rayleigh scattered light that contains the flow field information: The linewidth of this light is related to the static temperature, the frequency shift of this light relative to the illuminating laser is related to the velocity, and the total intensity of this light is proportional to the density.

In order to implement FRS, an absorption filter consisting of a cell filled with a molecular or atomic vapor is placed between the camera and the wind tunnel (see Fig. 1). To suppress the background scattering from windows and walls, the laser frequency is tuned to overlap the absorption line of the molecular atomic species. As a consequence, the unshifted background light associated with scattering from nonmoving surfaces is absorbed by the filter and only the Doppler shifted scattering from the flow passes through and is subsequently imaged (see Fig. 1c). In order to fully suppress this background scattering, the atomic or molecular absorption line must be "optically thick," i.e., the cell must be opaque at line center.

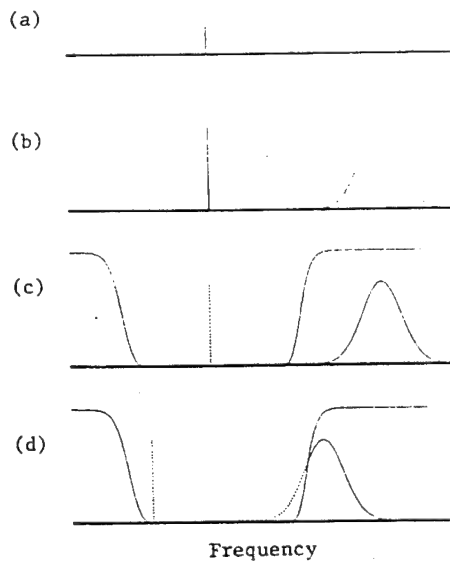


Fig. 1. Filtered Rayleigh Scattering Concept. (a) Narrow linewidth illumination laser. (b) Scattering from nonmoving surfaces (unshifted) and moving flow field (shifted and broadened). (c) Attenuation of scattering from nonmoving surfaces by the molecular filter for background suppression. (d) Laser frequency shift for velocity measurements.

\*Professor, Mechanical & Aerospace Engineering, Senior Member AIAA  
\*\*Research Scientist, Mechanical & Aerospace Engineering, Member AIAA

To obtain information about the flow velocity and temperature, the sharp transition from strong absorption to strong transmission is used. The laser is frequency tuned until the Doppler-shifted Rayleigh scattered light is partially absorbed by the filter (see Fig. 1d). The fraction of the Rayleigh-scattered signal that is absorbed for a given laser frequency is then a function of the Doppler shift (velocity) and the thermal linewidth (temperature). The magnitude of the signal is proportional to the density.

For the experiments presented here, we have used a frequency-doubled Nd:YAG laser which is tunable over approximately 60 GHz as a source, and an optically thick iodine molecular vapor cell as a filter. Accurate filter characterizations have been done using a continuous wave source which generated a few microwatts of stable frequency-doubled light with a very narrow linewidth. Wind tunnel measurements used an injection-locked pulsed laser source which produced 330 mJ pulses of approximately 7 nsec duration. This paper begins by reporting the results of the filter characterization and filter modelling efforts. The Mach 3 and Mach 5 measurements are then presented and we conclude with discussions on the extrapolation of this technique into the hypersonic regime and flight applications.

## 2. FILTER CHARACTERIZATION BY EXPERIMENTATION MODELLING

In order to accurately characterize the iodine filter, we made a number of spectroscopic measurements and developed a preliminary model of the absorption profile on a SUN 4 workstation. The motivation for these pursuits is two-fold. First, an accurate characterization of the absorption filter profile is necessary to analyze experiments aimed at obtaining quantitative data such as velocity, temperature, and density. Second, an understanding of the mechanisms responsible for the shaping of the absorption filter, and the ability to model a filter before actually building it, aid in designing filters which will maximize the accuracy of future measurements. The characterization experiments consisted of measuring cell transmission as a function of laser frequency and measuring peak absorption values of individual spectroscopic lines.

The absorption cell used in the characterization experiments was a 10" long, 2" diameter glass cell which was wrapped in heating tape and insulated with fiberglass tape to maintain the cell temperature to within  $\pm 5^{\circ}\text{C}$ . All experiments were run with a cell temperature of  $80^{\circ}\text{C}$ . Attached to the glass cell is a water-cooled side arm which contains crystalline iodine. All foreign gases are pumped out of the cell so that the pressure in the cell is determined by the vapor pressure of the crystalline iodine in the side arm. Since the vapor pressure of iodine is a strong function of temperature, the side arm temperature must be precisely controlled. This is accomplished by circulating water through a water jacket which surrounds the side arm. In this way, the side arm temperature can be set to any temperature below the cell temperature ( $80^{\circ}\text{C}$ ) with an accuracy of better than  $\pm 1^{\circ}\text{C}$ . During the experiments, the side arm temperature was varied in  $5^{\circ}$  increments from  $30^{\circ}\text{C}$  to  $55^{\circ}\text{C}$ . These temperatures correspond to vapor pressures ranging from 0.47 torr to 3.05 torr.<sup>4</sup>

The experimental set-up for both the transmission spectroscopy and the peak absorption

experiments is shown in Fig. 2. A Lightwave Nd:YAG diode-pumped, solid-state, nonplanar ring laser provided about 200 mW of narrow linewidth (5 kHz), continuous wave, frequency-tunable laser radiation at a wavelength of 1064 nm. A KTP crystal frequency doubled a small amount of this radiation to a wavelength of 532 nm, which was separated from the fundamental wavelength by a Pellin-Brocca prism. Residual radiation at 1064 nm was sent to a confocal etalon which monitored the laser frequency. A beamsplitter then split the green light into two beams. One beam was used to monitor laser intensity (which varied substantially over the full tuning range of the laser), while the second beam was passed through the iodine cell for transmission measurements. Signals were collected by two photomultiplier tubes, each mounted on a spectrometer which filtered out room light. The effects of reflections and absorption by cell windows were accounted for by normalizing each data scan to a reference scan of an evacuated cell containing no iodine to establish a signal corresponding to 100% transmission. When measuring the peak absorption of a particular spectral line, the data scan was started with the laser tuned outside of the absorption line and with a number of neutral density filters in front of the photomultiplier tube monitoring the signal transmitted through the cell. As the frequency of the green laser beam approached the spectral line center and the signal transmitted through the cell decreased, neutral density filters were successively removed from the beam path, effectively amplifying the signal which reached the detector. In this way, we were able to measure transmissions over a range of nearly seven orders-of-magnitude (from transmissions of 1 to nearly  $10^{-7}$ ) without having to change the bias voltage on the photomultiplier tube.

A plot showing cell transmission versus laser frequency is shown in Fig. 3. This data was taken with a side arm temperature of  $35^{\circ}\text{C}$ , which corresponds to a vapor pressure of 0.70 torr. This data represents the iodine absorption over the entire tuning range of the frequency-doubled Nd:YAG laser. When the spectroscopic features in this data set are matched to those in the Iodine Atlas, the wavelength tuning range of the frequency-doubled Nd:YAG tuning range is found to be approximately  $2 \text{ cm}^{-1}$  from  $18787 \text{ cm}^{-1}$  to  $18789 \text{ cm}^{-1}$ .<sup>5,6</sup>

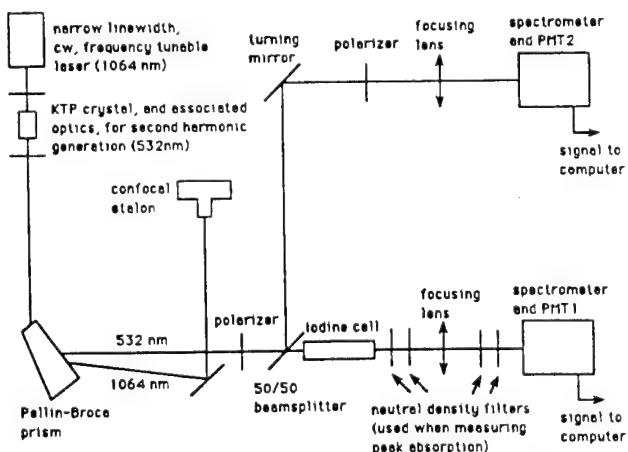


Fig. 2. Experimental set-up for iodine filter spectroscopy and absorption measurements.

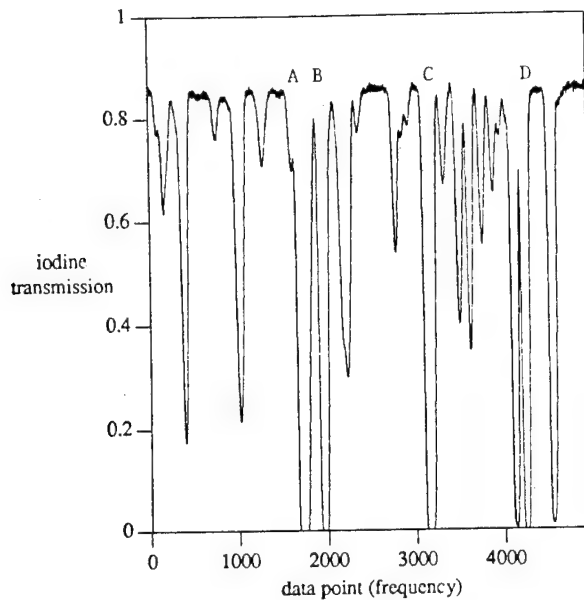


Fig. 3. Transmission spectrum of optically thick iodine (cell temperature of 80°C, side arm temperature of 35°C) over the scanning range of the frequency-doubled Nd:YAG laser. The optically thick spectral features, A,B,C, and D, are indicated.

Within this  $2 \text{ cm}^{-1}$  (60 GHz) tuning range, there are 4 absorption lines (labelled A,B,C, and D in Fig. 3) which are strong enough to use for FRS. Lines A and C are of particular interest since they both have absorption cut-off edges that are isolated from neighboring lines, thus allowing for relatively simple data analysis of FRS experiments. In order to better quantify the profiles associated with these two absorption bands, higher resolution scans were taken close to the bands for a range of side arm temperatures. Results from these scans are shown in Figs. 4 and 5. We estimate the error here on transmission measurements to be about  $\pm 2\%$ , and the error on relative frequency measurements to be about  $\pm 17\%$ . The large error on the frequency axis is due to the fact that the confocal etalon used to monitor frequency was not thermally stabilized, and, therefore, thermal expansions of aluminum mounts and spacers caused rather large shifts in etalon transmission peaks. Experiments using a more stable etalon are planned for the future.

Three features which are of great significance in using an iodine filter for FRS experiments are apparent in Figs. 4 and 5. The first is that the steepest edge of line A is not truly isolated. Indeed, a "shoulder" exists on this edge due to a much weaker, slightly shifted absorption line. This extra absorption must be taken into account when analyzing data from an FRS experiment that uses this line. In the determination of velocity in the nitrogen experiment described below, neglecting the effects of this shoulder accounted for an extra 4% error. The second feature is that, as the side arm temperature is increased, thereby increasing peak optical depth, the absorption profiles become wider, as expected. However, there is a steadily increasing continuum absorption, which we believe

is caused by a transition from the ground state of iodine to a dissociative electronic state.<sup>7</sup> The presence of this transition leads to a trade-off between background suppression and continuum absorption. Finally, we observe that the steepest cut-off edges on lines A and C require approximately 0.6 GHz to shift from maximum transmission to less than 1% transmission and that the slope is linear over a large portion of this range. Thus, while still suppressing background, the transmission of the filter will depend directly on the velocity of the flow over a range determined by the collection geometry.

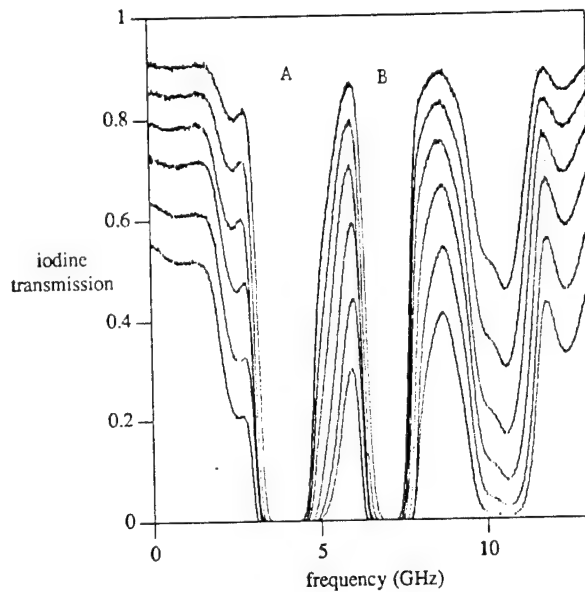


Fig. 4. High resolution spectral scan of spectral features A and B for iodine cell side arm temperatures ranging in 5°C steps from 30°C to 55°C.

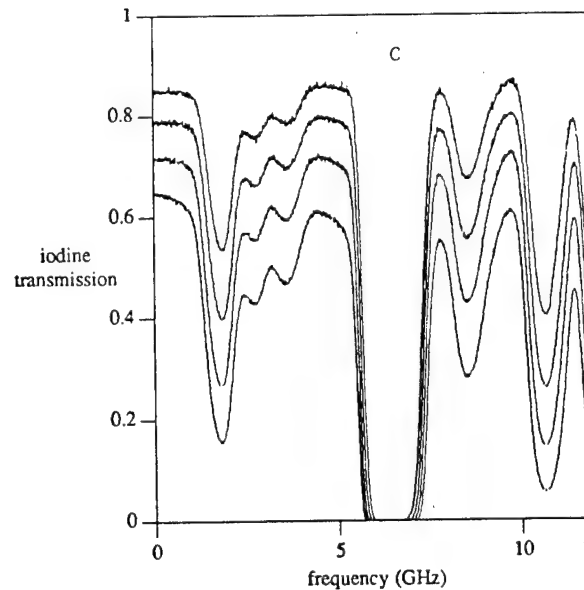


Fig. 5. High resolution spectral scan of absorption feature C for iodine cell side arm temperatures ranging from 35°C to 50°C in 5° steps.

An example of the data obtained while making measurements through the maximum absorption regions of lines A, B, C, and D is shown in Fig. 6. This scan is taken over lines A and B. Each jump in the data set occurs when a neutral density filter of roughly 10% transmittance is removed from the signal beam path, effectively magnifying the vertical scale by roughly 10. The minimum transmissions of the lines A and B shown in Fig. 6 are found to be  $3.7 \times 10^{-6} \pm 20\%$  and  $9.2 \times 10^{-4} \pm 10\%$ , respectively. The error on the measurement for line B is smaller than that for line A since fewer neutral density filters were necessary for the measurement on line B. Using this technique, we have measured minimum transmission values for lines A, B, C, and D for side arm temperatures between  $30^\circ\text{C}$  and  $50^\circ\text{C}$  (corresponding to vapor pressures from 0.47 torr to 2.15 torr). For the two lines, A and C, which are most suitable for FRS, we found minimum transmissions of  $3.7 \times 10^{-6}$  and  $8.6 \times 10^{-4}$ , respectively, at a side arm temperature of  $30^\circ\text{C}$ , and minimum transmissions of less than  $1.0 \times 10^{-7}$  (the limit of our measurement range) for line A at side arm temperatures greater than or equal to  $40^\circ\text{C}$ , and, for line C at side arm temperatures greater than or equal to  $45^\circ\text{C}$ . These very strong line center extinctions suggest that FRS may be used to eliminate narrow linewidth particulate scattering which overlaps a broader molecular Rayleigh scattering signal. This application is similar to that used by C.Y. She and co-workers in their High Spectral Resolution LIDAR.<sup>8</sup>

The minimum transmission measurements described above were repeated using our Continuum high-power, Q-switched, injection-seeded, frequency-doubled Nd:YAG pulsed laser. Such an experiment was necessary since the absorption profile of the cell depends not only on the properties of iodine, but also on the characteristics of the illuminating light. Although the results from this experiment are still preliminary, they show a large discrepancy between minimum absorption measurements made using the cw light source and those made with the pulsed light source. Differences in minimum transmission values for line A as large as three orders-of-magnitude have been measured. This difference cannot be accounted for simply by the difference in linewidth of the sources. In order to be certain that the cause of this difference was due to the change in light source and not due to some change in the absorption cell characteristics, the cw and pulsed light sources were set-up next to each other and alternately used to measure minimum transmission. Measurements of the minimum transmission of line A with a cell temperature of  $80^\circ\text{C}$  and a side arm temperature of  $30^\circ\text{C}$  using the cw light source, were made both before and after a measurement was made with the pulsed laser source. While the results of the two cw measurements agreed to within the experimental error, the pulsed measurement differed from the cw measurement by a factor of nearly 1000. The cause of this discrepancy has not yet been thoroughly investigated. One explanation may be that, although the pulsed laser is injection-locked to a single mode, other modes are still present at a very low amplitude. If one part in 1000 of the energy contained in each light pulse (i.e., 0.3 mJ out of 300 mJ per pulse) is not locked, this could account for the observed measurements.

The absorption profiles obtained from the above described experiments are currently being

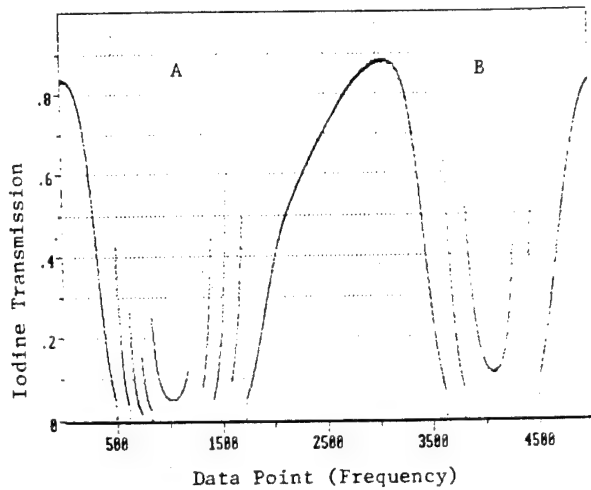


Fig. 6. High resolution peak absorption measurement of spectral features A and B using four neutral density filters for line A and two neutral density filters for line B.

used to estimate expected accuracies for measurements that will be made in future FRS experiments. In addition, the results of these experiments have been used to test the accuracy of a theoretical model which we are currently developing. Throughout the spectral region of interest, the only two relevant transition manifolds are from the bound electronic ground state (X) to the bound excited state (B), and from the ground state to a dissociative state.<sup>7</sup> The second of these accounts for the continuous background absorption observed in the experimental data. The second transition manifold has not yet been incorporated into the model, so the predicted profiles that follow do not contain the continuous background absorption seen in the experiments.

Due to the extensive spectroscopic data available in the literature on the X-B manifold, we were able to incorporate in the model all transitions with a lower vibrational quantum number,  $v''$ , between 0 and 2, an upper vibrational quantum number,  $v'$  between 1 and 62, and with lower rotational quantum number,  $J''$  between 0 and 150.<sup>6,9</sup> Using spectroscopic constants found in References 6 and 9, the model first determines the frequency of each rotational transition. Each of these absorption lines is split due to both the coupling between the nuclear electric quadrupole moment and the internal molecular electronic field gradients (NEQ hyperfine splitting), and the coupling between the nuclear magnetic moment and the magnetic field caused by the rotation of the molecule (magnetic hyperfine splitting).<sup>10,11</sup> This hyperfine splitting divides each rotational transition into either 15 or 21 lines, depending on whether the value of  $J''$  associated with the line is odd or even. The splitting of lines with odd  $J''$  is different from that of lines with even  $J''$  due to the necessity of an anti-symmetric molecular wavefunction and the resulting constraints placed on possible nuclear spin values.<sup>10</sup> Since the hyperfine splitting due to the magnetic interaction is smaller than that due to the nuclear electric quadrupole interaction, we have ignored it as a first approximation and included only the NEQ splitting. Therefore, the model splits each rotational line into six hyperfine lines, each of which has a degeneracy determined by whether  $J''$  is

odd or even. The absorption coefficient for each of these lines is then calculated, assuming thermal broadening only.

The average electronic transition strength, from Ref. 7, was corrected by 3% to give an optimum fit to the measured transmission profiles. The Franck-Condon factors were taken from Reference 12.

Using these formulas, the model produces profiles that appear very similar to those obtained by experimentation (see, for example, Figs. 7 and 8). Although some of the weaker lines observed in the experimental data are not present in the model data, all of the strong, optically thick lines (which are of interest for FRS) are present. As shown in Fig. 8, the shape of the optically thick line C is predicted well by the model.

Quantitative comparison of the peak optical depths for lines A, B, C, and D under various cell conditions shows an agreement of within  $\pm 5\%$  between values predicted by the model and those measured in the experiments. This corresponds to minimum transmissions values that agree to better than  $\pm 60\%$ .

### 3. VELOCITY MEASUREMENTS AND BACKGROUND SUPPRESSION

#### a. Measurements in a Mach 3, 8" x 8" High Reynolds Number Facility

As a demonstration of the utility of the FRS technique, we have taken instantaneous planar images and made time-averaged velocity measurements in the large 8" x 8", Mach 2.9 wind tunnel located at the Princeton University Gas Dynamics Laboratory. In this case, the Rayleigh scattering from the flow is from a fog of condensed water vapor. The relatively heavy mass of these very small crystals results in a very narrow scattering linewidth due to the fact that thermal motion varies with the inverse of the square root of the particle mass. (If the particles are heavy enough, the Rayleigh signal from the flow will have the same linewidth as does the laser pulse. This is found, indeed, to be approximately the case as evidenced by the similar cut-off rates of the background and Rayleigh signals as the laser is tuned.) The absorption filter used in the experiments consisted of a 10" long, 2" diameter glass cell wrapped in heating tape and maintained at a temperature of  $80^{\circ}\text{C} \pm 5^{\circ}\text{C}$ . Iodine crystals were located in a side arm which was maintained at a temperature of  $30^{\circ}\text{C} \pm 1^{\circ}\text{C}$ . This side arm temperature corresponds to a cell pressure (determined by the iodine vapor pressure) of 0.47 torr. The Doppler shift was determined by measuring the change in laser frequency required to move from the 50% transmission point of scattered light from the windows and walls to the 50% transmission point of the Rayleigh signal from the flow. Since there is negligible linebroadening from the condensate fog, the 50% points are easily matched for each curve. Figure 9 shows the scans of the scattering intensity at these two points on the image as the laser is tuned in frequency. Figure 10 shows three images from the approximately 500 images taken as the laser is tuned. The frequency at which each image was taken is indicated on Fig. 9. The free stream velocity measured by this scan is  $524 \text{ m/s} \pm 7\%$ . This value agrees to within the experimental error with the expected velocity of  $561 \pm 3\%$  measured using the more accurate RELIEF technique and taking into account the uncertainty in stagnation temperature.<sup>13</sup>

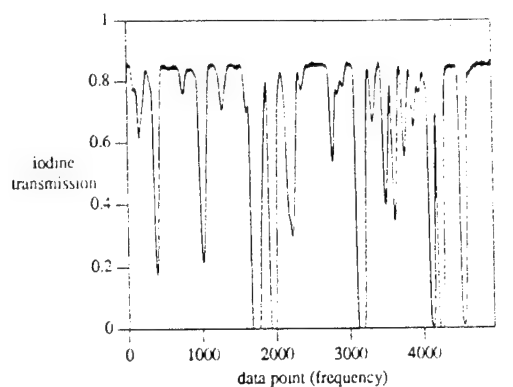


Fig. 7. Comparison of the measured iodine transmission (top) and the transmission computed from the model (bottom) over the full scanning range of the laser for a cell temperature of  $80^{\circ}\text{C}$  and a side arm temperature of  $35^{\circ}\text{C}$ .

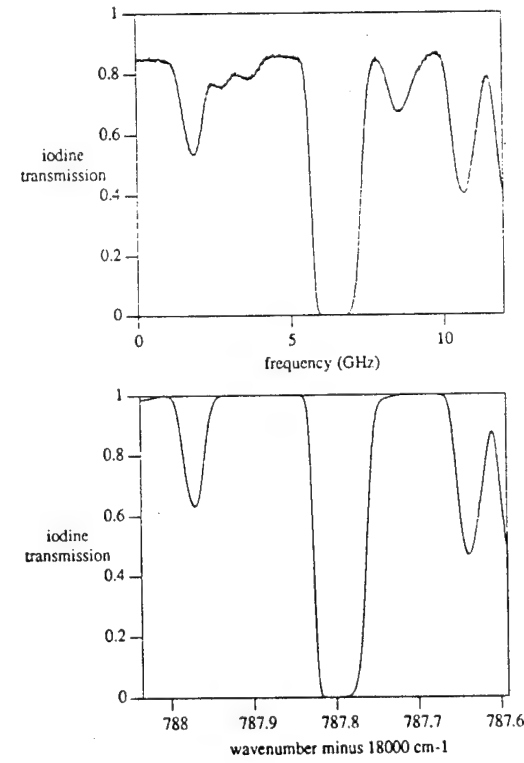


Fig. 8. High resolution comparison of the measured transmission (top) across spectral line C with the transmission computed from the model (bottom) for a cell temperature of  $80^{\circ}\text{C}$  and a side arm temperature of  $35^{\circ}\text{C}$ .

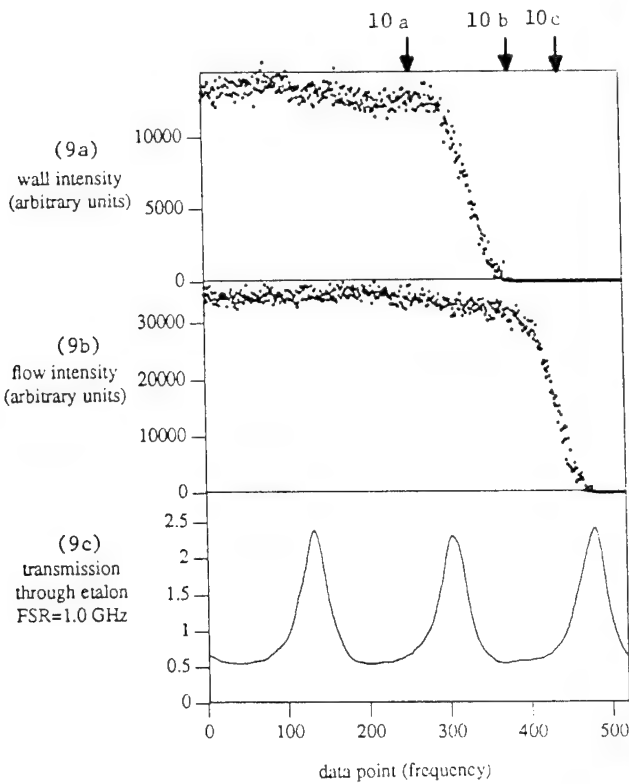
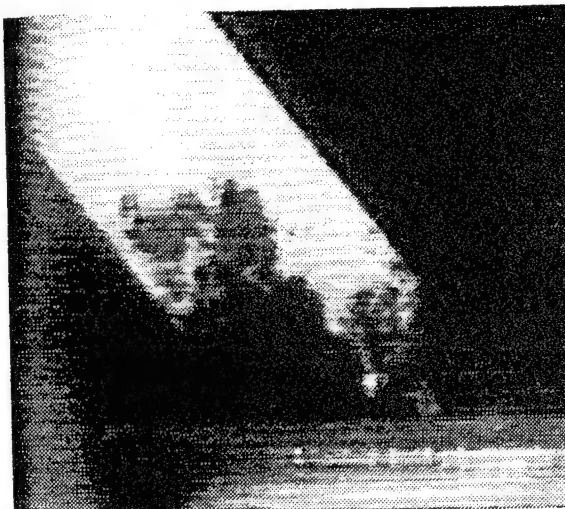


Fig. 9. Velocity measurement of the Mach 3 flow. (a) Unshifted scattering from the windows and walls imaged through the filter as a function of laser frequency. (b) Frequency-shifted scattering from the core of the flow imaged through the filter as a function of laser frequency. (c) Fabry-Perot interferometer calibration of the laser frequency. A comparison of the 50% cut-off of Fig. 9a with Fig. 9b gives a measure of  $524 \pm 36$  m/sec.



10(a)



10(b)



10(c)

Although the experimental error associated with this measurement is much smaller than that reported previously for the measurement made in the small 1.3 cm x 2.6 cm tunnel,<sup>1</sup> we expect that it will be reduced further in future experiments. Of the 7% error reported, almost 5% is due to shot noise and laser intensity fluctuations. The shot noise is much smaller than that present in the previous small tunnel measurement due to increased pulse energy provided by a new laser. However, this velocity measurement is based on a simple hand analysis of data which does not include any curve fitting or temporal averaging of signal levels. Either of these procedures would reduce the error attributed to shot noise. The two other major sources of error (each responsible for about 1% error) were uncertainty in the angle between the flow direction and the laser sheet, and uncertainty in the frequency tuning rate of the laser. The first of these error sources is easily dealt with. Reducing the second source of error will require accurate laser frequency calibration which may best be achieved by heterodyning a portion of the seed laser beam with a frequency-stabilized reference laser.

Fig. 10. Filtered Rayleigh images of a Mach 3 high Reynolds number boundary layer at different instances during the laser frequency scan. The points at which these figures were taken are indicated in Fig. 9: (a) Outside of resonance. (b) Background suppressed. (c) Near the cut-off point for the flow field.

b. Measurements in a Mach 5 Overexpanded Free Jet

A small Mach 5 jet was constructed which has a circular nozzle with an exit diameter of 5mm and a throat diameter of 1mm. The jet was operated with either air or nitrogen at plenum pressures ranging from 100 to 800 psia. The pressure in the test section was held constant by two 15 SCFM vacuum pumps working in parallel (see Fig. 11). Figure 12 shows instantaneous and time-averaged UV Rayleigh images of this jet taken with a frequency quadrupled Nd:YAG laser at 266 nm. For these images, the plenum pressure was held at approximately 200 psia, which was low enough to avoid condensation. FRS experiments were also performed with this apparatus. Scattered laser light was imaged onto a double-intensified CID camera using a Vivitar zoom lens. For these experiments, a 3" long, 2" diameter iodine absorption filter was used with a filter temperature of 80°C and a side arm temperature ranging from 41°C to 44°C. Initial measurements were made by focusing the frequency-doubled laser into a sheet and scanning the laser frequency in a manner similar to that done for the Mach 3 measurement. In all cases the laser beam was incident on the jet at an angle of 40° with respect to the flow direction, and the camera lens axis was perpendicular to the plane defined by the flow and the laser beam. Laser energies at 532 nm of approximately 330 mJ/pulse, and pulse lengths of approximately 7 nsec were typical laser operating conditions. Assuming the pulse is Fourier transform limited and Gaussian in time, the frequency linewidth of this laser is 60 MHz.

The utility of FRS to suppress background noise in this configuration is clearly shown for a nitrogen jet in Figs. 13a and 13b. In Fig. 13a, the laser is tuned away from the iodine absorption band, so both background scattering and scattering from the flow is imaged as would occur without the filter in front of the camera. In Fig. 13b, the laser is tuned so that it overlaps the iodine absorption band. The background scattering is absorbed by the filter, but scattering from the flow is Doppler-shifted outside of the absorption band and is imaged by the camera. Although no condensed water vapor is present in this flow, good contrast is achieved when structures in the flow are imaged using FRS.

In addition to suppressing background scattering, FRS was used in this configuration to measure the time-averaged velocity of the nitrogen flow in a manner similar to that done for the Mach 3 flow. This measurement is somewhat more complex than for the Mach 3 case, since, here, the scattering is from nitrogen molecules so the linewidth of the scattered light is significantly greater than that of the laser. The molecular scattering signal level is lower than in the Mach 3 case due to lower static density and the absence of the condensate fog. In order to increase the detected signal level, the laser beam was focused to a line which was imaged with the camera system. The variation of the brightness of the appropriate point in the line as compared to the light scattered from the window was then used for the measurement (see Fig. 14) leading to a value of 681 m/sec with an uncertainty of 41%. This is in good agreement with the value of 690 m/sec expected in this flow. The slope of the cut-off is significantly shallower than was the case in Fig. 9 since the thermal broadening of the nitrogen molecules is significant compared to that of the

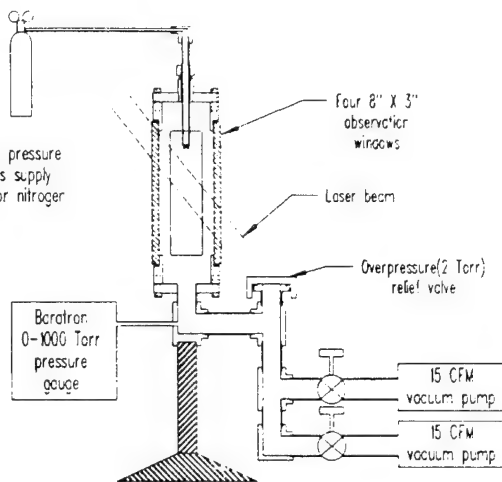
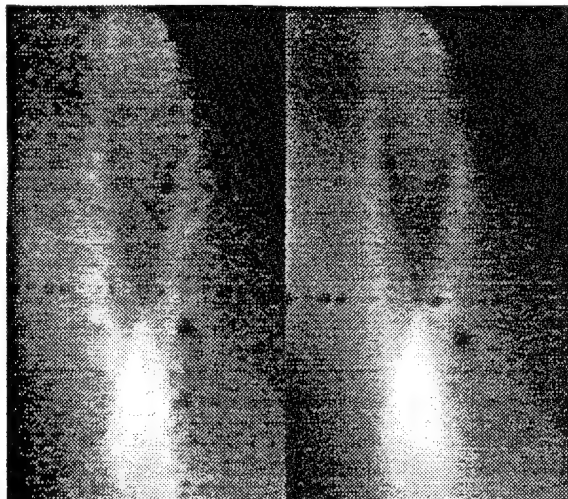


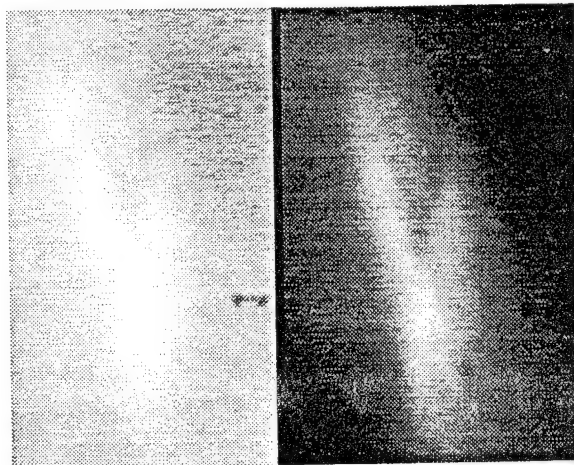
Fig. 11. Experimental set-up for the Mach 5 overexpanded jet experiments..



12(a)

12(b)

Fig. 12. Ultraviolet (266 nm) images of the Mach 5 jet. (a) Instantaneous image. (b) Time-averaged image.



13(a)

13(b)

Fig. 13. Time-averaged, Filtered Rayleigh Scattering images (visible-532 nm) of the Mach 5 overexpanded jet. (a) Without background suppression. (b) With background suppression.

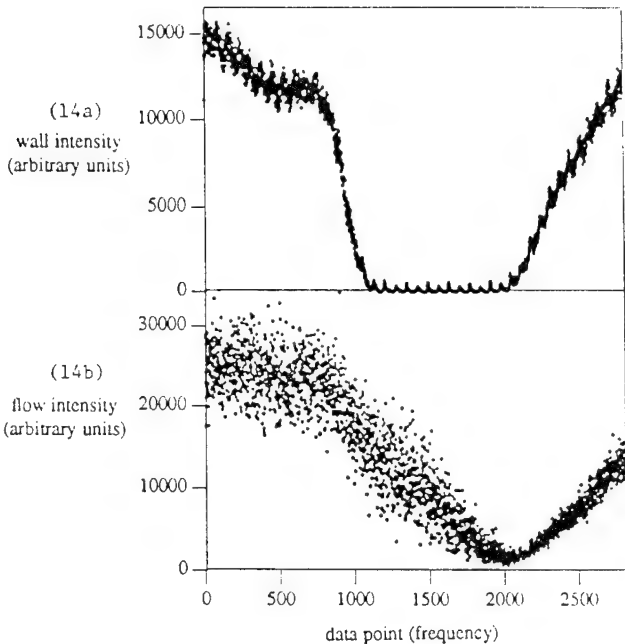


Fig. 14. Laser scan for velocity measurement in the Mach 5 jet. (a) Background signal imaged through the filter versus laser frequency. (b) Signal from the core of the flow imaged through the filter versus laser frequency. The point scatter reflects flow fluctuations as well as shot noise and laser jitter. A comparison of Figs. 14a and 14b yields a velocity of  $681 \pm 270$  m/sec.

condensate fog. This slope can be used to measure the static temperature of the flow, but it contributes significantly to the uncertainty of the velocity measurement. We expect a dramatic reduction in the velocity uncertainty and the added capability of determining temperature when the data is computer fit to the precise filter profile.

#### 4. EXTENSION INTO A HYPERSONIC REGIME

The Filtered Rayleigh Scattering approach is particularly attractive for measurements in hypersonic flows. The low densities characteristic of these flows simplifies the line broadening mechanisms, and the high speeds lead to large frequency shifts so strong background suppression can be achieved. In order to examine the applicability of FRS in that regime, we have made preliminary measurements at low pressure in our small Mach 5 facility. In order to maximize the scattered signal, the laser was focused to a line and passed through the Mach 5 jet as previously discussed. In this case, however, the plenum pressure was reduced to achieve very low static pressures in the test section. Figure 15 shows the image of this line at 10 torr, taken with and without background suppression. In this case, background suppression is critical since the signal level from the flow field itself is small. The line is clearly visible in these images, and quantitative density measurements and velocity measurements at any point along the line can be

made. We have further reduced the pressure to approximately 5 torr and, again, have seen good signal-to-noise. It is important to note that laser fluences in excess of normal breakdown levels are possible at these low densities, allowing us to significantly increase the scattering from a single resolvable element in the flow. Simple augmentations to this experiment include double-passing the line through the flow regime to allow instantaneous acquisition of orthogonal velocity components, and multiple passing of the line through the region of interest to permit images to be acquired. By carefully choosing the geometry, the velocities of very high Mach number flows can be measured while still preserving the background suppression feature. This approach is also of interest for measuring mass flux and may be applied with a multiple imaging system as a mass flux measurement to monitor the flow field at the inlet to a supersonic combustor.<sup>14</sup>

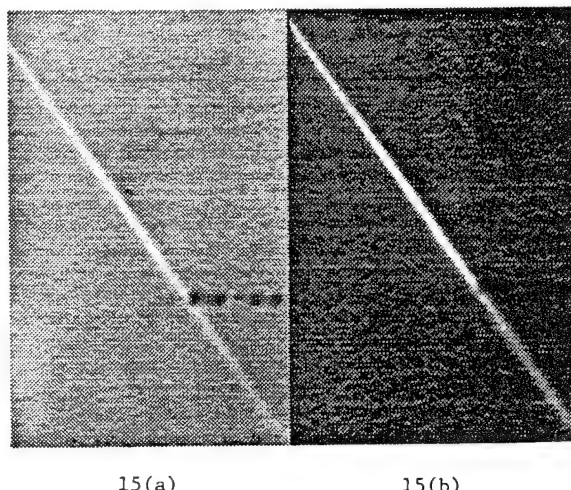


Fig. 15. Filtered Rayleigh Scattering image of a line through the Mach 5 jet at 10 torr. (a) Without filter. (b) With background suppression.

#### 5. MODELING OF TEMPERATURE AND PRESSURE MEASUREMENTS FOR AN IN-FLIGHT AIR DATA SYSTEM

One of the applications for which FRS is being considered is as an Optical Air Data System (OADS) for the National Aerospace Plane (NASP).<sup>15</sup> The parameters which must be measured by such a system are air speed, angle-of-attack, slip angle, and ambient air pressure and temperature. Results of a simple analysis using an ideal filter profile show that the iodine filter is well suited to measuring velocity, density, and temperature under the conditions that NASP is expected to encounter. Further work which incorporates the experimentally measured absorption profiles with theoretically predicted Rayleigh scattering intensity profiles has been performed in order to determine the accuracies which may be expected. Results of transmission versus temperature modeling also suggest that pressure may be directly measured spectoscopically in low density environments.

In order to use Filtered Rayleigh Scattering in the OADS, a laser pulse is fired out of the front of the plane. Light from this pulse is Rayleigh scattered back through an iodine cell to detectors located in the plane. Scattering from optical elements and from hot molecules behind the shock wave is eliminated by using time-gating.

In order to determine which iodine absorption line to use and under what cell conditions, plots of transmission versus temperature were calculated using the experimentally determined absorption profiles discussed in Section 2 and shown in Figs. 4 and 5. These transmission vs. temperature plots are shown in Fig. 16. Solid lines are plots generated using absorption line C, and dotted lines are plots generated using absorption line A. Side arm temperatures are shown in parentheses. Figure 16 shows that the greatest sensitivity to temperature is achieved by using absorption line C at a side arm temperature of 35°C. The sensitivity predicted for this configuration ranges from 6 degrees Kelvin per percent change in transmission at 105 K to 16 degrees Kelvin per percent change in transmission at 295 K.

Note that for absorption line A with a side arm temperature of 55°C, the transmission is roughly a linear function of temperature with a transmission axis intercept of 0 transmission at a temperature of 0°K. Since the signal is also directly proportional to density, the measured signal will be the product of the density times the temperature which is just the ideal gas relation for pressure. Thus, in this particular case, the detected signal is a direct measure of the static pressure.

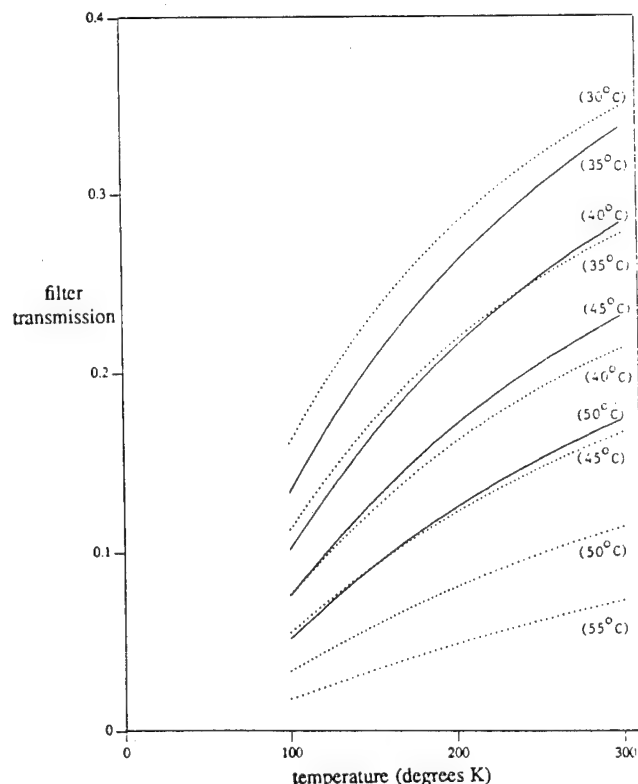


Fig. 16. Filter transmission versus temperature for lines A (dotted) and C (solid) for side arm temperatures used in Figs. 4 and 5.

## SUMMARY

We have explored the application of Filtered Rayleigh Scattering for quantitative measurements and imaging in supersonic and hypersonic flows. Specifically, we have used a narrow linewidth, frequency-doubled Nd:YAG laser together with an iodine molecular filter for background suppression and velocity measurements at Mach 3 and Mach 5. Both experimental and theoretical iodine filter transmission profiles were generated in order to permit us to optimize the filter characteristics and select the appropriate laser frequency range. The high-speed experiments yielded instantaneous images of boundary layer structure in the Mach 3 flow and overexpanded jet shock structure in the Mach 5 flow. Time-averaged velocity measurements were made in both cases by frequency scanning the laser and observing the attenuation of the scattered light through the iodine molecular filter. The technique has been extended to pressures below 10 torr in an effort to establish its utility as a measurement device for hypersonic facilities, and as an optical air data system for hypersonic aircraft.

## ACKNOWLEDGEMENTS

This work was supported by grants from NASA/Langley, AFOSR, an SBIR Grant through M.L. Energia, Inc. from the U.S. Army Missile Command, and a Graduate Student Researchers Program Grant from NASA/Lewis.

## REFERENCES

1. R.B. Miles, W.R. Lempert, and J. Forkey, "Instantaneous Velocity Fields and Background Suppression by Filtered Rayleigh Scattering," Paper #AIAA-91-0357, AIAA 29th Aerospace Sciences Meeting, Reno, NV, Jan. 7-10, 1991.
2. G.S. Elliott, M. Samimy, and S.A. Arnette, "A Study of Compressible Mixing Layers Using Filtered Rayleigh Scattering," Paper #AIAA-92-0175, AIAA 30th Aerospace Sciences Meeting, Reno, NV, Jan. 6-9, 1992.
3. R. Miles and W. Lempert, "Two-Dimensional Measurement of Density, Velocity, and Temperature in Turbulent High-Speed Air Flows by UV Rayleigh Scattering," Applied Physics B 51, 1, 1990.
4. TRC Thermodynamics Tables (Non-Hydrocarbons), pp. k-190, ka-190, 1975.
5. S. Gerstenkorn and P. Luc, "Atlas du Spectre d'Absorption de la Molecule d'Iode, Part 3, p. 53, 1978.
6. S. Gerstenkorn and P. Luc, "Absolute Iodine ( $I_2$ ) Standards Measured by Means of Fourier Transform Spectroscopy," Revue de Physique Appliquee, 14, pp. 791-794, 1979.
7. J. Tellinghuisen, "Resolution of the Visible-Infrared Absorption Spectrum of  $I_2$  into Three Contributing Transitions," J. of Chemical Physics 58, pp. 2821-2834, 1973.
8. H. Shimizu, S.A. Lee, and C.Y. She, "High Spectral Resolution LIDAR System with Atomic Blocking Filters for Measuring Atmospheric Parameters," Appl. Opt. 22, pp. 1373-1381, 1983.

9. P. Luc, "Molecular Constants and Dunham Expansion Parameters Describing the B-X System of the Iodine Molecule," *J. of Molecular Spectroscopy* 80, pp. 41-55, 1980.

10. M. Kroll and K.K. Innes, "Molecular Electronic Spectroscopy by Fabry-Perot Interferometry. Effect of Nuclear Quadrupole Interactions on the Linewidths of the  $B^3\Pi_g^+$  -  $X^1\Sigma_g^+$  Transition of the  $I_2$  Molecule," *J. of Molecular Spectroscopy* 36, pp. 295-309, 1970.

11. M.D. Levenson and A.L. Schawlow, "Hyperfine Interactions in Molecular Iodine," *Physical Review A* 6, pp. 10-20, 1972.

12. J. Tellinghuisen, "Intensity Factors for the  $I_2$  B-X Band System," *J. of Quantitative Spectroscopy and Radiative Transfer* 19, pp. 149-161, 1978.

13. R.B. Miles, W.R. Lempert, B. Zhang, J. Forkey, and I. Glesk, "Rayleigh Imaging and Flow Tagging in Ground Test Facilities," *International Congress on Instrumentation in Aerospace Simulation Facilities Record*, pp. 255-261, 1991.

14. M. Winter and J.A. Shirley, United Technologies Research Center, Private Communication.

15. B.R. Tibbetts, R.B. Miles, W.R. Lempert, and P.D. Kenefick, Jr., "Optically-Based Air Data System," *Tenth National Aerospace Plane Technology Symposium*, Paper #185, April 23-26, 1991.



**AIAA 94-0492**

**THE DEVELOPMENT OF A TUNABLE, SINGLE-FREQUENCY ULTRAVIOLET LASER SOURCE FOR UV FILTERED RAYLEIGH SCATTERING**

**N. Finkelstein, J. Gambogi, W.R. Lempert, and R.B. Miles**  
PRINCETON UNIVERSITY  
Dept. of Mechanical & Aerospace Engineering  
Princeton, New Jersey 08544 08544 U.S.A.

and

**G.A. Rines, A. Finch, and R.A. Schwarz**  
SCHWARTZ ELECTRO-OPTICS, INC.  
Concord, Massachusetts 01742 U.S.A.

**32nd Aerospace Sciences  
Meeting & Exhibit**  
**January 10-13, 1994 / Reno, NV**

# THE DEVELOPMENT OF A TUNABLE, SINGLE-FREQUENCY ULTRAVIOLET LASER SOURCE FOR UV FILTERED RAYLEIGH SCATTERING

N. Finkelstein, J. Gambogi, W.R. Lempert,\* and R.B. Miles\*\*

Dept. of Mechanical & Aerospace Engineering  
PRINCETON UNIVERSITY  
Princeton, New Jersey 08544 U.S.A.  
609/258-2875

and

G. A. Rines, A. Finch, and R. A. Schwarz  
SCHWARTZ ELECTRO-OPTICS, INC.  
Concord, Massachusetts 01742 U.S.A.

## ABSTRACT

We present the development of a flexible, high power, narrow line width, tunable ultraviolet source for diagnostic application. By frequency tripling the output of a pulsed titanium-sapphire laser, we achieve broadly tunable (227-360 nm) ultraviolet light with high quality spatial and spectral resolution. We also present the characterization of a mercury vapor cell which provides a narrow band, sharp edge absorption filter at 253.7 nm. These two components form the basis for the extension of the Filtered Rayleigh Scattering technique into the ultraviolet. The UV-FRS system is comprised of four pieces: a single frequency, cw tunable Ti:Sapphire seeding source; a high-powered pulsed Ti:Sapphire oscillator; a third harmonic generation system; and an atomic mercury vapor filter. In this paper we discuss the development and characterization of each of these elements.

## 1. INTRODUCTION

In recent years there has been significant activity in the development of optical diagnostic techniques which utilize high power laser systems coupled with narrow band vapor filters.<sup>1-5</sup> Most of this work has been directed to high speed flow field application, although, Shimizu et. al. have reported a vapor filter LIDAR

approach for determining temperature in the mesopause.<sup>6</sup> To our knowledge, all of this work has utilized visible laser sources, such as second harmonic of Nd:YAG, Argon ion, or visible dye. While these systems have demonstrated significant potential, there are several distinct advantages of shifting into the ultraviolet: ultraviolet sources offer the advantage of both the frequency,  $\omega^4$ , and the index-of-refraction,  $(n-1)^2$ , enhancement of Rayleigh and Raman scattering cross sections, and elastic 'flare' scattering from stray surfaces is reduced due to reduced reflectivity.<sup>7</sup> These features combine to produce greatly enhanced signal strength and image contrast in the ultraviolet. Finally, as will be shown, atomic mercury vapor filters exhibit nearly ideal characteristics.

The potential of UV-FRS is critically dependent upon the ability to produce a reliable, tunable, high-power, narrow linewidth, ultraviolet light source. The optical system we are developing, as illustrated in Fig. 1, is comprised of three principal components: a cw single-frequency, tunable Ti:Sapphire source, a pulsed Ti:Sapphire oscillator, which is injection-locked to the cw source, and a frequency tripler. A commercial Schwartz Electro-Optics Titan cw laser is modified to allow for continuous tuning in the near infrared. The cw source is used to injection-seed a high-power, pulsed, Ti:Sapphire laser, the output of which is passed through a set of third harmonic generating crystals. The result is a high-power, pulsed, near transform limited spectrally, near diffraction limited spatially, tunable ultraviolet laser source.

This source and the narrow-band, atomic-mercury vapor absorption filter constitute the key elements of a UV-FRS diagnostic measurement. In the following, we give a description of our progress to-date in the development of each component of the UV-FRS system. In particular, we present a detailed characterization of the

\*Research Scientist, Mechanical & Aerospace Engineering, Member AIAA

\*\*Professor, Mechanical & Aerospace Engineering, Senior Member AIAA

mercury absorption band at 253.7 nm, including both experimental absorption scans and spectral modeling.

## **2. DEVELOPMENT OF TUNABLE cw SOURCE**

The goal of the cw source development effort is to generate continuously tunable, single frequency, near infrared laser light. Because the gain bandwidth of the titanium-sapphire is quite broad (680-1100 nm), it is an excellent medium for tunable laser sources. The laser is required to operate in both a high-power (1-3 Watt) and a low-power (milliwatt) regime for its two different tasks: cw mercury vapor spectroscopy, and high-power, pulsed oscillator seed source, respectively. Both tasks will be described in following sections.

By addressing the more taxing of the aforementioned goals, the multi-Watt level tunable output, we have been assured its success in operation as a spectroscopic tool and application as a seeder for the pulsed system. Figure 2 shows the schematic of the cw system. The Titan cw Ti:Sapphire laser system was pumped by a Coherent Inova 200 full-frame argon ion laser. Operated open cavity, the Ti:Sapphire laser system achieved 2.8 Watts of multi-mode output with 10 Watts of pump input. The cavity modes are spaced 250 MHz apart and the spatial mode is  $TEM_{00}$ .

To achieve single frequency, continuous scanning, the laser is operated in the ring configuration with a galvanometer-driven dual tilt plate assembly, and a piezo-electrically controlled scanning etalon. The coarse tuning element, a three-plate, bi-refringent filter, allows the laser to operate on one or more modes over a 15 GHz range. The tilt plates perform the continuous tuning by changing the effective cavity length.

The addition of a piezo-electric translator (pzt) driven etalon allows for single mode operation. The confocal air spaced etalon (Spectra Physics 761) is low finesse (approximately two, mirror reflectivity of 20%), and has a free spectral range of 75 GHz. By suppressing all other cavity modes below lasing threshold, the etalon acts to select the single, highest gain, longitudinal mode of the cavity. The single mode output is stabilized by adding a 2 kHz 'dither' to the etalon offset voltage, and by using a standard first derivative nulling<sup>8</sup> to provide feedback in the form of a quasi-dc bias voltage. The amplitude of the applied dither was 1 Volt, corresponding to a 100 MHz frequency modulation of the etalon, which produced a one milliwatt amplitude modulation of the laser power.

Calibration and linearity of the laser scan are essential for accurate spectroscopic characterization of the mercury vapor absorption. For this work, we have used a 1.5 GHz Fabry-Perot interferometer with custom built comparator circuit to monitor spectral continuity and linearity. A normal saw tooth ramp voltage was applied to the etalon at a much faster rate than the tuning of the laser. The comparator electronics consist of an analog sample and hold, which is triggered by the

occurrence of an etalon transmission peak. The voltage applied to the etalon, which is proportional to the relative frequency change, was measured each time an etalon transmission occurred. Each point of the recorded offset voltages varied from a linear fit by less than 2 percent. Thus, we could verify a constant scan rate. The etalon traces also reveal any discontinuities, mode hops, or multi-mode behavior of the laser. The absolute frequency of the system is determined by calibration with low pressure mercury vapor absorption, which will be discussed in detail below.

This single etalon and tilt-plate combination was found to reliably produce single-frequency tunable output. The laser system achieved 2.2 Watts single longitudinal mode tunable output at 761 nm, with 10 Watts of ion laser pump power. It could be reliably tuned, continuously, in excess of 15 GHz without adjustment of the bi-refringent filter. With appropriate tuning of the bi-refringent filter (micro-motor attachment and control), we anticipate that the system could be tuned for much greater (order of nanometer) intervals. The linearity of the tuning mechanism is better than 98% over 15 GHz, with the spectral line width approximately 1 MHz over milliseconds, and approximately 10 MHz over minutes.

## **3. DEVELOPMENT OF THE PULSED SYSTEM**

The ultimate purpose of the scanning cw system is to act as a seeder for a high-power, pulsed, injection-locked system, that will be used for diagnostic techniques such as UV Filtered Rayleigh Scattering. It is relatively straightforward to injection seed a high-power oscillator. However, without active feedback to adjust the pulsed laser cavity length, the output frequency will fluctuate between one and two longitudinal mode output.<sup>9</sup> When the seed laser frequency closely matches the resonance condition of the pulsed oscillator, the output is single mode. When the frequency of the seed beam lies between two cavity modes of the pulsed oscillator, the laser operates on both cavity modes. In the single mode case, the output is a near the transform-limited spectral line width; whereas, in the dual mode case, the output is 2.5 to 3 times the transform-limit, spectrally. For UV-FRS it is desirable to continuously scan, while maintaining true single mode frequency output. To this end, we are in the process of developing a control system to acquire and maintain single longitudinal mode operation.

The schematic of the injection seeded Ti:Sapphire system is given in Fig. 3. The second harmonic output (at 532 nm.) of a Continuum model YG-661 Nd:YAG laser serves as the pump for a breadboard version of a Schwartz Electro-Optics pulsed Ti:Sapphire laser. It is significant to note that the spatial mode of the Nd:YAG pump is near  $TEM_{00}$ . This requires the Ti:Sapphire crystal to be located at the intermediate field of the two focusing lenses, F1 and F2, in order to prevent surface

damage. After some experimentation, nominal 130 cm focal length lenses were positioned 70 cm in front of the Ti:Sapphire crystal faces. The cavity is purposely seeded in a lossy fashion. This provides a simple means of optical isolation of the cw cavity from high-power, pulsed light feedback. The cw seed signal is coupled into the pulsed oscillator cavity using the first turning prism, which is designed to be slightly off Brewster's angle, resulting in approximately 0.5% reflectivity. As needed, other optical isolators, lossy mirrors or Faraday isolators, are added. Approximately 100 microwatts is sufficient for seeding.

Some preliminary work has been done to demonstrate locking of the pulsed laser to the seed (cw) laser. The control system takes advantage of the fact that the pulsed resonator design is inherently low-Q, and, therefore, acts as an external cavity Fabry-Perot etalon for the cw seeding beam. Tuning the cavity length produces Fabry-Perot fringes with a modulation depth of approximately 50%, which can be easily detected by placing a photodiode detector behind the high reflector. Cavity stabilization was demonstrated by locking to a 'side' of the fringe at approximately the half height of the fringe. The locking was performed with a simple comparator circuit which returned a voltage proportional to the difference between the actual fringe transmission, and a variable reference value. The feedback signal is applied to the piezo-electrically mounted output coupler. Single frequency, pulsed operation, as determined by observation of a smooth temporal pulse profile, was achieved in the laboratory for periods on the order of minutes, although the seed laser could not be significantly tuned because of the rudimentary locking electronics.

For our purposes, there are distinct advantages of the fringe-locking mechanism over the standard pulse build-up minimization technique. The main difference between these two control systems is that the fringe, cavity resonance system offers continuous feedback, while the pulse build-up minimization system offers only shot-to-shot feedback. This latter mechanism of feedback control is most accurate when the pulse conditions are not rapidly changing. As a result, scanning must be very slow. Further, the effects of unstable ambient noise are not accounted for. By continuously monitoring the seed beam (except during the actual firing of a pulse), the fringe monitoring control allows for greater stabilization in less stable environments.

We are currently in the process of implementing a higher bandwidth, more robust version of the fringe-locking approach, based on the ramping of the piezo-electric material bias voltage through several fringe orders prior to each firing of the pulsed laser. A similar approach has been developed by workers at NIST in an injection-seeded, flashlamp-pumped ring dye laser.<sup>10</sup> It is anticipated that this system will provide continuous

tuning capability, and control bandwidth on the order of 100 kHz.

The resulting system yields high energy, single longitudinal mode output over a widely tunable range in the near infrared. The system produces 100 mJ/ pulse output in a 7 nsec pulse at 10 Hz, pumped at 280 mJ/ pulse at 532 nm. The spatial quality is TEM<sub>00</sub> and nearly diffraction limited.

#### **4. THIRD HARMONIC GENERATION**

Third harmonic generation is performed in the standard two step manner: type I doubling of the fundamental, and subsequent type II mixing of the residual fundamental with the second harmonic produced in the first step. Beta Barium Borate (BBO) is used for both steps. Figure 4 shows the conversion to third harmonic as a function of fundamental energy per pulse. The advantages of seeded operation are clearly evident. Seeding improves the spatial mode quality and reduces the bandwidth, both of which enhance the harmonic generation. Second harmonic generation is near the optimum of 67% internal conversion by power, or 50% conversion by photon. The conversion from the second to third harmonic is considerably lower, and results in a net conversion to third harmonic of 14% to 18%.

The same scheme is used for generation of cw tunable ultraviolet light; however, due to much lower power, a pair of BBO crystals is used in a wedged walk-off compensating geometry to produce the second harmonic. The dual crystal arrangement increases the second harmonic conversion by creating a longer effective interaction length than can be generated with a single crystal (due to walk-off of the Poynting and propagation vectors). The generation of third harmonic is identical to the pulsed set-up. Because of the low power, only trace amounts of tunable ultraviolet light is created (on the order of 10<sup>-10</sup> Watts). However, as we will demonstrate in the following section, this is sufficient to perform the Hg vapor spectroscopy.

#### **5. CHARACTERIZATION OF THE MERCURY FILTER**

Accurate characterization of the absorption spectra of optically thick mercury vapor is essential if it to be used as a filter medium. Appropriate characterization is critical for diagnostics which depend upon the knowledge of the filter profile to measure flow properties such as temperature, velocity, and density. Additionally, predictive modeling capability allows for construction of filters most appropriate to given experimental conditions. Characterization of the mercury filter is achieved by measuring transmission as a function of laser frequency. Computer models are used to quantify appropriate parameters such as maximum attenuation, and homogenous versus inhomogeneous broadening ratios.

Ideally, an atomic or molecular vapor filter will completely suppress background scattering while transmitting all Rayleigh or Raman scattered light. Four salient features characterize an ideal filter: infinitely sloped edges (to allow for a precise filter frequency cut-off), zero transmission over the entire width of the absorption band, unity transmission outside the filtering band, and a variable width filtering band.

Our mercury filter, consisting of a 5 cm. long by 5 cm. diameter all quartz cell with an 18 cm. side arm 'cold' tip, is shown in Fig. 5. The cell body, excluding the side arm portion, is wrapped in heating tape which controls the body temperature to  $\pm 1$  C. A water bath encloses the side arm and maintains constant temperature to  $\pm 0.1$  C. Prior to sealing, a small quantity (approximately 5 gms) of electronic grade mercury was inserted and the cell evacuated. The pressure inside the cell is estimated to be less than 0.05 torr. Since the heating tape maintains the cell body at a temperature higher than that of the water bath, the side arm temperature controls the vapor pressure of the mercury. Experiments were run characterizing the mercury absorption at side arm temperatures of 23 C, 70 C, and with the water bath replaced by a CO<sub>2</sub> slurry. These corresponds to vapor pressures of 0.0015 torr, 0.048 torr, and less than 10<sup>-5</sup> torr, respectively.

The experimental set-up for the absorption experiments is depicted in Fig. 2. The tunable output of the cw Ti:Sapphire laser is frequency-tripled, as previously described. A prism separates the fundamental and second harmonic from the 253.7 nm which is 50:50 split into reference and absorption legs. Twenty nanometer bandwidth interference filters are used in combination with solar blind photomultiplier tubes to avoid interference from scattered second harmonic light. The signal from the photomultiplier tubes is filtered through a low band-pass RC circuit (time constant of 0.01 seconds), and digitized with a laboratory computer based A/D system. The computer also collects a signal from the custom built comparator circuit which measures the relative frequency axis, as described previously. Complete (100%) transmission is determined by removing the cell from the beam path.

Figure 6 is a transmission profile of the mercury cell with a side-arm temperature of 23 C, and a body temperature of 48 C. This scan represents a sweep of approximately 30 GHz in the UV, or 10 GHz in the fundamental. Five strong, and one weak absorption lines are clearly evident. These different lines arise from the six different naturally-occurring isotopes of mercury. The isotopes are listed above their corresponding absorption lines. The odd isotopes have non-zero nuclear spin which produces hyperfine splitting. The even isotopes have zero nuclear spin and therefore each produces a single transition. The relative frequencies of these absorption bands agree well with earlier published values, which are represented as vertical lines on the bottom of the figure.<sup>11</sup> The square-bottomed shape of

the five strong absorption lines is characteristic of optically thick absorption (i.e. the absorption coefficient multiplied by the cell length is much greater than one). The Hg 196 absorption profile is not optically thick because of its low natural abundance of 0.14%. Between the discrete absorption bands we see an approximately flat transmission, at about 70% of the signal without the cell present. The 30% loss is due to the four uncoated window surfaces of the cell. With the beam blocked, a slight offset from zero exists corresponding to 1 nA of photomultiplier tube dark current.

A blow-up of the Hg 202 isotope absorption feature is given in Fig. 7, along with a computer model assuming a Voigt spectral lineshape. The figure demonstrates mercury's nearly ideal characteristics as a vapor filter. The sharp edges and flat base are characteristic of this very optically thick case. The modeling corresponds to an optical depth of approximately 71. [Line center attenuation is  $\exp(-71)$  or 10<sup>-31</sup>]. The 10% to 90% absorption edge occurs over 0.55 GHz, while the full width half maximum is 2.76 GHz. In Fig. 7, the Lorentzian component (FWHM) is fixed at 2.66 MHz, based on the mercury excited state natural lifetime of 120 nanoseconds. The Gaussian component (FWHM) is 1.067 GHz, corresponding to the cell body temperature of 48 C.

The measurement at the dry ice cold tip temperature verified that the 70% baseline transmission is due to window losses as opposed to continuum background absorption, which limits the extinction Iodine vapor-based cells.<sup>12</sup> This high off-line transmissivity allows for greater flexibility in design of vapor filter absorption bands, since the absorption characteristics (extinction and bandwidth) may be widely varied by altering the 'cold' tip temperature.

As an example of this, the side-arm was heated to 70 C, which increases the vapor pressure to 0.05 torr, and the optical depth to approximately 2000 (or maximum attenuation of 10<sup>-850</sup>). The cell temperature was kept at 105 C, which yields an inhomogeneous linewidth of 1.19 GHz (FWHM). As can be seen in Fig. 8, the width of the absorption band also increases rather dramatically. For naturally occurring isotopic abundance of mercury, the once separate absorption lines are no longer fully resolved. The fwhm of an individual absorption line increases from 2.76 Hz at 23 C, to an estimated 4.6 GHz at 70 C. Another significant feature, evident from Fig. 8, is the distinct presence of Lorentzian 'wings' on the absorption profile. Preliminary models verify the existence of this non-negligible Lorentzian wing assuming a linewidth of 2.66 MHz, or 0.22% of the 1.19 GHz Gaussian component. The Lorentzian contribution appears in the wings of the very optically thick Voigt profile, where it dominates due to its  $1/\Delta\omega^2$  frequency profile off line center. The significance for diagnostic measurements is that this represents a fundamental limit to the filter cut-off under extreme optically thick conditions.

To summarize, in examining the three mercury absorption spectra, the following salient features have been observed. In the optically thick regime, absorption lines appear to have sharp edges and flat bases. In our reference case of a 23 C, 5 cm length cell, we model an optical depth of approximately 71, and spectral bandwidth (FWHM) of 2.76 Hz. The bandwidth and optical depth may be varied significantly by altering the cold tip temperature; however, under extreme optically thick conditions, the Lorentz component becomes significant in the near wings. No measurable continuum absorption or other absorption features were observed.

## 6. CONCLUSIONS

The key elements of a flexible, high-power, single-frequency tunable ultraviolet source for diagnostic applications such as UV FRS have been demonstrated. A cw tunable, single-mode Ti:Sapphire laser has been constructed for use as a seeder for a pulsed titanium sapphire system, and as an independent cw spectroscopic tool. Detailed characterization of a mercury vapor absorption filter has shown it to exhibit nearly ideal characteristics, including exceedingly high line center attenuation, flat bottoms and sharp edges, variable bandwidth, and freedom from spectral interference.

## ACKNOWLEDGMENTS

The authors wish to acknowledge G. Scoles, K. Lehmann, and M. Souza for useful discussions, and P. Howard for providing technical assistance. This research was conducted with support from AFOSR, M.L. Energia, Inc., and NASA-Ames.

## REFERENCES

1. R.B. Miles and W.R. Lempert, *Appl. Phys. B* **51**, p.1 (1990).
2. G.S. Elliott, M. Samimy, and S.A. Arnette, AIAA-92-0175 (1992).
3. H. Komine, S.J. Brosnan, A.B., Litton, and E.A. Stappaerts, AIAA-91-0337 (1992).
4. J.A. Shirley and M. Winter, AIAA-93-0513 (1993).
5. J.W. Lee, J.F. Meyers, A.A. Cavone, and K.E. Suzuki, AIAA-93-0414 (1993).
6. H.S. Shimizu, S.A. Lee, and C.Y. She, *Appl. Opt.* **22**, p. 1373 (1983).
7. D.E. Gray, *American Institute of Physics Handbook*, 2nd ed., p. 6-119 (1963).
8. G.C. Bjorkland, *Opt. Lett.* **5**, p. 15 (1980).
9. R.L. Schmidt and L.A. Rahn, *Appl. Opt.* **25**, p.629 (1986).
10. G.J. Rosasco, W.J. Bowers, W.S. Hurst private communication. Nation Institute of Standards and Technology, Process Measurements Division, Gaithersburg, MD.
11. F. Bitter, *Appl. Opt.*, **1**, p. 1 (1962).
12. R.B. Miles, J.N. Forkey, and W.R. Lempert, AIAA-92-3894 (1992).

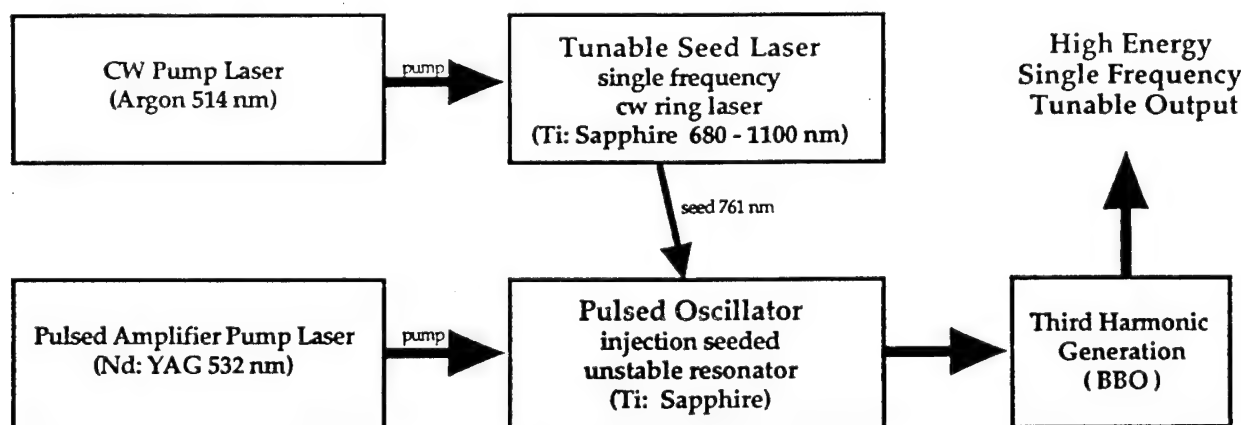


Fig. 1. Tunable single-frequency ultraviolet source.

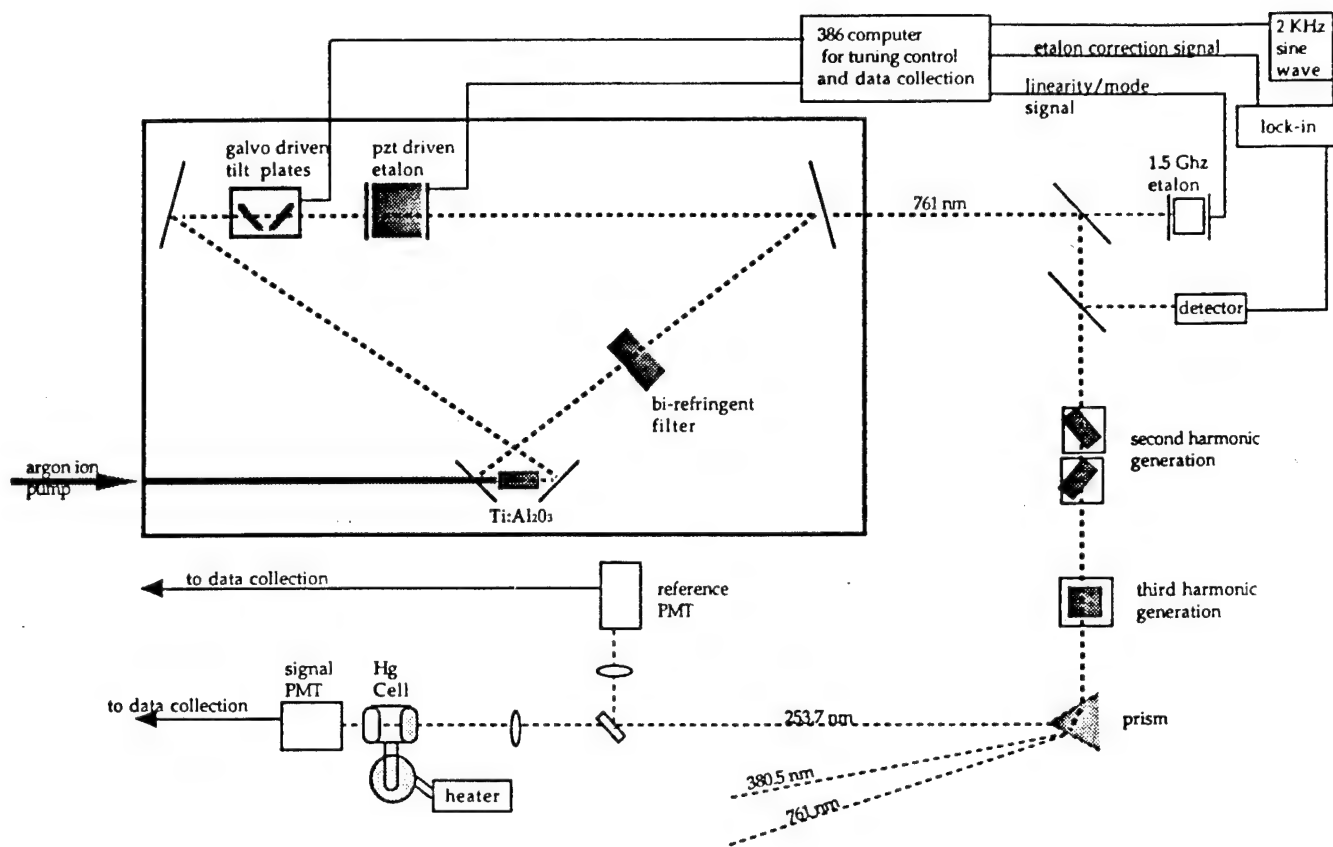


Fig. 2. cw Ti:Sapphire laser schematic with Hg spectroscopy experiment.

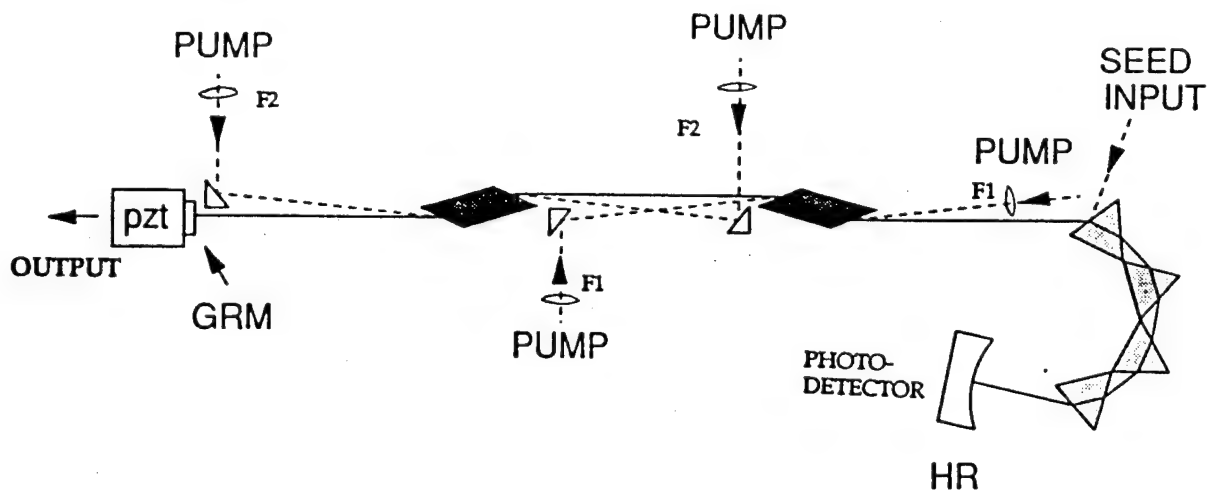


Fig. 3. Schematic illustration of pulsed laser oscillator.

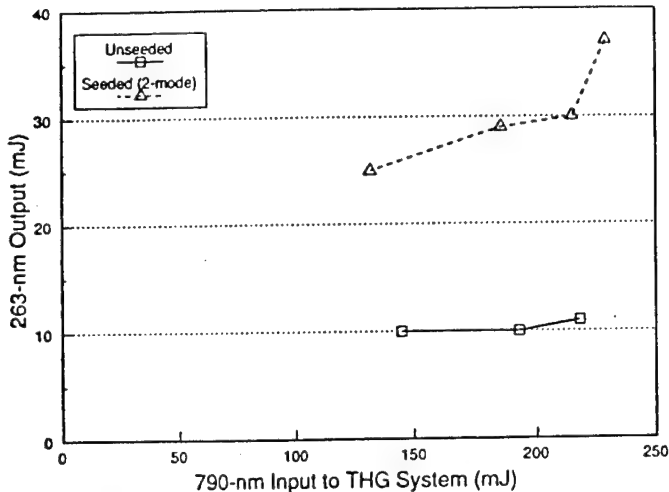


Fig. 4. Third-harmonic conversion efficiency at 790 nm.

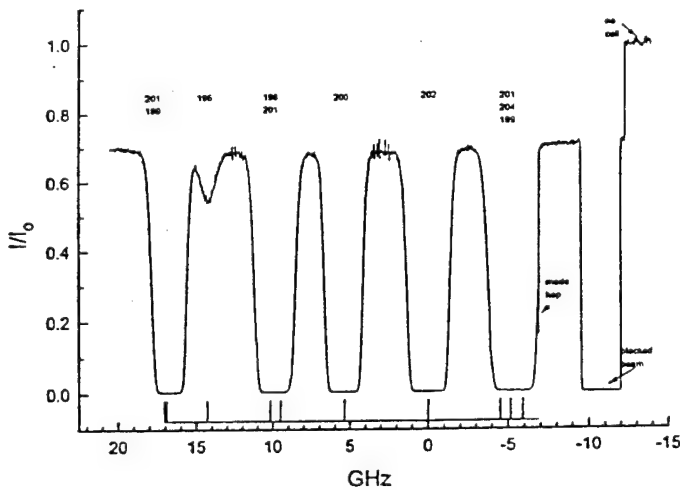


Fig. 6. Experimental Hg absorption with side-arm temperature of 23C, and cell body temperature of 48C.

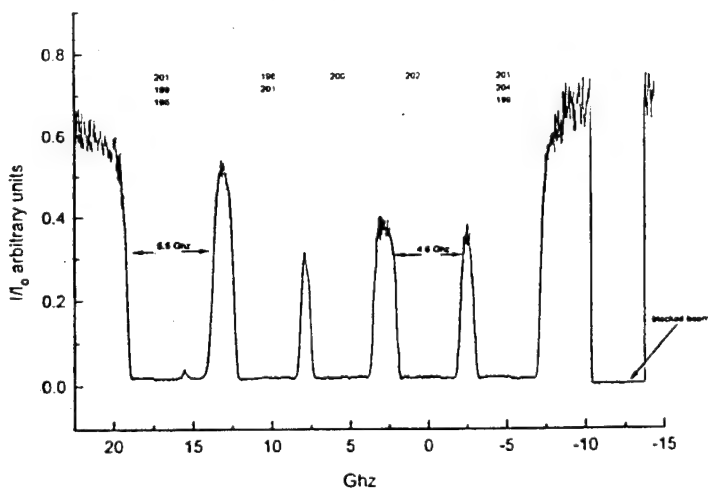


Fig. 8. Experimental Hg absorption with side-arm temperature of 70C, and cell body temperature of 105C.

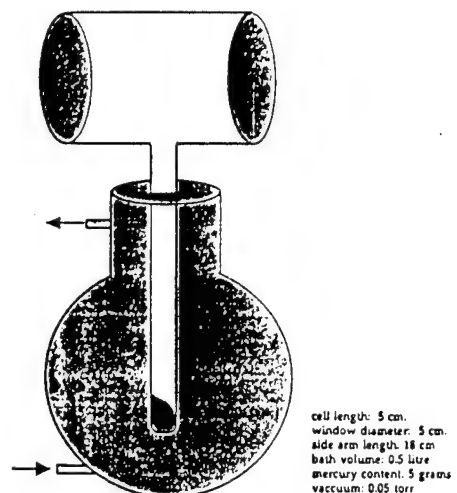


Fig. 5. Schematic illustration of mercury vapor cell and water bath.

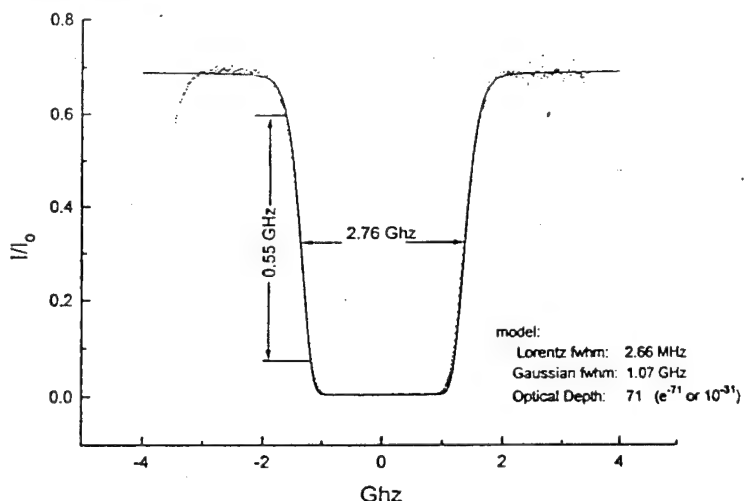


Fig. 7. Blow-up of experimental data (dotted) from Fig. 6 in vicinity of Hg 202 transition, along with modeling prediction (solid).



**AIAA 94-0491**

**VOLUMETRIC IMAGING OF SUPERSONIC  
BOUNDARY LAYERS USING FILTERED  
RAYLEIGH SCATTERING BACKGROUND  
SUPPRESSION**

**J.N. Forkey, W.R. Lempert, S.M. Bogdonoff,  
and R.B. Miles  
PRINCETON UNIVERSITY  
Dept. of Mechanical & Aerospace Engineering  
Princeton, New Jersey 08544 U.S.A.**

**and**

**G. Russell  
IBM THOMAS J. WATSON RESEARCH CENTER  
Yorktown Heights, New York 10598 U.S.A.**

**32nd Aerospace Sciences  
Meeting & Exhibit  
January 10-13, 1994 / Reno, NV**

# VOLUMETRIC IMAGING OF SUPERSONIC BOUNDARY LAYERS USING FILTERED RAYLEIGH SCATTERING BACKGROUND SUPPRESSION

J.N. Forkey, \* W.R. Lempert, \*\* S.M. Bogdonoff, † and R.B. Miles ††

Dept. of Mechanical & Aerospace Engineering  
PRINCETON UNIVERSITY  
Princeton, New Jersey 08544 U.S.A.  
609/258-5131

and

G. Russell

IBM THOMAS J. WATSON RESEARCH CENTER  
Yorktown Heights, New York 10598 U.S.A.

## ABSTRACT

We demonstrate the use of Filtered Rayleigh Scattering and a 3D reconstruction technique to interrogate the highly three dimensional flow field inside of a supersonic inlet model. A 3 inch by 3 inch by 2.5 inch volume is reconstructed yielding 3D visualizations of the crossing shock waves and of the boundary layer. In this paper we discuss the details of the techniques used, and present the reconstructed 3D images.

## 1. INTRODUCTION

The structure of the boundary layers and crossing shock waves in supersonic inlets is a critical factor affecting engine performance, wall loading, and heat transfer to the inlet surface. In addition, the role of the boundary layer in enhancing mixing phenomena and its effect on combustion dynamics are potentially important factors for the development and optimization of supersonic RAMJET engines.

While a number of laser-based diagnostic techniques are available for investigating flow properties away from surfaces in supersonic and hypersonic flows, many of these have difficulty interrogating boundary layers due to large reflections of laser light from walls and windows. When available, the information obtained from these techniques is usually displayed as data along a one-dimensional line, or across a two-dimensional plane. In many practical applications, however, information about the complex three-dimensional flow structure is needed to develop a full understanding of the flow.

In this paper, we describe the use of Filtered Rayleigh Scattering to image two-dimensional slices of the flow inside of a supersonic engine inlet model. These images are attained without artificially seeding the flow, and they extend from the floor of the inlet model (including the boundary layer) to beyond the center line. We also demonstrate the use of a reconstruction algorithm to generate three-dimensional, dynamic views of the space-filling data, which provides a volumetric visualization of the flow field inside the model.

## 2. EXPERIMENTAL SET-UP

The results presented below were obtained from experiments performed in the Princeton Gas Dynamics 8" by 8", high Reynolds number, Mach 3, blowdown wind tunnel. The tunnel was run with a stagnation temperature of 260 K, stagnation pressure of 100 psi and with a free stream Mach number of 3. A schematic of the inlet model which was placed in the 8"x 8" test section is shown in Fig. 1.<sup>1,2,3</sup> The model consisted of two 24-inch long flat plates, each mounted parallel to the wind tunnel floor and ceiling. The bottom plate was mounted 2 inches from the floor of the wind tunnel,

\*Graduate Student, Mechanical & Aerospace Engineering.  
Student Member AIAA

\*\*Research Scientist, Mechanical & Aerospace Engineering.  
Member AIAA

†Professor Emeritus, Mechanical & Aerospace Eng.,  
Fellow AIAA

††Professor, Mechanical & Aerospace Engineering,  
Senior Member, AIAA

while the top plate was mounted 2 inches from the ceiling of the wind tunnel (4 inches from the bottom plate). The boundary layer on the wind tunnel walls was approximately 1 inch thick at the leading edge of the flat plates, so the flow entering the model was free of any initial boundary layer (i.e., the top and bottom boundary layers inside the model were built-up starting from the leading edge). Between these two flat plates, were two variable angle vertical fins. The leading edges of the fins were separated by approximately 6 inches, and were 7.6 inches downstream of the leading edges of the flat plates. Although each fin angle could be varied independently from 5 degrees to 11 degrees with respect to the wind tunnel free stream flow direction, all of the data reported in this paper were taken with both fins set at 11 degrees. Optical access to the inlet model was provided by BK7 and quartz windows mounted in the floor and ceiling of the wind tunnel and in the two flat plates in the model.

In order to image the boundary layer close to the bottom flat plate, Filtered Rayleigh Scattering (FRS) was used.<sup>4,5,6</sup> The laser source was a frequency-doubled, injection-seeded, Nd:YAG laser which generated 5 ns pulses, each with 300 mJ of energy at a wavelength of 532nm. The laser light was focused into a sheet 0.8 mm thick and 7 cm wide and passed through the model oriented perpendicular to the flat plates, and spanwise with respect to the incident free stream flow (see Fig. 2). Light from the laser sheet was scattered by an ice vapor fog which is formed in the cold regions of the flow from a few parts per million residual water vapor in the compressed air supply. Other investigators have used larger amounts of water vapor or have seeded their flows with ethanol.<sup>7,8,9</sup> However, in our case, the FRS technique was sensitive enough that the residual concentration of water vapor was sufficient to obtain images. While scattering from this ice vapor fog precludes the possibility of observing molecular Rayleigh scattering, it provides a means of generating images with large contrast between "warm" and "cold" regions of the flow. In particular, interfaces across shocks, and interfaces between boundary layers and free stream flow are accentuated.

The light scattered from the flow in the downstream direction, was turned by a  $3\frac{1}{8}$  inch by  $1\frac{5}{8}$  inch, front surface aluminum mirror which was placed roughly 27 inches downstream of the leading edges of the flat plates. This mirror was mounted at an angle of 45 degrees to the tunnel walls, on the end of a sting arm. Light reflected from this mirror passed through a quartz window mounted in the side of the tunnel and was imaged by a Vivitar zoom lens, onto a double-intensified CID camera. The camera output was stored on videotape for subsequent analysis.

Images were taken at 26 different downstream locations inside of the model, with the farthest upstream location 12.3 inches downstream of the leading edges of the flat plates. Subsequent locations were separated from

each other by 0.1 inches. Each image captured a slice of the flow roughly 3 inches high and 3 inches wide. In order to preserve the camera magnification as the laser sheet was translated, the camera assembly was also translated in 0.1 inch increments.

Filtering of the scattered light was accomplished by placing a glass cell filled with iodine vapor in front of the camera lens. The cell was 3.25 inches long. The cell temperature was held at 80 C, and the vapor pressure was held at 1.44 torr by keeping the temperature of a cooler side arm at 44.5 C. An absorption profile for this cell in the frequency region of interest has been measured previously<sup>5</sup> and is shown in Fig. 3. By tuning the frequency of the injection seeded laser to overlap the strong absorption feature labeled A in Fig. 3, much of the stray scattering from walls and windows was absorbed by the iodine cell before it reached the camera since this stray light was at the same frequency as the incident laser light. Light scattered from the flow, however, was Doppler-shifted to a frequency outside of absorption feature A (see Fig. 3), and so this light passed through the iodine cell and was imaged onto the camera. Because the viewing angle in this experiment was 180 degrees with respect to the free stream velocity, and 90 degrees with respect to the illumination source, the Doppler shift due to the flow velocity was large (on the order of 1 GHz), so this experiment was an ideal application of the Filtered Rayleigh Scattering technique. In order to illustrate the utility of Filtered Rayleigh Scattering in this configuration, Fig. 4 shows two images taken with the camera "zoomed in" on the upper boundary layer. Figure 4a shows the image obtained without using the vapor filter. Here it is impossible to see any of the roughly 5mm thick boundary layer. Figure 4b is identical to that of Fig. 4a except that this image was acquired using FRS. In this case, the boundary layer is clearly visible.

### 3. DATA PROCESSING

Images were initially stored on video tape, and were subsequently processed using a Data Translation DT1451 frame-grabber installed on a Sun 4 Workstation. A single image from each of the 26 different downstream locations was used for the three-dimensional reconstruction. Because the turning mirror oscillated slightly in the horizontal direction during wind tunnel runs, each image was digitally shifted using as a reference a vertical line located half way between the two shocks generated by the two fins. Other image processing operations that were performed were a standard cropping of the image to eliminate data outside of the field of interest, and a standard greyscale stretch to increase contrast. Because the greyscale stretch was performed after digitization, the dynamic range of the final images was not as large as it would have been if the gain on the camera amplifier had been set higher, or if an analog amplifier had been used when the images were

transferred from the VCR to the frame grabber. We have incorporated such an amplifier into the system for future experiments. Finally, strong, spurious noise signals, which were generated by scattering of laser light by large particles in the flow, were artificially removed from some images when the area surrounding these signals was uniformly black. These large particles, probably "large" ice crystals, are observed near the end of each wind tunnel run. Given a sufficient number of wind tunnel runs, it would have been possible to limit run times so as to avoid generating these particles. However, due to wind tunnel time constraints, this was not done.

The processed two-dimensional images are shown in Fig. 5. In the first 11 images, the edge of the turbulent boundary layer on the bottom flat plate is clearly visible. Outside of the boundary layer, where the static temperature is cold, the ice vapor fog is present, and much light is scattered. Within the boundary layer, however, the static temperature is much higher, so the ice vapor fog disappears, and very little light is scattered. The interface between the dark and light regions, therefore, indicates the location of the gradient in static temperature at the edge of the boundary layer. The effect on the boundary layer, of the strong pressure gradients generated across the vertical shocks is clearly seen in these images. Boundary layer fluid is forced to the centerline of the model causing a "bulging" of the boundary layer as the flow moves downstream.

Shock locations in these images are also clearly visible. In the first 7 images taken at locations ahead of the shock crossing point, the shocks are observed as curved lines of slightly increased intensity extending from the top of the field of view to the bottom boundary layer. In the images taken farther downstream, beyond the shock crossing point, the static temperature after the shocks is high enough that the ice vapor fog disappears completely, and so shocks are observed here as sharp discontinuities between bright and dark regions of the images. The two crossing shocks observed in these images exhibit a continuous curvature from the bottom boundary layer to the top of the field of view. This is in contrast to the shocks observed by Garrison and Settles et. al. inside an inlet model without a top flat plate.<sup>9</sup> In this latter case, shocks were observed to be curved close to the boundary layer, but straight and vertical farther from the bottom plate.

#### 4. THREE-DIMENSIONAL RECONSTRUCTION

In order to increase our understanding of the evolution of the shocks and boundary layer as they move through the inlet model, we have utilized a display method which was developed for viewing translucent 3-D space-filling data.<sup>10,11</sup> This method projects the 3-D space-filling data onto a 2-D screen (the computer screen) which is located at some specified distance from the center of the 3-D volume, and at an angle determined by the specified observer location (see Fig. 6). The

intensity of each pixel on the computer screen is determined by tracing rays from the back of the data set to the observer's location, through all of the data slices. At each intersection point between the ray and an individual volume element (voxel), the "incoming intensity," generated from voxels farther from the observer is first attenuated by a value determined by the voxel data value and then incremented by an amount proportional to the data value. This method creates an image with "partial transparency" where, as in viewing fog, data closer to the observer partially obscures data farther back. Mathematically, this can be expressed as:

$$I_{out} = I_{in} \cdot \exp(-\alpha L) + I_{local} \quad (1)$$

where  $I_{in}$  is the intensity generated by previous data slices;  $I_{local}$  is the local source intensity--a function of data value;  $\alpha$  is the local absorption coefficient--also a function of data value; and  $L$  is the distance between data slices. This technique is capable of projecting onto a 2-D screen not only solid surfaces, but also, because of the partial transparency, objects embedded within the 3-D volume.

This technique was used to generate 2-D projections of the 3-D flow in the inlet model at a number of different viewing locations. All of the viewing angles placed the observer slightly above the inlet model, looking down at an angle of 30 degrees. Different viewing locations varied as the observation angle was rotated about the imaginary vertical axis passing through the center of the inlet model. This angle was varied from 0 degrees to 360 degrees in three degree increments. Examples of the resulting 2-D projections are shown in Fig. 7.

These reconstructions provide a way to view all of the data in one 2-D image. While individual projections yield some insight into the three dimensionality of this flow, two additional techniques further enhance the perceived three-dimensionality. By rapidly displaying images reconstructed with successive observation angles (each separated by three degrees from the previous one), the data is observed as a rotating volume. This rotation greatly increases the perception of three dimensionality by allowing the observer to perceive relative locations of different portions of the data. This dynamic approach simulates the way one naturally observes a complex volumetric object by moving one's head.

Because it is not always possible to rapidly re-display the reconstructed images, particularly in a manuscript, we have also investigated the use of stereo pairs of images. The image shown in Fig. 7b is re-displayed in Fig. 8, along with its associated stereo pair. The viewing of such stereo pairs can be aided by coloring one of the images blue, and adding to it the second image colored red. Then the three-dimensionality is perceived by viewing this composite picture through glasses with one red lens and one blue lens. Although this multi-color scheme aids in the viewing of stereo

pairs, we have found that the use of apparent motion is, by far, the better method for understanding the three-dimensionality of space-filling data. For this particular data set, the use of this dynamic technique allowed for a clearer understanding of the three-dimensional shape of the shocks. Particularly noticeable were the curvature of the shocks, as well as the shape of their approach towards and separation after the crossing point.

In order to focus in on the 3-D shape of the boundary layer, the first 11 images, which show a well defined boundary layer edge, were cropped just above the boundary layer. Also, the greyscale values were inverted in order to highlight the boundary layer. These cropped and inverted image slices were then used to generate the 3-D reconstructions as described above. Once again, rotating images were generated and were used to observe the "central bulging" of the boundary layer as it moved downstream. A stereoscopic pair of images showing this effect is shown in Fig. 9.

### 5. FUTURE WORK

Future efforts will be aimed at achieving two goals. The first is to image molecular Rayleigh scattering in this inlet model. This will allow for the investigation of the flow farther downstream where the flow is too warm to support the ice vapor fog. In addition, it will allow for the investigation of this entire flow, when run with pure nitrogen. Preliminary results were obtained using the setup described above with the laser sheet moved to a point 16 inches downstream of the leading edges of the flat plates: a location where the ice fog no longer appears. With no further optimization of laser seeding efficiency, iodine filter characteristics, or collection geometry, the time averaged image shown in Fig. 10b was obtained. Because of motion of the turning mirror, edges in this image are not very sharp. However, this image shows that the variation in intensity across the edge of the boundary layer can be detected with this FRS technique. By contrast, a similar image was taken with the FRS technique disabled. This image is shown in Fig. 10a. In this case, stray wall scattering completely overwhelms the Rayleigh scattering.

The second major area under investigation is the further development of FRS to be able to make quantitative measurements of temperature, density and velocity. Early work in this area has already been reported.<sup>5</sup> In this work, we found that one of the major sources of systematic uncertainty is due to uncertainty in laser frequency. Currently under development is a system which accurately measures laser frequency by measuring the beat frequency between the interrogation laser and a reference laser locked to a well characterized iodine absorption line. We expect that this system will be able to measure laser frequency to an accuracy on the order of 1MHz. This corresponds to a velocity uncertainty, for example, on the order of 1 m/s.

### 6. CONCLUSIONS

In this work, we have demonstrated the utility of the Filtered Rayleigh Scattering technique for investigating complex supersonic flows. In particular, FRS is especially useful when imaging boundary layers close to surfaces, where stray scattering would otherwise be a problem. We have also demonstrated the utility of a 3D reconstruction technique, which, when used in a dynamic mode, can generate the perception of a rotating volume of data. Alternatively, stereo pairs of images can be used to generate 3D perception.

Finally, we expect that future work will allow for the imaging of molecular Rayleigh scattering, and will generate quantitative data with lower levels of experimental uncertainty.

### ACKNOWLEDGMENTS

We wish to acknowledge Carl Delo and Jon Poggie for their help in generating the 3D reconstructions. Also, we would like to acknowledge Bill Stokes for his help in setting up and running the wind tunnel experiments.

This research was conducted with support from the AFOSR and NASA-Langley. In addition, J. Forkey was supported by a graduate student researchers fellowship from NASA-Lewis.

### REFERENCES

1. K. Poddar and S. Bogdonoff, "A Study of Unsteadiness of Crossing Shock Wave Turbulent Boundary Layer Interactions," AIAA #90-1456, 21st Fluid Dynamics, Plasma Dynamics and Lasers Conference, Seattle, WA, June 18-20, 1990.
2. N. Narayanswami, D. Knight, S.M. Bogdonoff, C.C. Horstman, "Crossing Shock Wave--Turbulent Boundary Layer Interactions," AIAA 91-0649, 29th Aerospace Sciences Meting, Reno, NV, Jan. 7-10, 1991.
3. S.M. Bogdonoff and W.L. Stokes, "Crossing Shock Wave Turbulent Boundary Layer Interactions--Variable Angle and Shock Generator Length Geometry Effects at Mach 3," AIAA 92-0636, 30th Aerospace Sciences Mtg. Exhibit, Reno, NV, Jan. 6-9, 1992.
4. R.B. Miles, W.R. Lempert, and J. Forkey, "Instantaneous Velocity Fields and Background Suppression by Filtered Rayleigh Scattering," AIAA 91-0357, 29th Aerospace Sciences Mtg., Reno, NV, Jan. 7-9, 1991.
5. R.B. Miles, J.N. Forkey, and W.R. Lempert, "Filtered Rayleigh Scattering Measurements in Supersonic/Hypersonic Facilities," AIAA 92-3894, 7th Aerospace Ground Testing Conf., Nashville, TN, July 6-8, 1992.

6. G.S. Elliott, M. Samimy, and S.A. Arnette, "Molecular Filter-Based Diagnostics in High-Speed Flows," AIAA 93-0512, 31st Aerospace Sciences Meeting and Exhibit, Reno, NV, Jan. 11-14, 1993.
7. G.S. Elliott, M. Samimy, and S.A. Arnette, "A Study of Compressible Mixing Layers Using Filtered Rayleigh Scattering," AIAA 92-0175, 30th Aerospace Sciences Meeting and Exhibit, Reno, NV, Jan. 6-9, 1992.
8. F.S. Alvi and G.S. Settles, "Physical Model of the Swept Shock Wave/Boundary Layer Interaction Flow Field," AIAA Journal 30, Sept. 1992, p. 2252.
9. T.J. Garrison and G.S. Settles, "Flow Field Visualization of Crossing Shock Wave/Boundary Layer Interactions," 30th Aerospace Sciences Meeting and Exhibit, Reno, NV, Jan. 6-9, 1992.
10. G. Russell and R.B. Miles, "Display and Perception of 3-D Space-Filling Data," Applied Optics 26, March 15, 1987, p. 973.
11. C. Delo, J. Poggie, and A.J. Smits, "A System for Imaging and Displaying Three-Dimensional, Time-Evolving Passive Scalar Concentration Fields in Fluid Flow," Princeton University MAE Dept. Technical Report #1992, Jan. 1994.

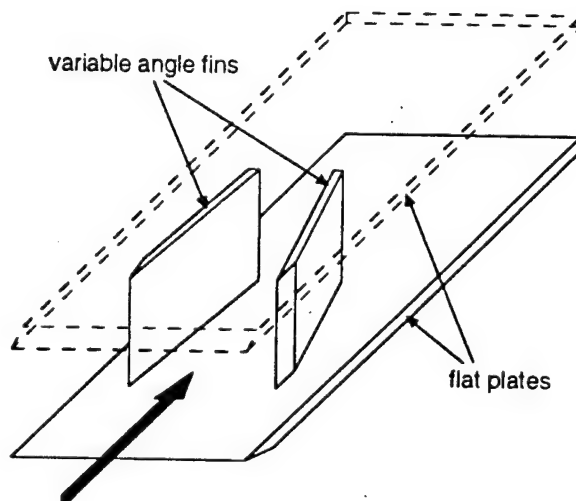


Fig. 1) Experimental model of supersonic inlet. Flat plates are separated by 4 inches. Leading edges of fins are separated by 6 inches.

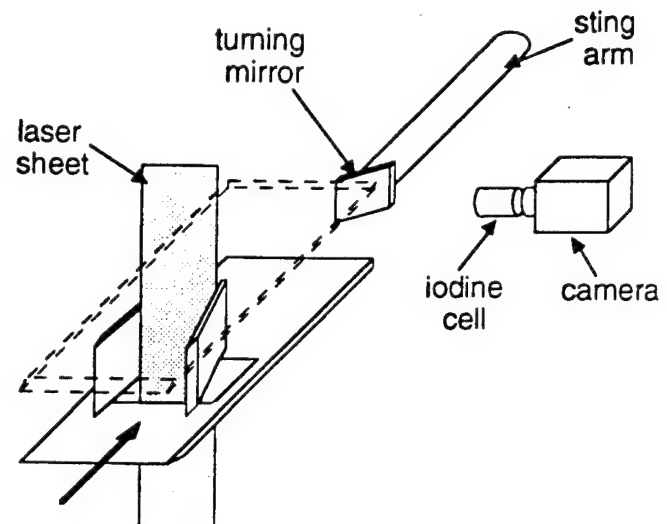


Fig. 2) Experimental setup for Filtered Rayleigh Scattering technique.

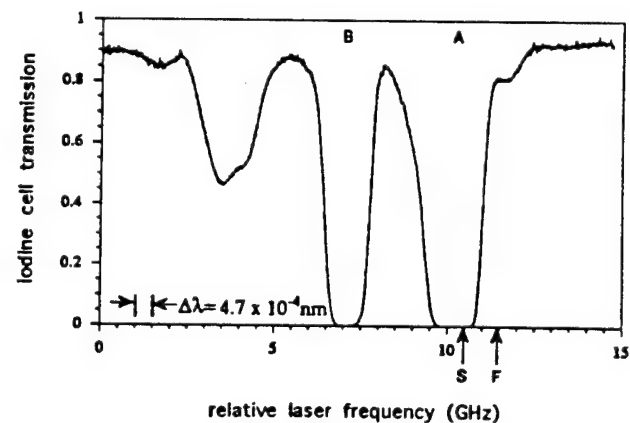
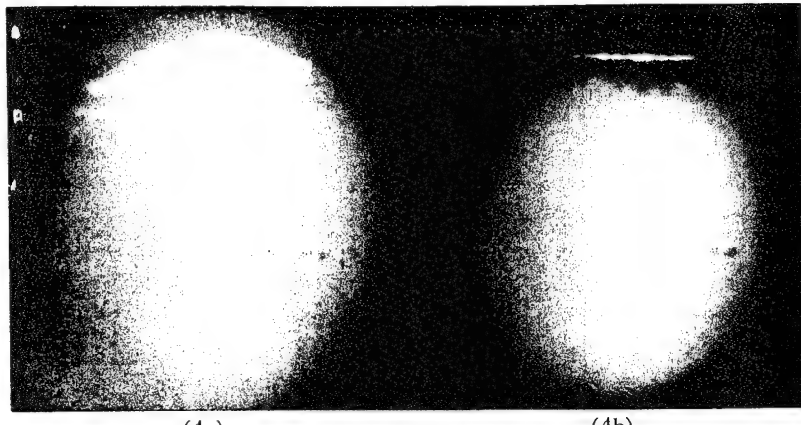


Fig. 3) Absorption profile of iodine cell near 532 nm. The absorption feature labelled "A" was used as the filter in the work reported here. Stray scattering was at the frequency indicated by "S", while scattering from the free stream of the flow was at the frequency indicated by "F".



(4a) (4b)

Fig. 4) Images of the boundary layer on the top flat plate  
a) taken without using FRS, b) taken with FRS.

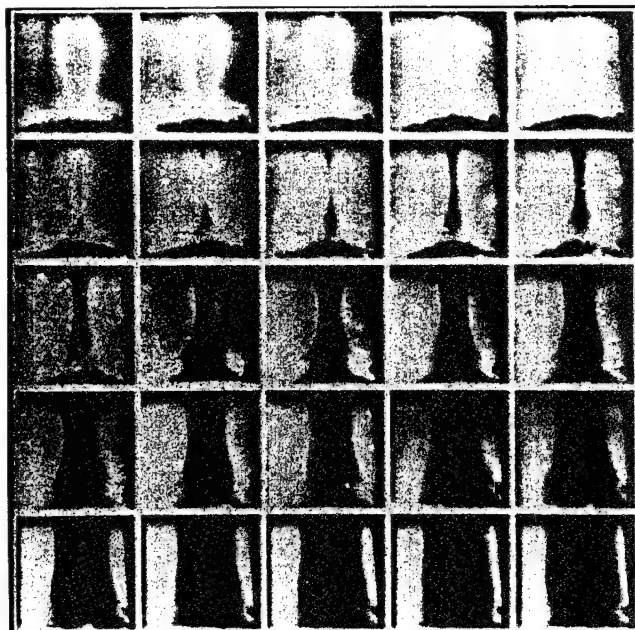


Fig. 5) 3 inch by 3 inch slices of data showing shock structure and bottom plate boundary layer. The image on the top left was taken 12.4 inches downstream of the leading edge of the flat plate. Subsequent images were separated from each other by 0.1 inches.

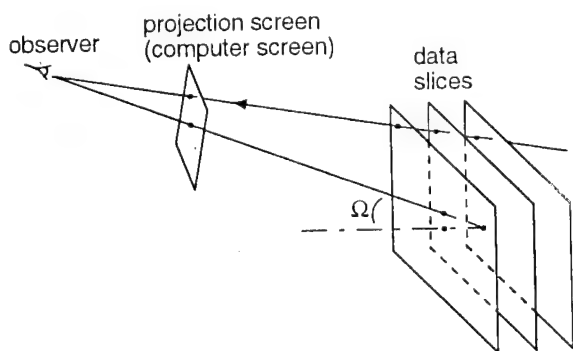
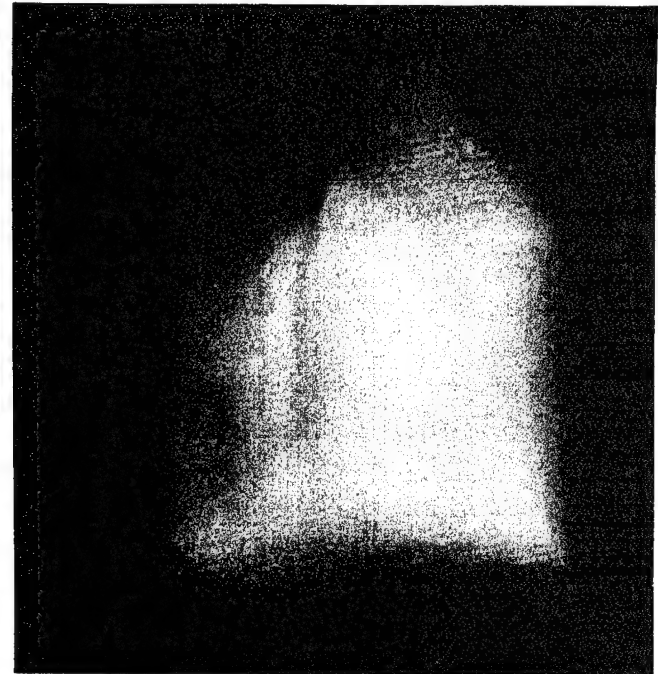
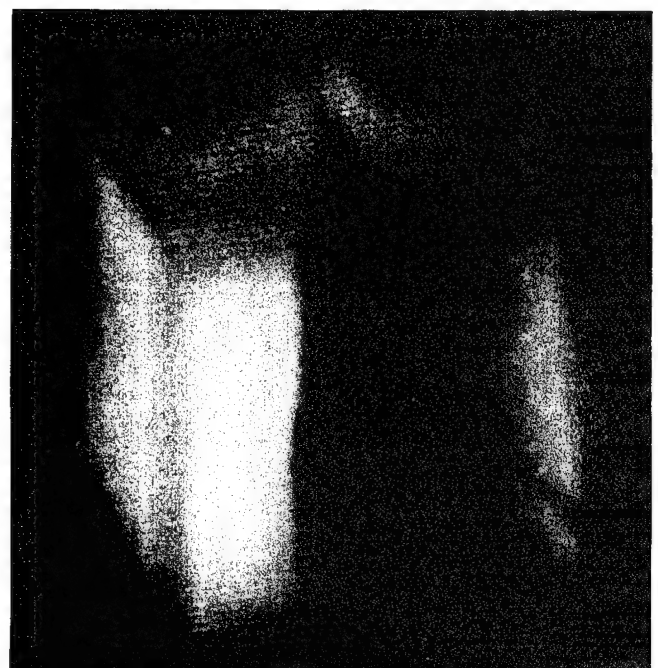


Fig. 6) Geometry used in 3D reconstruction technique.



(Fig. 7a)



(Fig. 7b)

Fig. 7) These images are two examples of the images obtained from the 3D reconstruction technique. a) This image was generated for an observer looking downstream from a location before the shock crossing point. Shocks are visible before the crossing point as brighter regions of the volume. b) This image was generated for an observer looking upstream from a location beyond the shock crossing point. Shocks are visible after the crossing point as sharp discontinuities in brightness.

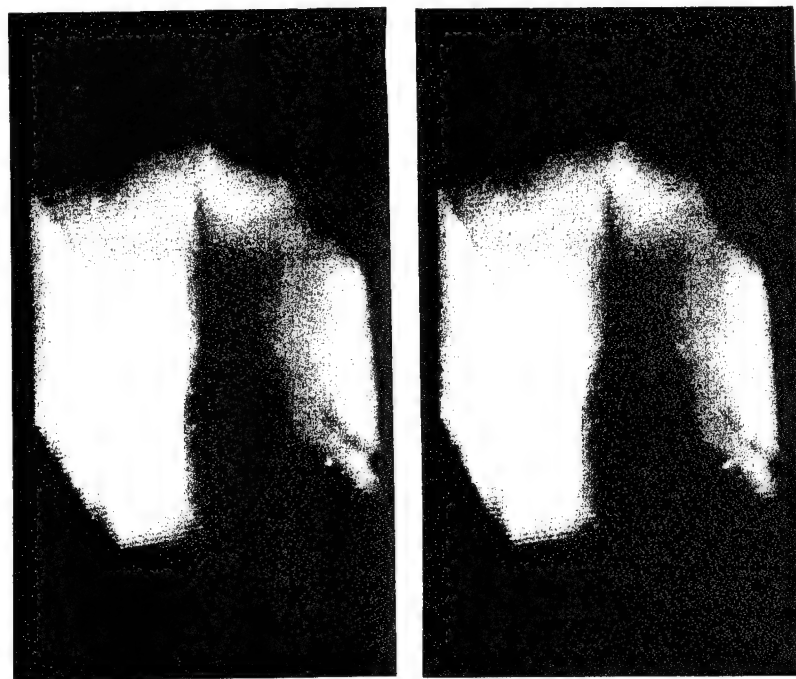


Fig. 8) This is the image in figure 7b redisplayed with its stereopair.

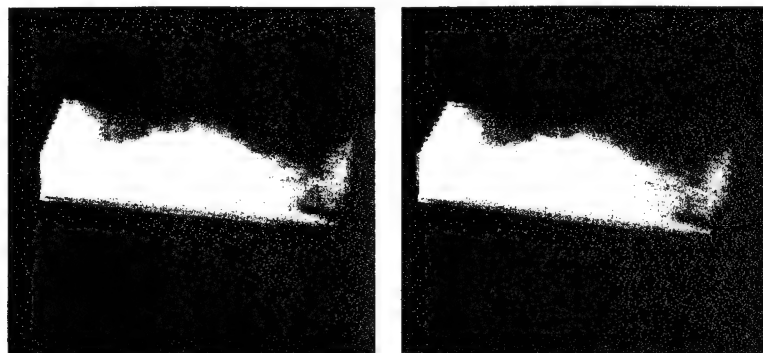
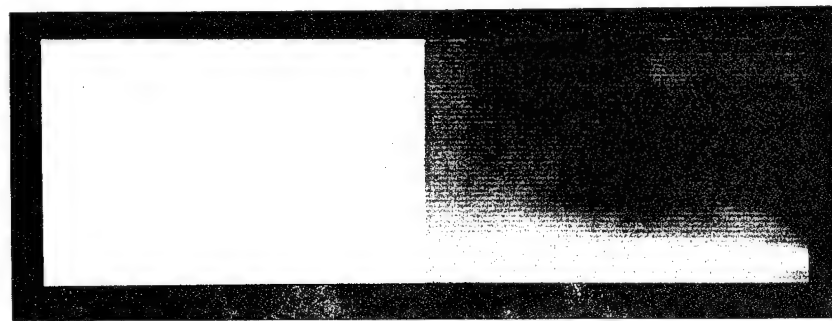


Fig. 9) Stereopair of boundary layer as seen by an observer looking downstream.



(Fig. 10a)

(Fig. 10b)

Fig. 10) Images of molecular Rayleigh scattering taken 16 inches downstream of the leading edges of the flat plates, a point where ice vapor is not present. a) Image taken with no filtering. b) Image taken using Filtered Rayleigh Scattering, showing semicircular boundary layer.



AIAA-95-0298

## CONTROL OF EXPERIMENTAL UNCERTAINTIES IN FILTERED RAYLEIGH SCATTERING MEASUREMENTS

J.N. Forkey, N.D. Finkelstein, W.R. Lempert, and R.B. Miles

PRINCETON UNIVERSITY  
Dept. of Mechanical & Aerospace Engineering  
Princeton, New Jersey 08544 U.S.A.

**33rd Aerospace Sciences  
Meeting and Exhibit**  
**January 9-12, 1995 / Reno, NV**

# CONTROL OF EXPERIMENTAL UNCERTAINTIES IN FILTERED RAYLEIGH SCATTERING MEASUREMENTS

J. N. Forkey,\* N. D. Finkelstein,\* W. R. Lempert,† and R. B. Miles‡

Department of Mechanical and Aerospace Engineering  
PRINCETON UNIVERSITY  
Princeton, New Jersey 08544 U.S.A.  
609/258-5131

## ABSTRACT

Filtered Rayleigh Scattering is a technique which allows for measurement of velocity, temperature, and pressure in unseeded flows, spatially resolved in 2-dimensions. We present an overview of the major components of a Filtered Rayleigh Scattering system. In particular, we develop and discuss a detailed theoretical model along with associated model parameters and related uncertainties. Based on this model, we then present experimental results for ambient room air and for a Mach 2 free jet, including spatially resolved measurements of velocity, temperature, and pressure.

## 1. INTRODUCTION

Filtered Rayleigh Scattering (FRS), a recently developed flow diagnostic technique,<sup>1,2</sup> achieves large suppression of background scattering for whole field flow visualization, and obtains quantitative measurements of velocity, temperature and density, in unseeded gaseous flows.

This technique makes use of Rayleigh scattering from molecules in the flow, and is driven by a high power, injection seeded laser. By imaging the scattered light onto a CCD camera, one may obtain an image of

flow density. In order to filter out unwanted background scattering from stationary objects in the field of view, the laser is tuned in frequency to coincide with an atomic or molecular absorption line. A cell containing the atomic or molecular species is then placed between the camera and the flow. If the cell temperature, pressure, and length are set appropriately, the absorption line can be made optically thick, so that the cell acts as a notch filter, absorbing all scattering at the laser frequency. Because the flow is moving, the Rayleigh scattering is Doppler shifted, and therefore, passes through the atomic or molecular filter, and is imaged on the camera.

In order to extend the technique to make quantitative measurements, one must take advantage of the fact that the amount of light reaching any resolution element of the camera is a function of the total intensity of the Rayleigh scattering (flow density), as well as the overlap of the Rayleigh scattering profile with the filter absorption profile. This overlap is a function of the central frequency of the Rayleigh profile, which is determined by flow velocity (Doppler shift), and the spectral shape of the Rayleigh profile, which is a function of the flow temperature and pressure. In order to uniquely determine the parameters,  $v$ ,  $T$ , and  $P$  experimentally, it is necessary to collect data (resolution element intensity) for varying conditions. A minimum of three data points are required to capture the three parameters. By imaging the scattering through multiple filters with different absorption profiles, or by observing the scattering from several different angles simultaneously, or by monitoring intensity at the camera while tuning the frequency of the laser, it is possible to determine the pertinent parameters of the Rayleigh scattering profile, and, therefore, the velocity, temperature, and pressure at each resolution element.

Previous work has been concentrated into two areas. The first is the use of this technique for background suppression when visualizing flows, and the second is for the measurement of velocity. The background

\*Graduate Student, Mechanical & Aerospace Engineering,  
Student Member, AIAA

†Research Scientist, Mechanical & Aerospace Engineering,  
Member, AIAA

‡Professor, Mechanical & Aerospace Engineering,  
Senior Member, AIAA

Copyright © 1995 by the American Institute of  
Aeronautics and Astronautics, Inc. All rights reserved.

suppression feature of Filtered Rayleigh Scattering has been used to image flow fields that otherwise would be completely obscured by the strong scattering from wind tunnel surfaces. We have used this technique to image the flow field inside a Mach 3 inlet, and to generate volumetric images of the crossing shocks and boundary layers present.<sup>3</sup> Elliot and coworkers<sup>4</sup> have also used this technique to observe structures in compressible mixing layers. Measurements of velocity have been investigated by a number of workers. The measurement of velocity in a seeded compressible mixing layer was performed by Elliot,<sup>5</sup> and velocities over a delta wing in a seeded air flow were measured by Meyers, et. al.<sup>6</sup> using a technique similar to Filtered Rayleigh Scattering, called Doppler Global Velocimetry. The use of Filtered Rayleigh Scattering in unseeded flows for measuring mass flow has been investigated by Winter and Shirley,<sup>7</sup> and velocity measurements in an unseeded Mach 5 flow have been made by our group.

Current work utilizes laser scanning to obtain a complete Rayleigh scattering spectrum for each measurement point. This method of data collection offers the advantage of many data points for model fitting; however, such a method yields time averaged results. The work reported here makes use of two laser/filter pairs. The first consists of a frequency doubled, injection seeded, Nd:YAG laser, along with a molecular iodine absorption cell and the second consists of a frequency tripled, injection seeded, Ti:Sapphire laser along with an atomic mercury filter.

In this paper, we continue the development of Filtered Rayleigh Scattering as a tool for measuring velocity in unseeded flows, by discussing the major sources of systematic uncertainties in FRS experiments, and by discussing techniques that have been developed to minimize these. Although temperature and pressure are measured during an unseeded experiment, these will be discussed only briefly and qualitatively in the results section of this paper; future work will concentrate on quantifying the measurements of these parameters more fully. Our discussion begins with a theoretical model of the scattering and detection processes, which can be used to determine flow parameters from camera intensity values. This is followed by discussions of each of the three major components of a Filtered Rayleigh Scattering experiment -- laser, filter, and camera -- along with corresponding analyses of the major sources of uncertainties, and techniques used to control them. We then demonstrate the utility of FRS by presenting experimental measurements along with a detailed error analysis of the velocity data obtained from an unseeded flow facility and Nd:YAG/iodine filter pair. Two sets of experimental conditions yield velocity fields spatially resolved in two dimensions. We conclude with a discussion of the development of ultraviolet FRS utilizing a frequency tripled Ti:Sapphire laser and a mercury absorption filter. Although the discussions here focus on measurements made using molecular Rayleigh scattering,

many of the considerations are directly applicable to experiments which make use of particle scattering.

## 2. THEORETICAL MODEL

Accurate measurement of flow velocity, temperature and pressure from raw experimental data requires complete understanding of the processes occurring. Furthermore, it is necessary to have an accurate model describing experimental data in order to deduce the measurements of interest. For a Filtered Rayleigh Scattering experiment, the pertinent raw data consists of grayscale value,  $S$ , at a particular resolution element of the camera. Our model, therefore, predicts this signal level for any experimental configuration.

When a laser pulse with energy per unit area of  $E_I$ , lineshape profile  $l(v)$  and central laser frequency of  $v_I$ , relative to some reference frequency, is incident on a region of flow with pressure  $P$ , and temperature  $T$ , the Rayleigh scattered energy,  $E_R$  at frequency  $v$  relative to the reference frequency, scattered from an interrogation volume  $V$ , into the solid angle  $d\Omega$ , is given by the convolution of the laser lineshape  $l(v)$  and the Rayleigh-Brillouin scattering profile  $g(v)$ :

$$E_R(v) = E_I \frac{PV}{kT} \frac{d\sigma}{d\Omega} d\Omega \int_{-\infty}^{\infty} l(v - (v_I + v_D) - v') g(v') dv' \quad (1)$$

Here,  $k$  is equal to Boltzmann's constant, and  $\frac{d\sigma}{d\Omega}$  is the differential Rayleigh scattering cross section. The laser lineshape  $l(v)$  is centered at  $v_I$  and shifted by the Doppler shift  $v_D$ :

$$v_D = \frac{2v}{\lambda} \sin\left(\frac{\theta}{2}\right) \quad (2)$$

where  $v$  is the flow velocity in the direction to which the experimental system is sensitive (i.e.  $v$  is the velocity component in the direction which bisects the angle between the vector extending from the scattering center to the camera, and the vector pointing opposite the laser propagation vector).  $\lambda$  is the absolute laser wavelength and  $\theta$  is the scattering angle. The Rayleigh - Brillouin scattering profile,  $g(v)$ , is characterized by the  $Y$  parameter which is a measure of the ratio of the scattering wavelength to the molecular mean free path.<sup>8,9</sup> This parameter is a measure of the relative contribution of the central Rayleigh scattering peak, and the two side bands corresponding to Brillouin scattering. A  $Y$  parameter much greater than one corresponds to strong Brillouin components, while a  $Y$  value much less than one corresponds to Rayleigh scattering only. The  $Y$  parameter

can be expressed as a function of flow parameters and scattering angle:

$$Y = 0.2308 \left[ \frac{T(\kappa) + 110.4}{T^2(\kappa)} \right] \left[ \frac{P(\text{atm})\lambda(\text{nm})}{\sin \theta/2} \right] \quad (3)$$

In addition to the useful Rayleigh signal, there will also be some stray elastic scattering which has total energy per pulse of K and the same spectral profile and frequency as the laser.

$$E_E(v) = K l(v - v_l) \quad (4)$$

When the Rayleigh energy,  $E_R$ , and the stray scattering energy,  $E_E$ , are passed through the absorption filter, detected by an intensified CCD camera, and converted into a grayscale value by a frame grabber, the final signal level, S (0-255), for one resolution element is given by:

$$S = C \left[ \int_{-\infty}^{\infty} E_R(v) t(v) dv + \int_{-\infty}^{\infty} E_E(v) t(v) dv \right] \quad (5)$$

where  $t(v)$  is the transmission of the filter at frequency  $v$ , and  $C$  is a constant which takes into account transmission of the focusing optics, quantum efficiency of the camera, gain of the microchannel plate, and analog to digital conversion of the video signal performed by the frame grabber. This equation assumes that the camera gain, and frame grabber A to D conversion are linear and that a value of zero for S corresponds to values of zero for  $E_R$  and  $E_E$ .

Equations 1 through 5 can be summarized to show explicitly the parameters which influence S:

$$S(\lambda, \theta, R, B, v, P, T, v_l) = R \frac{P}{T} \times \left[ \int_{-\infty}^{\infty} \left\{ \int_{-\infty}^{\infty} l(v - [v_l + v_D(v, \lambda, \theta)]) - v') g(Y(P, T, \theta), v') dv' \right\} t(v) dv \right] + B \int_{-\infty}^{\infty} l(v - v_l) t(v) dv \quad (6)$$

Here, R and B are the products of constants in equations 1, 4 and 5, and in most experiments may be considered calibration parameters.  $\lambda$  is the absolute wavelength of the laser and is necessary only for calculating the Doppler shift and the Y parameter; it is known precisely from the literature.  $v$ ,  $P$ , and  $T$  are the unknowns in the experiment. Since these are three independent unknowns, at least three measurements of S must be made while varying  $t(v)$  or at least one of the remaining two parameters :  $\theta$ , or  $v_l$ . Varying  $t(v)$  corresponds to

simultaneous measurements of scattering through different absorption profiles (i.e. different cells). Varying  $\theta$  corresponds to using either multiple laser angles, or multiple viewing angles and collecting through identical filters. Varying  $v_l$  corresponds to collecting signals at various different laser frequencies. Using multiple  $\theta$ 's, or multiple cells with different  $t(v)$ 's, yields instantaneous information about flow parameters. For the work reported in this paper, however, we chose to measure time averaged flow parameters by tuning the laser frequency while monitoring camera signal levels. The main advantage of a time averaged measurement is that high signal levels may be achieved by averaging signal levels from several laser pulses. This minimized the statistical uncertainties caused by shot noise to a negligible level, so that systematic uncertainties could be evaluated and minimized. Additionally, fitting the data to our theoretical model is improved by collecting information at 110 different frequencies.

The raw data obtained in such a frequency tuning experiment consists of plots of resolution element intensity, S, versus laser frequency,  $v_l$ . These plots, one for each image resolution element, are then fit to equation 6 with  $v$ ,  $T$ , and  $P$  taken as fitting parameters. In order for such a fit to yield accurate results, all fixed parameters in equation 6 --  $\lambda$ ,  $\theta$ ,  $R$ , and  $B$  -- must be known, or independently measured. The laser lineshape,  $l(v)$  and the filter cell absorption profile,  $t(v)$ , must also be known or independently measured. Any errors in these four parameters or two profiles will propagate into systematic errors in the final values obtained for  $v$ ,  $T$ , and  $P$ . Finally, the accuracy of the fit will also depend on the accuracy with which the individual measurements of S and  $v_l$  are made. Any systematic error in S or  $v_l$  will again result in uncertainties in  $v$ ,  $T$ , and  $P$ .

### 3. MODEL PARAMETERS

Each of these four parameters,  $\lambda$ ,  $\theta$ ,  $R$ , and  $B$ , two profiles,  $l(v)$  and  $t(v)$ , and two measurement quantities, S and  $v_l$ , along with uncertainties in each is discussed in the following four sections.

#### Filter

Stability and accurate characterization of the absorption filter are required for the transmission profile  $t(v)$  to be accurately known. The filter used in recent experiments consists of a glass cell 2 inches in diameter and 4 inches long, with 2 inch diameter sleeves extending 2 inches beyond each of the two windows (figure 1). A few iodine crystals were placed in the sealed and evacuated cell. The temperature of the cell is measured and controlled by a temperature controller (stable to within  $\pm 0.5$  °C), an RTD element cemented onto the cell wall, and heating tape, which covers the entire cell body and sleeves. The pressure of the cell is set by accurately controlling the temperature of a side arm 'cold tip' which

is kept at a lower temperature than the cell body. The side arm is enclosed in a water jacket, and water temperature is controlled by a water bath with a specified temperature accuracy of  $\pm 0.01$  °C.

In order to characterize the transmission profile of the filter, it is necessary to have a means of accurately measuring the frequency of the interrogation laser relative to some absolute, stable reference. There is also a need to make similar measurements of the laser frequency,  $v_l$ , while performing an actual Filtered Rayleigh Scattering experiment. To this end, we have made use of a heterodyne technique which measures frequency relative to the peak of a Doppler broadened iodine absorption line at  $18789$  cm $^{-1}$  which corresponds to the P142(37,0) transition in the B-X electronic manifold. The experimental setup used to characterize the absorption filter is shown in figure 2. The laser used as the absolute frequency reference is a Lightwave model 124-1064-50-F narrow linewidth (5 kHz), cw, 50 mW, Nd:YAG laser. A small portion of the infrared light from this laser is frequency doubled using a KTP crystal. The green, frequency doubled light is separated from the infrared light, and passed through a 0.5 inch diameter iodine reference cell of similar construction as the filter cell. The main body of this reference cell is held at a temperature of 80 °C and the sidearm at a temperature of 45.7 °C. The light passed through this reference cell is detected with an amplified photodiode. A standard first derivative nulling technique<sup>10</sup> is used to lock the frequency of the doubled beam of the reference laser to the P142(37,0) absorption peak of the reference cell. The residual infrared laser light from the reference laser is sent through a fiber optic onto a high speed detector (New Focus model # 1434). A second, narrow linewidth, 40 mW, cw, Nd:YAG laser is used to interrogate the original iodine filter cell. This laser beam is also passed through a KTP crystal to generate a frequency doubled beam, which is used to measure transmission through the filter. The residual infrared light from the interrogation laser is passed through the same fiber optic onto the high speed photodetector, where it interferes with the reference laser beam. The interference generates a signal at a frequency equal to the difference between the frequencies of the reference laser and the interrogation laser. A Hewlett Packard microwave frequency counter with accuracy better than 1 MHz measures this heterodyne signal. The frequency difference between the frequency doubled beams is then twice the measured frequency difference between the infrared beams. This system allows for frequency measurements of the frequency doubled beam over a range of 80 GHz.

A computer model of iodine absorption<sup>2</sup> indicates that with a reference cell main body temperature stability of 1 °C and side arm temperature stability of 1 °C, the peak of the P142(37,0) transition is stable to within 1 MHz. In order to determine the stability of the frequency of the reference laser, the sensitivity of the feedback electronics must also be considered. To demonstrate the

short term stability, the heterodyne beat frequency was monitored while the reference laser was manually detuned, and allowed to re-lock. Because the short term (seconds) stability of the measurement laser is 75 kHz, the change in the beat frequency over this short time period is due solely to the change of the reference laser frequency. As shown in figure 3, the reference laser re-locks to within  $\pm 1$  MHz of its original frequency. This measurement along with the stability of the reference iodine cell demonstrates the short term frequency stability of this reference signal to be within  $\pm 2$  MHz. However, in an environment without temperature stabilization, the long term (days) frequency has been observed to shift by as much as a few tens of MHz. This shift is apparent when the system resides in a lab where the temperature cycles through as much as 5 °C in 24 hours. This sensitivity to ambient temperature is probably caused by the particular scheme used to generate the frequency modulation needed for the locking technique. A new frequency modulation scheme with reported sub-MHz stability<sup>10</sup> is currently being assembled. Currently, this long term drift is accounted for by measuring cell transmission versus laser frequency immediately before running a Filtered Rayleigh Scattering experiment, and determining the frequency shift of the reference laser relative to its frequency at the time of the original filter characterization.

Using this frequency measurement technique, the setup in figure 2 was used to determine the transmission profile,  $t(v)$ , of the iodine cell. A scan with a resolution of 10 MHz extending over 42 GHz is shown in figure 4. The absorption region used by the current experiments is enlarged in figure 5. The maximum uncertainty on the transmission measurements made with this setup is estimated to be  $\pm 0.5\%$ . The maximum uncertainty on the frequency measurements, as discussed above, is estimated to be  $\pm 2$  MHz. This does not include the long term drift which is accounted for with a calibration experiment at the time of the Filtered Rayleigh Scattering experiment. Three transmission profiles, analogous to figure 4, were taken in a temperature stabilized environment for analysis of FRS data. During data analysis, each of the three spectra were used independently for fitting experimental data to equation 6. The resulting differences in  $v$ ,  $T$ , and  $P$ , due to the iodine reference scan that was used were negligible.

### Laser

The interrogation laser used in the current experiments is an injection seeded, frequency doubled, pulsed Nd:YAG laser. In order to use equation 6 to analyze experimental data, the absolute wavelength,  $\lambda$ , of the laser, the instantaneous center frequency of the laser,  $v_l$ , relative to the reference laser, and the laser lineshape,  $l(v)$ , must all be known, or independently determined.

The wavelength of the laser can be determined from the wavelength of the iodine absorption line used as the

filter. As measured by Gerstenkorn and Luc,<sup>11</sup> this line is located at  $18788.4509\text{ cm}^{-1}$  with an uncertainty of  $\pm 0.002\text{cm}^{-1}$ . During the Filtered Rayleigh Scattering experiment, the frequency of the laser is tuned over approximately 5 GHz, which corresponds to a change in wavelength of 0.005 nm. Conservatively, the laser wavelength,  $\lambda$ , which is used to calculate the Doppler shift, equation 2, and the Y parameter, equation 3, may be taken to be  $532\text{ nm} \pm 0.5\text{ nm}$ . This overestimate in the uncertainty of wavelength has negligible effects on the accuracy of measurements of velocity, temperature, and density.

In order to determine the central frequency of the pulsed laser, a small portion of the infrared, cw seed laser is split off from the main beam and combined with the cw infrared beam from the reference laser described above. The same heterodyne system that was used to characterize the filter, is then used to determine the frequency difference between the seed beam and the reference laser. If the central frequency of the pulsed laser is precisely determined by the seed beam, then it is accurately measured by the heterodyne signal. In order to determine how well the pulsed laser frequency matches that of the seed beam, one must know the particular mechanism by which the pulsed laser is locked to the seed laser. For most available lasers, including the laser used in the current experiments, locking is achieved through Q-Switch Buildup Time Reduction (BUTR). This feedback system varies the oscillator cavity length of the pulsed laser while monitoring the time between the firing of the Q-switch and laser emission. When the Q-Switch buildup time is minimized, the pulsed laser is well seeded, and its frequency is very close to that of the seed beam. This feedback system requires that the pulsed oscillator cavity length be continuously dithered, so that even when the pulsed laser is well seeded, its frequency may still oscillate over a small range due to frequency 'pulling' of the output pulse with respect to the seed frequency.<sup>12</sup> This frequency dither is specified by the manufacturer to be less than  $\pm 10\text{ MHz}$  at  $532\text{ nm}$ . For Filtered Rayleigh Scattering experiments, such as those reported below, that determine flow parameters by fitting data obtained from many laser pulses, the effect of this dither should be negligible, since, on average, half of the laser pulses will have a central frequency up to 10 MHz higher than the measured seed laser frequency, and half will have a central frequency up to 10 MHz lower. For instantaneous measurements, however, this frequency dither must be taken into account if one is to attain accurate velocity measurements.

In addition to this frequency dither, one must also consider the effects of frequency tuning on injection seeding. Scanning of the high power laser is accomplished by stepping the temperature of the seed laser crystal. This changes the crystal length and index of refraction, and therefore, the frequency of the seed laser. By monitoring the frequency of the seed laser after its temperature is changed, it has been determined that the

seed laser requires roughly 10 seconds to re-stabilize. Simultaneously, measurements of the feedback voltage to the piezoelectric crystal controlling the cavity length of the pulsed laser show that its frequency has also stabilized after 10 seconds (figure 6). In the experiments reported below, frequency tuning was accomplished by changing the seed laser temperature by discrete steps, and allowing 10 seconds after each step before collecting data. New laser systems currently under development make use of different seeding and tuning techniques, and so the next generation of tunable lasers should be capable of frequency tuning on a shot to shot basis. An alternative locking scheme is further developed in the discussion of future work.

Characterization of the laser frequency profile,  $I(v)$ , is also necessary for analysis. A small portion of the pulsed laser beam was passed through the filter cell, and transmission was monitored as a function of laser frequency. The resulting profile is a convolution of the filter profile  $t(v)$ , determined as described above, and the laser frequency profile,  $I(v)$ . Assuming first a purely Lorentzian laser frequency profile, and then a purely Gaussian profile, a number of data sets were each fit. These fits yielded laser linewidths, for the Lorentzian case, which were much narrower than the frequency transform limit of approximately 150 MHz (based on an infrared laser pulse length of 6 ns). The Gaussian fit, however, yielded more reasonable linewidths between 100 MHz and 200 MHz. An example of this test data and a fit using a Gaussian laser lineshape are shown in figure 7. Although this suggests that the use of a Gaussian lineshape is appropriate, it does not rule out the possibility that some small Lorentzian component is present. In any event, the linewidth of the Rayleigh - Brillouin scattering profile,  $g(v)$ , will generally be much broader than the laser linewidth, and so a small discrepancy in the laser lineshape will not introduce a significant error in the flow parameters determined when data is fit to equation 6.

In many laser based diagnostics experiments, it is desirable to continuously monitor the laser intensity, in order to filter out any change in signal due to drift or jitter in laser power. A simple photodiode and boxcar integrator monitoring the intensity of a small portion of the laser beam yielded intensity measurements with uncertainties larger than the small jitter and drift of the laser intensity itself. While a more precise intensity monitoring system may be used in the future, for the experiments reported here, the laser intensity was not continuously monitored, and any small jitter or drift was accounted for in the estimated uncertainties on the parameters R and B as described below.

### Camera

The discussion above, outlining the theoretical model, assumes the camera and frame grabber are linear in their response, i.e. that C in equation 5 is independent

of signal level. In order to test the linearity of the imaging system, a cw HeNe laser at 632.8 nm was used to illuminate an index card which was beyond the object plane of the camera. This yielded a temporally stable signal level across the entire CCD chip. With the camera and frame grabber parameters set to the values used in the Filtered Rayleigh Scattering experiments, the camera gate time was reduced in discrete steps, each equal to one tenth the initial value. For an ideal, linear system, this would result in a 10% decrease in signal level at each resolution element with each step. For a very non-linear system response, a calibration experiment such as this could be used to pre-process the signal levels from each resolution element in order to remove non-linearities before the fitting of the data to equation 6. Because the non-linearities appear to be small in this particular camera - frame grabber pair, the current work has not included such pre-processing. However, based on experimental results presented below, this assumption has come to be questioned, especially with regard to threshold values.

The model discussed above, also assumes that the collection solid angle subtended by the camera lens,  $d\Omega$ ,

is small enough to consider  $\frac{d\sigma}{d\Omega}$ ,  $v_D$ ,  $g(v)$ , and  $t(v)$ ,

constants over the entire solid collection angle. In order to determine the conditions for which this assumption is valid, a computer model which does not make this assumption (one which corrects for variation in angle and path length across the imaging lens) was developed, and its results compared to the model above. For this theoretical study, an idealized Mach 5 flow, with velocity equal to 721 m/s, static temperature equal to 50 K, and static pressure equal to 40 torr was assumed. The laser sheet was assumed to have a propagation direction 45° relative to the flow, and the camera was assumed to image at a nominal angle of 90° to the sheet. Filter transmission versus frequency plots were calculated for the point in the center of the field of view, using this more detailed model, assuming various collection f numbers (distance from lens to laser sheet / diameter of lens). These plots were compared to similar plots made using the simpler theory discussed above. As can be seen in figure 8, a very small collection f# results in very different curves for the two models. This is to be expected, since the scattering angle  $\theta$ , varies significantly across the solid collection angle  $d\Omega$ , resulting in large variations in Doppler shift  $v_D$ , and scattering profile  $g(v)$ . As the collection f# increases, the variation of  $\theta$  across the solid collection angle decreases, and so the discrepancy between the two models also decreases. For a collection f# greater than about 10, this discrepancy is small enough to be considered negligible.

For the experiments discussed below, the collection f# was approximately 15, so the variation in  $\theta$  across the solid collection angle was neglected. It was still necessary, however, to determine the value of  $\theta$  accurately in order to obtain  $v$ ,  $T$ , and  $P$  with low

uncertainties. The difficulty with the measurement of this angle is that there exists no convenient marker for the camera observation direction. In order to address this problem, a HeNe laser at 632.8 nm was positioned so that the beam was coincident with the central camera observation ray. The center of the camera lens, and the center of the field of view uniquely define this ray. By placing an index card in the HeNe beam at various locations, a spot was observed on the CCD chip. When the index card was in the object plane of the camera lens, the laser spot appeared as a small, focused spot; when the card was behind or in front of the object plane, the spot appeared as a much larger unfocused spot. The position and angle of the HeNe laser beam were varied until the in focus spot and out of focus spot were both centered on the central pixel of the CCD chip. At this point the HeNe laser precisely overlapped the main camera ray, and was, therefore, an accurate indicator of the observation direction. The scattering angle,  $\theta$ , was then measured by observing, on a protractor, the angle between the incident Nd:YAG laser beam and the HeNe beam. The accuracy of this technique was limited by the accuracy with which the protractor could be read, and was estimated to be  $\pm 1^\circ$ . In larger facilities this same technique could be used to obtain much more accurate angle measurements since a triangulation scheme could be used, where the lengths of three sides of a triangle composed of the Nd: YAG beam, the HeNe beam, and a line between them could be measured with small relative uncertainty.

### Other Parameters

In the discussion of the theoretical model presented above, it was shown that uncertainties in the fitted flow parameters  $v$ ,  $T$ , and  $P$  are dependent on the uncertainties in four fixed model parameters,  $\lambda$ ,  $\theta$ ,  $R$ , and  $B$ , two profiles,  $l(v)$  and  $t(v)$ , and two measurement quantities,  $S$  and  $v_I$ . The previous three sections have discussed all of these uncertainties with the exception of the two model parameters  $R$  and  $B$ . Both of these parameters depend critically on the particular experimental setup, and, therefore, cannot be predicted with even marginal accuracy from theoretical considerations. Although they could be taken as two additional fitting parameters, this would decrease the certainty with which  $v$ ,  $T$ , and  $P$  could be determined from the fit. Therefore, pre and post experiment calibrations were used to measure these two values to within some range. Two calibrations were performed, both with the filter cell removed from the front of the camera, thereby allowing for a  $t(v)$  profile of 1 (i. e. the absence of the filter cell is equivalent to the presence of a filter cell with 100% transmission at all frequencies). In the first calibration, the camera imaged an evacuated test section. With  $P$  equal to zero, and  $t(v)$  equal to 1, equation 6 becomes:  $S=B$ . For the second calibration, the camera imaged the test section at atmospheric conditions. In this case,  $P$  was assumed to be equal to 760 torr, and  $T$  was approximately 293 K ( $T$  was

measured with a thermocouple for each calibration run).

Equation 6 now becomes  $S = \frac{P}{T} R + B$ , and since B is known from the first calibration, R can be determined. Typical values and uncertainties for R and B are  $600 \pm 20$  and  $40 \pm 5$ , respectively.

#### **4. MEASUREMENTS**

##### **Experimental Set-Up and Data Collection**

In order to demonstrate the measurement capability of the Filtered Rayleigh Scattering technique, we have performed experiments under two test conditions. The first condition consists of ambient air at room temperature and pressure (nominally  $20^\circ\text{C}$  and 760 torr). Although the air is not moving, this test is still a good indicator of the accuracy of the velocity measuring capabilities of Filtered Rayleigh Scattering for the given temperature and pressure conditions, since the major uncertainties on the velocity measurement are expected to be absolute, not relative. The second test condition consists of a Mach 2 free jet pressure matched to ambient atmospheric pressure.

The experimental setup for these experiments is shown in figure 9. The frequency doubled, injection seeded, pulsed laser described above was used as the laser source. The beam was focused into a sheet and passed through the 6 inch by 6 inch vertical test section of a laboratory scale wind tunnel, at an angle of roughly 50 degrees to the vertical. The intensified CCD camera and zoom lens, captured scattered light at 90 degrees to the laser sheet. The iodine cell discussed above was placed between the camera lens and the flow to be used as the absorption filter. The first test condition of ambient room air was achieved by temporarily removing the windows on the test section before the experiment was performed, and by leaving opened a valve between the test section and the surrounding laboratory during the experiment. For the second test case, compressed atmospheric air was passed through a nozzle contoured to produce a Mach 2 flow which is pressure matched to atmospheric pressure. The stagnation pressure was held at 100 psig, and the stagnation temperature was measured to be 258 K. Isentropic calculations predict that the free stream velocity, static temperature, and static pressure at the exit of this jet should be 480 m/s, 143 K, and 753 torr. In order to achieve a significant Doppler shift, the Nd:YAG beam crossed the flow at an angle of  $50^\circ$ . This required that the measurement region in the flow be some 12 mm to 22 mm (or 2 to 4 nozzle diameters) downstream of the nozzle exit in order to keep the laser beam from hitting the nozzle. RELIEF experiments<sup>13</sup> performed along a line 19 mm from the nozzle exit yielded velocities varying from 477 m/s to 497 m/s. This variation indicates the flow in the FRS test region has already interacted with the shear layers, and so velocity, temperature, and

pressure values are not expected to be uniform, nor identical to the isentropically calculated values.

For each of the two test conditions, the experimental procedure consisted of first running calibrations, then taking experimental data, and concluding with calibration runs. Measurements of resolution element intensity, S, were taken when the test section was evacuated, and again when filled with air at atmospheric pressure and temperature. These data determined values for R and B, as discussed above. Additionally, during the calibration runs, a portion of the laser beam passed directly through the iodine absorption cell in order to determine a transmission versus frequency profile. This profile was then used to determine any long term frequency offset of the reference laser frequency, which may have occurred since the filter cell was characterized. The same profile was used to determine the laser linewidth as discussed above. Next, the filter was placed in front of the camera, and the flow was imaged at 110 different laser frequencies. Fifty frame averages were stored at each frequency. Finally, calibrations were again performed in order to detect any drifts in R, B, frequency offset, or laser linewidth during the run. The average of two values determined for each of R, B, frequency offset, and laser linewidth were subsequently used when analyzing the data.

Data analysis consisted of binning the camera pixels into 10 pixel by 10 pixel resolution elements, which correspond to roughly 300 micron by 300 micron points in the flow. The size of these resolution elements was determined by previous work which indicated that the resolution of the microchannel plate was effectively 5 pixels by 5 pixels on the CCD chip.<sup>14</sup> At each resolution element, an intensity versus frequency curve was generated, and then fit to equation 6 using parameter values,  $\lambda$ ,  $\theta$ , R, and B, and lineshape profiles,  $t(v)$  and  $l(v)$ , all of which were determined either during the calibration scans, or measured before the experiment as described in the sections above. Such data, S versus  $v_i$ , and the associated final fit to the model for a particular resolution element of the ambient air test conditions is shown in figure 10. These fits, one at each resolution element, yielded values for v, T, and P at each point in the flow.

##### **Uncertainty Analysis**

In order to estimate the uncertainties associated with the final measurements of velocity, the uncertainties in the parameters  $\lambda$ ,  $\theta$ , R, and B, and the uncertainties in the lineshape profiles  $t(v)$  and  $l(v)$  were all taken into account for one test point in the field of view for each of the two test measurement configurations. It is possible to independently calculate uncertainty measurements for velocity, temperature, and pressure at every point in the field of view. However, here, we present only a sample analysis of velocity uncertainty estimates at a point in the center of the field of view for the two conditions, ambient

air and a Mach 2 jet. Each of the individual uncertainties in the four parameters  $\lambda$ ,  $\theta$ ,  $R$ , and  $B$  propagates into uncertainties in velocity, in the following manner, analogous to:<sup>15</sup>

$$\Delta v = \frac{\partial v}{\partial \theta} \Delta \theta \quad (7)$$

Here, the uncertainty in velocity,  $\Delta v$ , due to an uncertainty in angle,  $\Delta \theta$ , is given. The uncertainty in  $\lambda$  is determined as discussed above. The uncertainty in  $\theta$  was estimated when it was measured. The uncertainties in  $R$  and  $B$  are estimated based on the variations between the pre and post calibration measurements at the various points in the test region.

In order to take into account the uncertainty of velocity due to uncertainty in the lineshape  $l(v)$ , the following equation is used:

$$\Delta v = \frac{\partial v}{\partial (\delta v)} \Delta (\delta v) \quad (8)$$

where  $\delta v$  is equal to the linewidth of the laser profile  $l(v)$  of the assumed Gaussian lineshape, which is obtained from the fits to the pre and post calibration experiments. Finally, systematic uncertainties in  $v_r$  arising due to uncertainty in the amount of the long term drift of the reference frequency were accounted for with equations of the form:

$$\Delta v = \frac{\partial v}{\partial v_r} \Delta v_r \quad (9)$$

where here,  $v_r$ , is the reference frequency. The uncertainty in linewidth,  $\delta v$ , and the long term drift of the reference frequency  $v_r$ , are estimated based on pre and post calibration values for a number of experiments. All of the partial derivatives in equations 6 through 8, except  $\frac{\partial v}{\partial \theta}$ , are calculated numerically by fitting the data with

the appropriate parameter changed slightly.  $\frac{\partial v}{\partial \theta}$  is calculated analytically, by using equation 2. In order to combine all of the individual contributions to the uncertainty in velocity, we assumed the individual uncertainties were uncorrelated, and took the square root of the sum of the squares<sup>15</sup> as the total systematic uncertainty. Table 1 summarizes the uncertainties in each of the parameters and profiles, shows the relevant partial derivatives at the test point for the first set of test conditions, and the uncertainty in velocity attributed to the uncertainty in each of the parameters and profiles. The final estimated uncertainty in velocity is 4 m/s. Table 2 shows the same data for the second test case (Mach 2 free jet). The final estimated uncertainty for this case is 5 m/s.

par	$\lambda$ (nm)	$\theta$ (deg)	R	B	$\delta v$ (MHz)	$v_r$ (MHz)	Total Uncer- tainty
typ. value	532.	91	600	40	150	--	
$\Delta p_{\text{par}}$	0.5	1	20	5	50	5	
$\frac{\partial v}{\partial (\text{par})}$	0.013	0.011	0.008	0.25	0.002	0.65	
$\Delta v$ (m/s)	0.007	0.011	0.16	1.25	0.1	3.25	3.5

Table 1: Uncertainties for velocity measurement in ambient air

par	$\lambda$ (nm)	$\theta$ (deg)	R	B	$\delta v$ (MHz)	$v_r$ (MHz)	Total Uncer- tainty
typ. value	532.	91	600	40	150	--	
$\Delta p_{\text{par}}$	0.5	1	20	5	50	5	
$\frac{\partial v}{\partial (\text{par})}$	0.38	0.41	0.004	0.91	0.002	0.44	
$\Delta v$ (m/s)	0.19	0.41	0.08	4.55	0.1	2.2	5.1

Table 2: Uncertainties for velocity measurement in Mach 2 jet.

These tables demonstrate, in both cases, that velocity is most sensitive to variations in  $B$ , the background scattering level, and  $v_r$ , stability of the frequency reference. Now that these parameter uncertainties have been reduced to acceptable levels, experiments can focus on identifying error sources that had been previously masked.

### Experimental Results

Results from the first test case are shown in color figure 1. This plot shows velocity, in the direction of sensitivity, as a function of downstream and spanwise location. The background here has been artificially set to a very low velocity delineated by dark red. The actual data is shown throughout the laser sheet which extends from the top right of the plot to the bottom left. Measured velocity values within the sheet range from -12 m/s to 31 m/s. The errors in these velocity measurements are considerably larger than the predicted uncertainty in Table 1. Because the uncertainties associated with the parameters listed in Table 1 are small, the larger errors must be due to other factors. A comparison of color figure 1 with color figure 2, which shows the calibration parameter  $R$ , indicates that the variations in measured velocity are correlated with variations in the magnitude

of  $R$ . However, the variation in  $R$  is caused primarily by the spatial profile of the laser. This correlation suggests the measured velocity depends on the recorded laser intensity. This is probably an artifact of the non-linearity of the detection system, which was neglected in the original analysis. The observed correlation between measured velocity value and laser intensity suggests that even a small amount of non-linearity in the detection system causes uncertainties in the velocity measurement. Once this non-linearity is accounted for, a variation in measured values closer to the predicted value of  $\pm 4$  m/s can be expected. In particular, the region at the top of the laser sheet, with low laser energy (less than 75% of the peak), accounts for most of the distribution in measured velocity. Neglecting this small portion of the laser sheet yields a measured velocity range between -12 m/s and 10 m/s.

Velocity values obtained with the Mach 2 free jet are shown in color figures 3 and 4. In these figures, the values in the region outside of the laser beam have been artificially set to 0 m/s (yellow). The core of the jet can clearly be seen as the violet region, while the shear layers are apparent on either side of the core, extending from the violet region near 200 m/s to the yellow zero values. It should be emphasized that the measured velocity is the velocity component along the direction of sensitivity, which is determined by the laser propagation direction, and the camera observation direction. Points outside of the flow, but still within the laser sheet were analyzed and assigned their measured velocity values, all of which were close to 0 m/s, as evidenced by the fact that the laser sheet cannot be differentiated from the background, outside the jet. The velocity measurements within the core of the jet vary from 192 m/s to 221 m/s. Again, some of this distribution in velocity is generated by the variation in laser intensity across the laser sheet. However, much of it is probably due to a real variation in velocity at this point in the flow. Evidence of such variations have been observed previously during RELIEF experiments performed with a tag line at 19mm from the nozzle exit. These RELIEF experiments yielded values for free stream velocity. After correcting for a slight difference between stagnation temperature, the RELIEF experiments predict free stream velocities ranging from 477 m/s to 497 m/s.

In order to project from the velocity in the direction of sensitivity of the Filtered Rayleigh Scattering experiment, to the velocity in the free stream direction, the angle between the direction of sensitivity and the free stream must be measured. For an angle of  $65.5^\circ$ , the Filtered Rayleigh Scattering velocities would be in precise agreement with the RELIEF velocities. During the FRS experiment, this angle was measured by assuming that the free stream direction was perpendicular to the flat top of the nozzle exit. All angles were measured, therefore, with the flat nozzle top being taken as a reference. Using this technique, the angle between the direction of FRS sensitivity and the free stream was

determined to be  $62.7^\circ \pm 0.7^\circ$ . The  $2.0^\circ$  to  $3.4^\circ$  discrepancy between this angle and the required  $65.5^\circ$ , is probably due to a slight deviation between the free stream direction and the direction perpendicular to the flat top of the nozzle exit. It should be emphasized that the difficulty in measuring the angle between the direction of velocity sensitivity and the free stream velocity is not unique to Filtered Rayleigh Scattering. This issue will be important in any technique that measures Doppler shift to determine one component of velocity.

Although the temperature and pressure data obtained from the Filtered Rayleigh Scattering experiments has not yet been fully analyzed, we present here preliminary plots of this data for the Mach 2 conditions. Color figures 5 and 6 show 3-D plots of temperature and pressure. Both show behavior of the parameters as expected. The pressure of the free jet appears to be the same as that of the ambient surroundings, as expected, although the pressure values vary significantly across the entire region of interest. The temperature of the free jet is seen in color figure 6 to be significantly lower than that of the ambient, also as expected. Although the variation of measured temperature across the jet is  $\pm 17$  K, the average value of 142 K matches the isentropically calculated value well.

## 5. FUTURE WORK

This work has emphasized control of experimental uncertainties to minimize the systematic uncertainties associated with Filtered Rayleigh Scattering. However, statistical uncertainties must also be considered. Signal to noise limitations arise primarily due to shot noise. In order to reduce this statistical uncertainty to below 1%, it is necessary to collect 10,000 photo-electrons per resolution element. Earlier discussions<sup>16</sup> for realistic conditions, using the Nd:YAG/iodine FRS paradigm, and f5 optics, conclude that a CCD camera generates 64 photo-electrons per resolution element per laser pulse. This yields measured intensity variation of 1 part in 8, or 12.5%. Time averaging, however, allows for the collection of a larger number of photons. By averaging 160 laser pulses, or 16 seconds at 10 Hz repetition rate, at each measurement point, the shot noise is reduced below 1%. However, this scheme prevents instantaneous measurements. Because the Rayleigh scattering cross-section increases dramatically in the ultraviolet, due to the frequency,  $\nu^4$ , and index of refraction,  $(n-1)^2$ , scaling, it is possible to collect in excess of 600 photo-electrons per laser pulse at 253.7 nm for the same experimental setup. The single pulse shot noise is reduced to an uncertainty of 2.4%.

Applying the Titanium:Sapphire/Hg Filter paradigm to FRS, yields noticeable improvements both because of the laser and filter characteristics. Current efforts to complete a high power, narrow linewidth, tunable ultraviolet laser system are underway. By injection seeding a pulsed Ti: Sapphire, and frequency tripling the tunable infrared output, we achieve in excess of 10 mJ of

tunable, narrow linewidth, ultraviolet light. To insure single mode operation while the laser is frequency tuned, efforts to complete injection locking of the pulsed Ti: Sapphire are underway. To avoid the necessarily slow tuning rate of the BUTR injection locking technique of the Nd:YAG, a novel method of injection locking via a fringe locking technique is being developed in collaboration with Schwartz Electro-Optics, Inc.<sup>17</sup> The implication of such a locking technique is that the feedback is given on an instantaneous basis, rather than on the shot to shot basis of the BUTR. Feedback to the locking system is given between laser pulses, and thus, tracking by this system offers a frequency agile laser. Tuning may be faster, take discontinuous jumps, or dither over a wide range, without fear of unlocking.

The development of a novel atomic vapor filter for FRS, using mercury, allows for a variety of improvements, as well. Because of the strong absorption and high atomic weight of mercury, achieving very high optical depth is attainable. Model fits to experimental transmission scans of a 5 cm length mercury vapor filter, suggest optical depths in excess of 1000.<sup>17</sup> A detailed scan of the Hg 202 line for a sidearm temperature of 23 C (figure 11), demonstrates the nearly ideal characteristics of a mercury vapor filter. The high optical depth translates into an ability to suppress very strong elastic scattering, while transmitting weaker Doppler shifted signals, as would be desirable for imaging air flow over a model (or imaging a boundary layer). Mercury does not suffer the background absorption difficulties of iodine. As a result, it is possible to dramatically vary the width of the absorption profile of the filter. This leads to the tailoring of filters to an appropriate experiment and to the use of multiple filters for instantaneous measurement of T, P, v. As previously mentioned, iodine experiments to date relied on scanning laser frequency; however, multiple Hg filters may be used with varying transmission profiles, to extract the same information on an instantaneous basis. Alternately, it may be possible to affect the mercury cell linewidth with an applied magnetic field. Then, a single cell could be rapidly 'scanned' to achieve multiple measurements for instant calibration, and achieve several data points for varying absorption profiles,  $t(v)$ .

## 6. SUMMARY

The major components of a Filtered Rayleigh Scattering experiment have been examined and sources of systematic uncertainty have been identified and controlled to acceptable levels. With these sources of uncertainty reduced, current experimental results may now be used to determine other sources of uncertainty which had previously been masked. Work continues on the development of an UltraViolet Filtered Rayleigh Scattering system which will allow for reduction of statistical uncertainty.

## ACKNOWLEDGMENTS

We would like to thank Professor Tenti, University of Waterloo, for making available to us his program for calculating Rayleigh Brillouin profiles.

This work was conducted under the support of the Air Force Office of Scientific Research, NASA-Langley, NASA-Lewis, and Small Business Innovative Research Programs under M.L. Energia, Inc. and Schwartz Electro-Optics, Inc.

## REFERENCES

1. R.B. Miles and W.R. Lempert, "Two Dimensional Measurement of Density, Velocity, and Temperature, in Turbulent High Speed Air Flows by UV Rayleigh Scattering," Applied Physics B, Vol. 51, pg. 1, 1990.
2. R.B. Miles, J.N. Forkey, and W.R. Lempert, "Filtered Rayleigh Scattering Measurements in Supersonic/Hypersonic Facilities," 7th Aerospace Ground Testing Conference, Nashville, TN, July 1992. AIAA-92-3894
3. J.N. Forkey, W.R. Lempert, S.M. Bogdonoff, G.Russell, and R.B. Miles, "Volumetric Imaging of Supersonic Boundary Layers Using Filtered Rayleigh Scattering Background Suppression," 32nd AeroSciences Meeting and Exhibit. Reno, NV, Jan. 1994. AIAA 94-0491.
4. G.S. Elliot, M. Samimy, and S.A. Arnett, "A Study of Compressible Mixing Layers Using Filtered Rayleigh Scattering," 30th AeroSciences Meeting and Exhibit. Reno, NV, Jan. 1992. AIAA 92-0175.
5. G.S. Elliot, M. Samimy, and S.A. Arnett, "Details of A Molecular Filter Based Velocimetry Technique," 32nd AeroSciences Meeting and Exhibit. Reno, NV, Jan 1994. AIAA 94-0490.
6. J.F. Meyers, "Development of Doppler Global Velocimetry," 18th Aerospace Ground Testing Conference, Colorado Springs, CO, June 1994. AIAA 94-2582.
7. M. Winter and J.A. Shirley, "Air Mass Flux Measurement System Using Doppler Shifted Filtered Rayleigh Scattering," 31st AeroSciences Meeting and Exhibit. Reno, NV, Jan. 1993. AIAA 93-0513.
8. G. Tenti, C.D. Boley, and R.C. Desai, "On the Kinetic Model Description of Rayleigh-Brillouin Scattering From Molecular Gasses," Canadian Journal of Physics, Vol. 52, pg. 285, Feb. 1974.

## FIGURES

9. H. Shimizu, S.A. Lee, and C.Y. She, "High Spectral Resolution Lidar System with Atomic Blocking Filters for Measuring Atmospheric Parameters," Applied Optics, Vol. 22, pg. 1373, 1983.

10. A. Arie, M.L. Bortz, M.M. Fejer, and R.L. Beyer, "Iodine Spectroscopy and Absolute Frequency Stabilization with the Second Harmonic of the 1319-nm Nd:YAG laser," Optics Letters, Vol. 18, pg. 1757, 1993.

11. S. Gerstenkorn, and P. Luc, Atlas du Spectre d'Absorption de la Molecule Diode, Part 3, pg. 53, 1978.

12. Y.K. Park, G. Giuliani, and R.L. Beyer, "Unstable Single-Axial-Mode Operation of an Unstable Resonator Nd:YAG Oscillator by Injection Locking," Optics Letters, Vol. 5, pg. 96, 1980.

13. R.B. Miles, J. Connors, E. Markovitz, P. Howard, and G. Roth, "Instantaneous Supersonic Velocity Profiles in an Under Expanded Sonic Air Jet by Oxygen Flow Tagging," Physics of Fluids A, Vol. 1, pg. 389, 1989.

14. personal communication: Kyritsis, D., Engine Lab., Mechanical and Aerospace Engineering Department, Princeton University, Princeton, NJ.

15. see, for example, P.R. Bevington Data Reduction and Error Analysis for the Physical Science, Mc Graw Hill, 1969.

15. R.B. Miles, J.N. Forkey, N.D. Finkelstein, and W.R. Lempert, "Precision Whole-Field Velocity Measurements with Frequency Scanned Filtered Rayleigh Scattering," 7th International Symposium on Application of Laser Techniques to Fluid Mechanics, Lisbon, Portugal, July 1994.

16. N.D. Finkelstein, J.Gambogi, W.R. Lempert, R.B. Miles, G.A. Rines, A. Finch, and R.A. Schwarz, "Development of a Tunable Single Frequency UltraViolet Laser Source for UV Filtered Rayleigh Scattering" 32nd AeroSciences Meeting and Exhibit. Reno, NV, Jan. 1994. AIAA 94-0492.

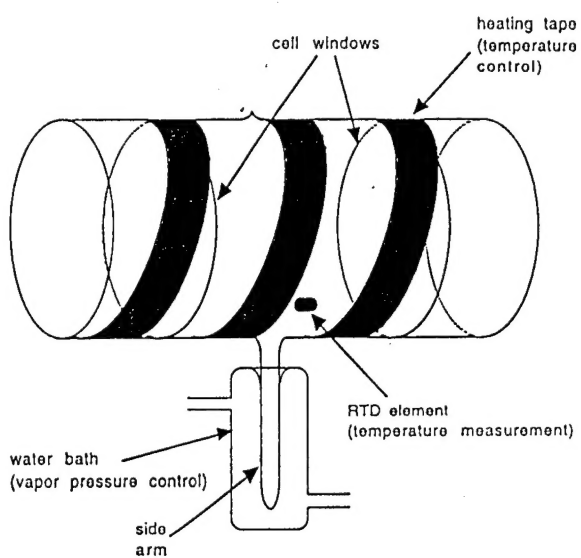


Fig. 1: Iodine absorption cell.

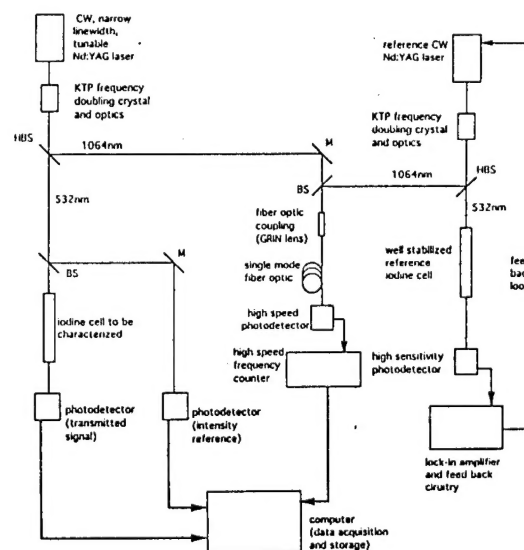


Fig. 2: Experimental setup used to characterize iodine cell. Frequency reference is on the right, and the transmission measurement setup is on the left. Abbreviations are: BS - beam splitter, HBS - harmonic beam splitter, M - mirror.

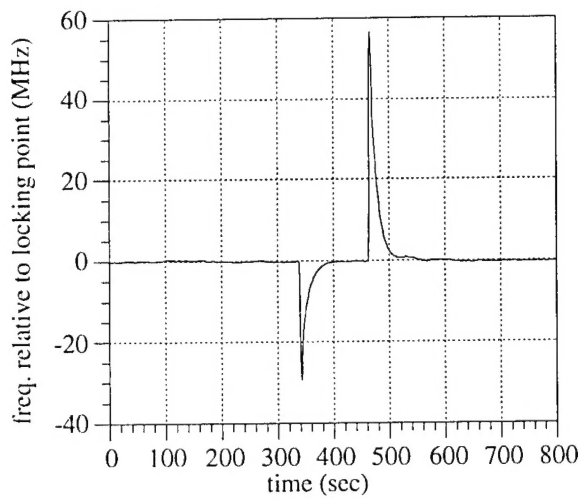


Fig. 3a: Demonstration of re-locking of reference laser after manual de-tuning.

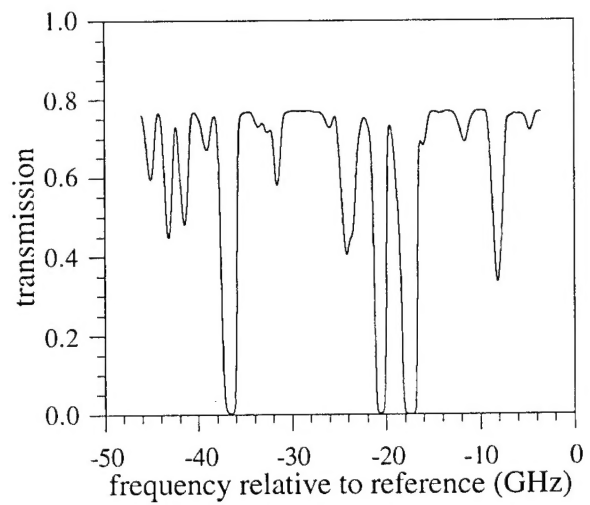


Fig. 4: Transmission profile of iodine filter cell

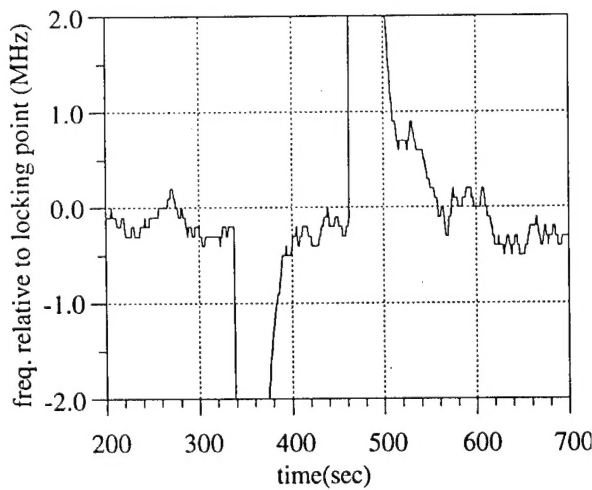


Fig. 3b: Enlargement of figure 3a, showing the reference laser re-locking to within  $\pm 1$  MHz.

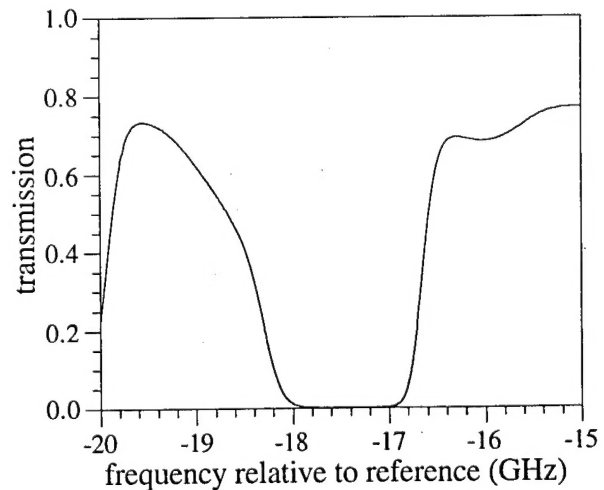


Fig. 5: Detail of filter transmission profile

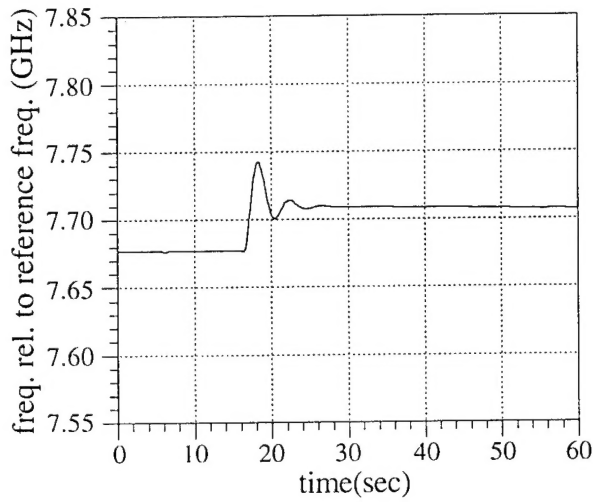


Fig. 6a: Frequency of injection seeder after a discrete change in tuning voltage

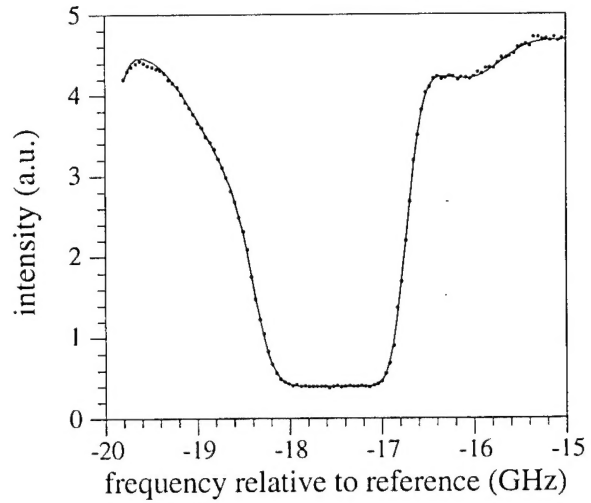


Fig. 7: Fit of calibration data (points) to a convolution between the Gaussian laser line profile and the filter transmission profile (line)

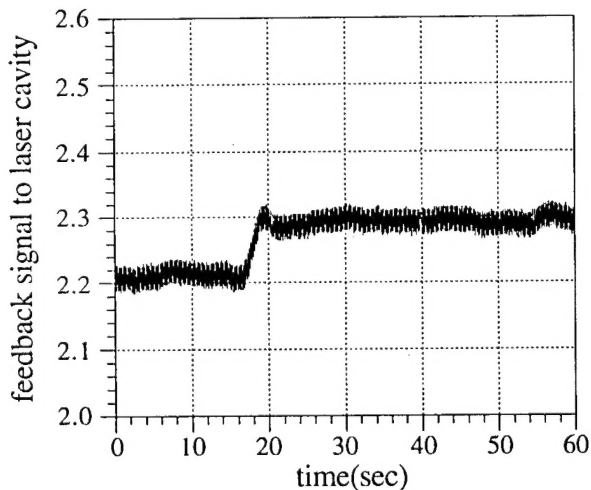


Fig. 6b: Feedback signal which controls locking of laser by changing oscillator cavity length

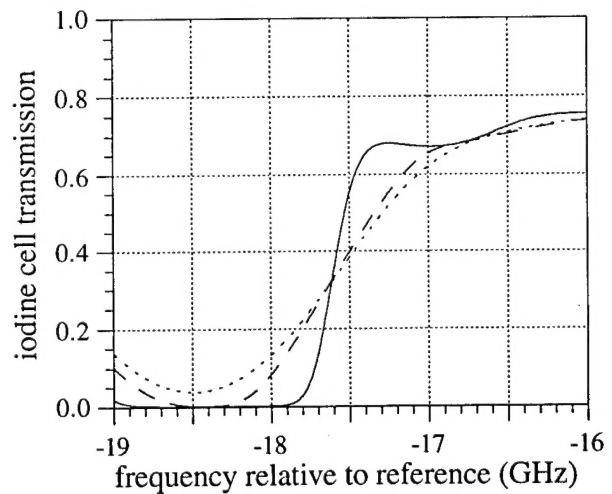


Fig. 8a: Response of the iodine filter to scattering from an idealized Mach 5 flow, imaged with a collection f# of 1. The solid curve shows the response predicted for narrow linewidth scattering when effects of the solid collection angle are neglected. The dashed line includes the effects of the solid collection angle, again assuming narrow linewidth scattering. The dotted line includes the effects of the solid collection angle, as well as the Rayleigh-Brillouin scattering profile.

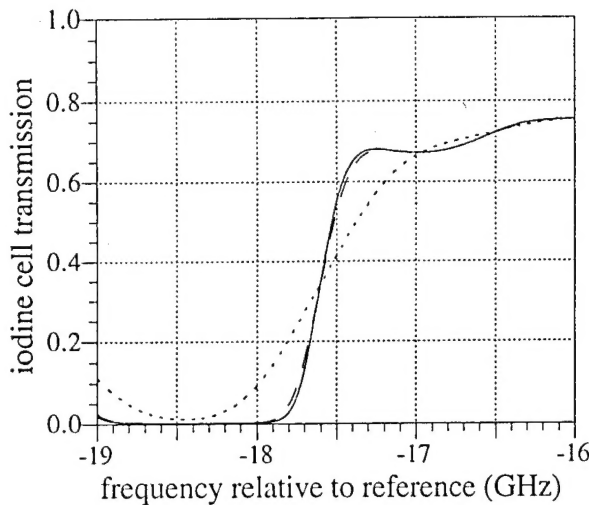


Fig. 8b: Response of the iodine filter to scattering from an idealized Mach 5 flow, imaged with collection f# of 5

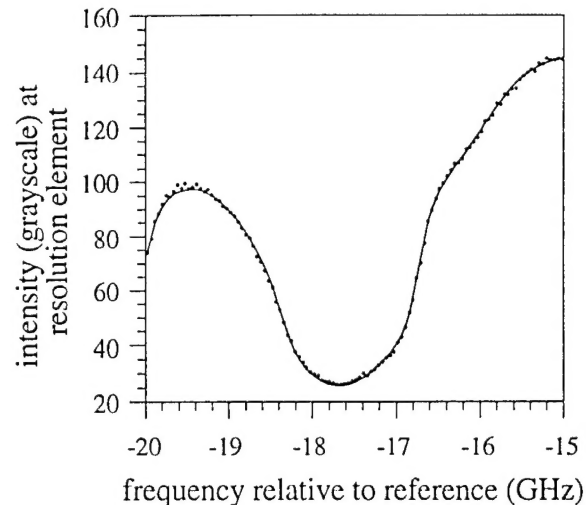


Fig. 10: Fit of grayscale data values at one resolution element (points) to  $S(v)$  as given by equation 6 (line).

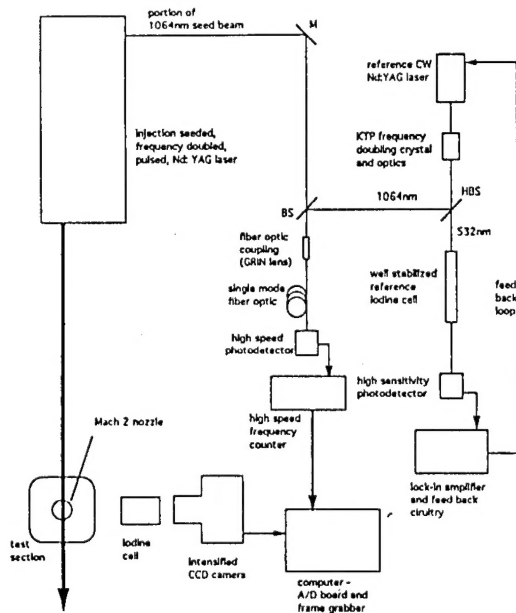


Fig. 9: Experimental setup for Filtered Rayleigh Scattering experiments. Abbreviations are as in fig. 2.

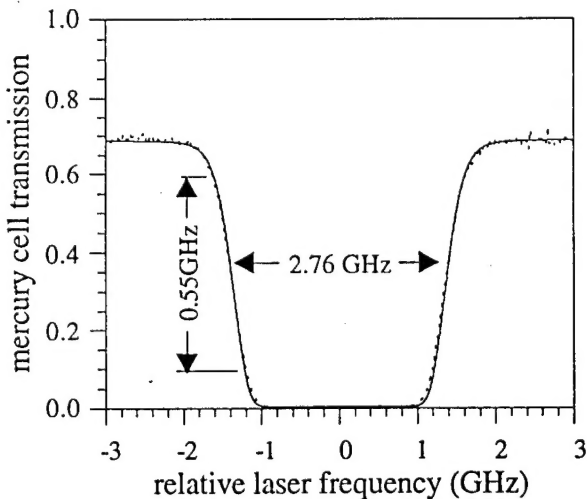


Fig. 11: Experimental scan of mercury vapor cell transmission (dotted) at 253.7 nm for a 5 cm long cell with a cell temperature of 48°C, and a side arm temperature of 23°C. Fit to theory (solid) yields an optical depth of 71.